2017

Integrating Nano-Patterned Ferromagnetic and Ferroelectric Materials For Smart Tunable Microwave Applications

Tengxing Wang
University of South Carolina

INTEGRATING NANO-PATTERNED FERROMAGNETIC AND FERROELECTRIC MATERIALS FOR SMART TUNABLE MICROWAVE APPLICATIONS

by

Tengxing Wang

Bachelor of Science
Tianjin University of China 2010
Master of Science
Fudan University of China 2012

Submitted in Partial Fulfillment of the Requirements

for the Degree of Doctor of Philosophy in

Electrical Engineering

College of Engineering and Computing

University of South Carolina

2017

Accepted by:

Guoan Wang, Major Professor

Mohammod Ali, Committee Member

Grigory Simin, Committee Member

Chen Li, Committee Member

Cheryl L. Addy, Vice Provost and Dean of the Graduate School

Dedication

This dissertation is dedicated to my wife and parents for their love and support.

Acknowledgments

The four-year Ph.D. experience in the University of South Carolina is a hard but valuable journey. It is absolutely a milestone in my life, and an important starting point for my future career. During my Ph.D., I received all kinds of help from people around me, and I couldn't have finished this dissertation without the support from them. It is my great pleasure to acknowledge them for their guidance, assistance and company.

Foremost, I would like to express my most sincere gratitude to my adviser Dr. Guoan Wang. I'm still feeling grateful that four years ago Dr. Wang gave me the opportunity to participate in his research group and become a member of SMART Lab. It is really my great fortune to meet Dr. Wang and research under the guidance of Dr. Wang. His inspiring ideas, broad scientific knowledge, and deep technology insight impress me all the time, and lead me in all the way of my research work. Dr. Wang gives me sufficient freedom in my research to work with the topics I'm interested in, and when I have any issues, he is always there to help, and he is always able to propose smart and efficient methods to tackle the issues. Absolutely Dr. Wang is one of the smartest and nicest people I've ever met. In my opinion, in addition to scientific research, what I have learned most from Dr. Wang is the attitude towards the science and life. Dr. Wang is full of positive and optimistic attitude, and that power always influences me and encourages me against frustrations and failures. What I have learned and gained from Dr. Wang is invaluable, and I could not have imagined having a better adviser.

I would like to thank Prof. Mohammod Ali, Prof. Grigory Simin and Prof.

Chen Li for their valuable time and effort serving in my Ph.D. committee and for their brilliant, constructive and precious suggestions in the proposal defense and dissertation. I'm very grateful to the scientists in Center for Nanoscale Materials, Argonne National Laboratory: Dr. Ralu Divan, Dr. Leonidas Ocola and Mr. Daniel Rosenmann, for supporting me with the research and fabrication in the clean room. Without their involvement and efforts, I could not have finished my fabrication and research.

I am indebted to my colleagues and friends in the SMART Lab: Yujia Peng, Wei Jiang, B M Farid Rahman and Yong Mao Huang, for stimulating research discussions, for the great help in simulation, fabrication and measurement, and for all the progress we have made together under the guidance of Dr. Guoan Wang. I also want to thank my office mates: Wuzhao Yan, Zhichao Liu, Zheqing Zhou, Lixing Yang, Guangxing Niu and Shijie Tang, for their friendship and company. Because of them, my Ph.D. life is rich, colorful, and memorable.

Most importantly, I would like to express my eternal love and appreciation to my beloved wife, Chunling (Penny) Wang. If there are three things in the world that I love most, they are sun, moon and you. Sun for days, moon for nights, and you forever. I always think the most fortunate thing in my life is meeting you and marrying you. I always appreciate your selfless sacrifice and great efforts for our family. I always feel happy because of your everlasting love, company, and unlimited support. It is you and your endless love that grant me the power to go through every hard period, and make me believe there is always hope, just because I will always fight for you and will never ever let you down. Thank you and I will always love you.

I would like to express my gratitude and love to my parents: Lijun Wang and Guanghui Li. Thank you very much for your endless love, unlimited support and understanding. I'm proud of being your son, and proud of having you as my parents.

Abstract

The wireless communication market has been ever-growing in the recent decades. Radios with high performance and capabilities to support wireless connections are increasingly demanded. Recent developments in wireless communications targeting ubiquitous connections have resulted in ever more complex system structures for supporting multiple frequency bands and standards. Reconfigurable and tunable RF/microwave technologies have the potential to significantly simplify the systems. The main objective of this dissertation is to develop tunable technologies and design concepts, and propose a new design methodology to implement dually electrically tunable microwave components by integrating both selectively patterned ferromagnetic and ferroelectric materials.

The first part of the dissertation demonstrates the concept and topology of selectively patterned ferromagnetic (Permalloy) thin film enabled electrical tunability. The properties of Permalloy are demonstrated in details, and electrically tuning mechanism and topology are introduced and analyzed with both magnetic simulation and measurement results. By integrating selectively patterned Permalloy thin film to the coplanar waveguide transmission line, electrically tunable microwave transmission line is achieved. The inductance density of tunable transmission line can be electrically tuned by dc current, and the feasibility of Permalloy enabled electrical tunability is proved. To further validate the efficacy and utilize the topology to design tunable microwave components, tunable inductors and a tunable bandpass filter are designed and fabricated. For the tunable inductors, a planar spiral inductor and a 3-D solenoid inductor are implemented. Permalloy thin film is integrated with inductors

to enable the tunability, and more than 10% inductance tunability has been achieved. Design principle of the tunable bandpass filter is then analyzed and demonstrated, and by integrating Permalloy thin film, the center frequency can be continuously tuned by dc current.

Based on the topology of Permalloy enabled electrical tunability, the second part of the dissertation proposes and demonstrates the methodology of ferromagnetic (Permalloy) and ferroelectric (PZT) enabled dual tunability for electrically tunable microwave applications. The tunable microwave components have both inductive and capacitive tunability by simultaneously integrating Permalloy and PZT thin films. To validate the efficacy and prove the concept, two dually electrically tunable phase shifters are implemented, including a slow wave transmission line phase shifter and a 3-D lumped-element phase shifter, and the performance can be tuned by applying dc current and/or dc voltage. Compared with planar transmission line phase shifter, 3-D structure has significant higher tuning efficiency and more compact size, and thus the maximal length normalized phase tunability has reached to 210°/cm. The dual tunability enabled by Permalloy and PZT not only improves the design flexibility and electrical tuning range, but also, more importantly, realizes the capability of characteristic impedance retaining, by which when microwave components are tuned, the characteristic impedance can be kept constant. This design concept and methodology can be further developed and applied to implement other tunable microwave components and circuits to realize tunable communication systems.

Table of Contents

List of Tables

List of Figures

Chapter 1

Introduction

1.1 Motivation

The fast growing wireless communication market has seen dramatic changes in both requirements and capabilities of the radios to support wireless connections. Recent developments in wireless communications have resulted in the radios that have evolved from a single-mode, triple-band 2G system to a triple-mode, 9-band (4×GSM, 5×UMTS with HSPA+) high-speed data-capable system in year 2010. The trend of mobile devices targeting ubiquitous connection continues, and a fast growing number of frequency bands are required to be supported. As the fourth generation (4G) long-term evolution (LTE) systems are rapidly deployed, the number of frequency bands listed in the current LTE specifications has reached to 40, with the operation frequency ranging from 0.7 GHz to 3.8 GHz [1, 2].

Modern wireless communication systems are required to support multiple frequency bands. Furthermore, integrating multi-functional modules into a single wireless device to operate over different standards has become a defined trend. Such demands in the market put critical requirements on the performances of the wireless systems, including higher functionality, more compact size, longer battery life, and more importantly, lower cost. Figure 1.1 illustrates such a scenario that a modern cellphone is compatible with several wireless standards, including 3G, 4G, GPS, Bluetooth, WiFi, etc.

The higher level integration of functionality without imposing a substantial

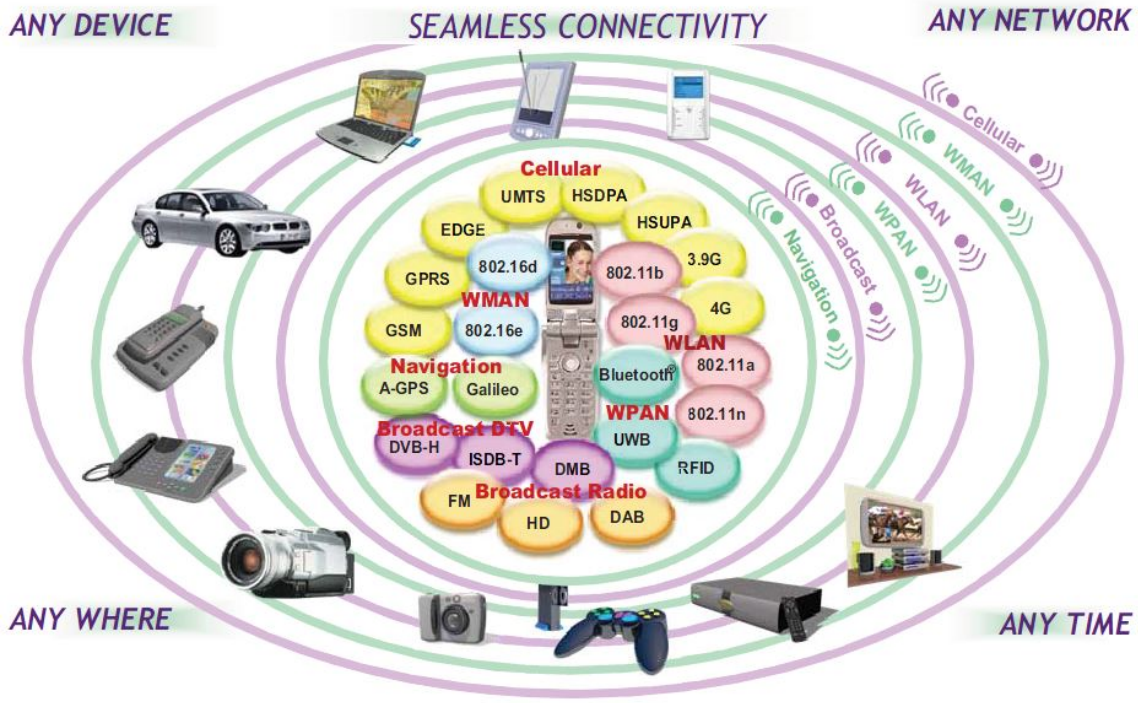

Figure 1.1: Modern mobile handsets can support multiple frequency bands and wireless standards [3].

increase in cost offers obvious benefits to the end users, while it raises significant challenges to the system designers and manufactures, especially for today's even more complex wireless communication systems. Figure 1.2 depicts the system architecture of a highly integrated RF transceiver subsystem, which is compatible with HSDPA/WCDMA/EDGE standards [4]. Parallel integration is utilized and separate RF front-ends are stacked to support different frequency bands and wireless standards. Large die area is required for the architecture, and even larger area is needed for the off-chip passive components, such as filters, duplexers, and switches.

To realize true wireless ubiquity and meet the challenge of high integration, technological innovations from both system level and device level are highly demanded. On the system level, concepts such as software defined radio (SDR) and cognitive radio (CR) [5] are proposed and widely utilized. Reconfigurable RF systems

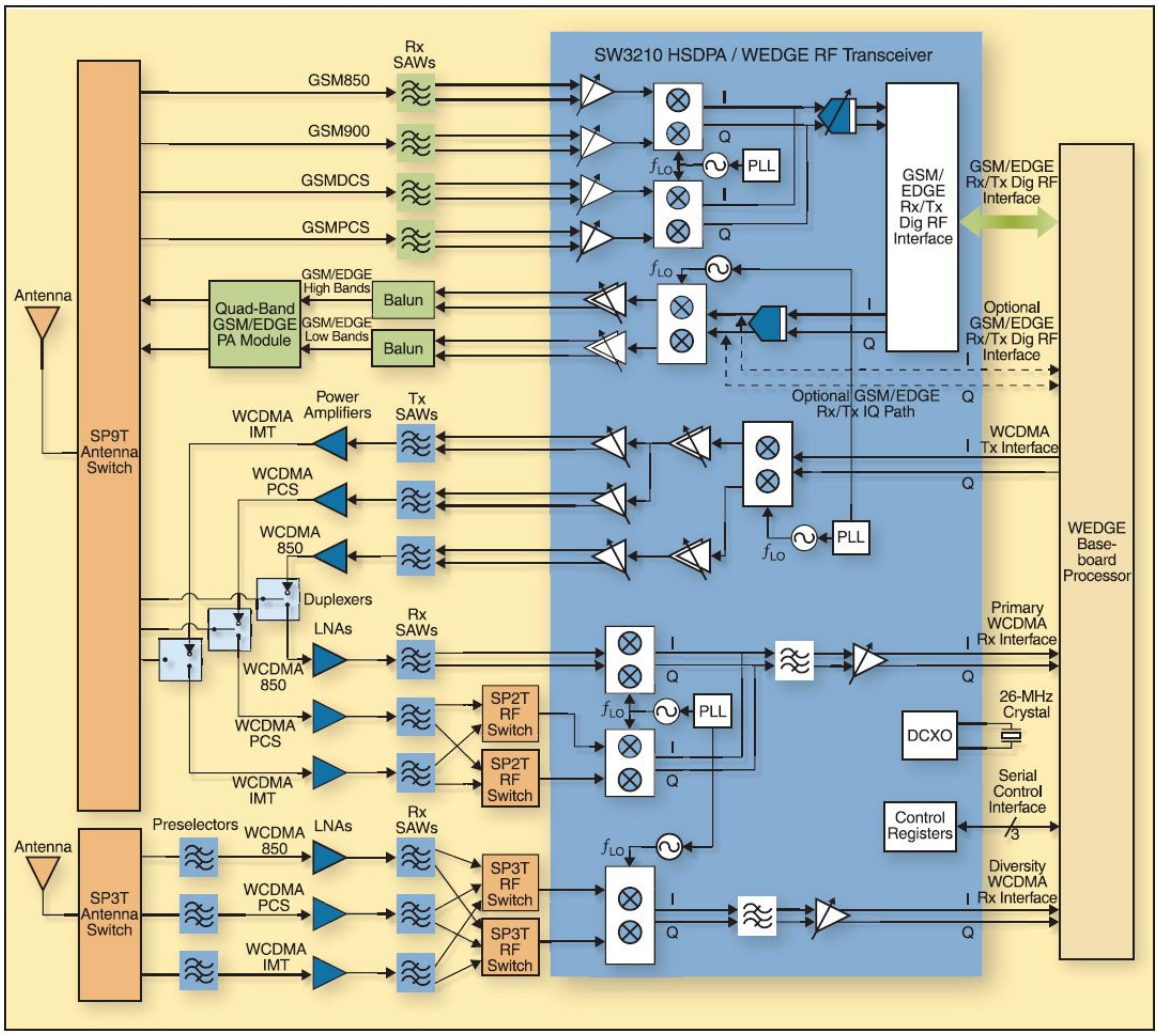

Figure 1.2: System architecture of a RF subsystem with multiple frequency bands diversity [4].

are exploited to adapt hardware parameters to the requested working frequencies and wireless standards. Apparently, in Figure 1.2, if the parallel integration of static filters can be replaced by several tunable filters to support different operation frequency bands, the RF subsystem can be significantly simplified. A concept implementation of tunable RF system is illustrated in Figure 1.3. Tunable matching network and tunable bandpass filters are utilized instead of the parallel integration of static RF components, and the complexity of the system is significantly reduced.

On the device level, high performance tunable RF components are of crucial

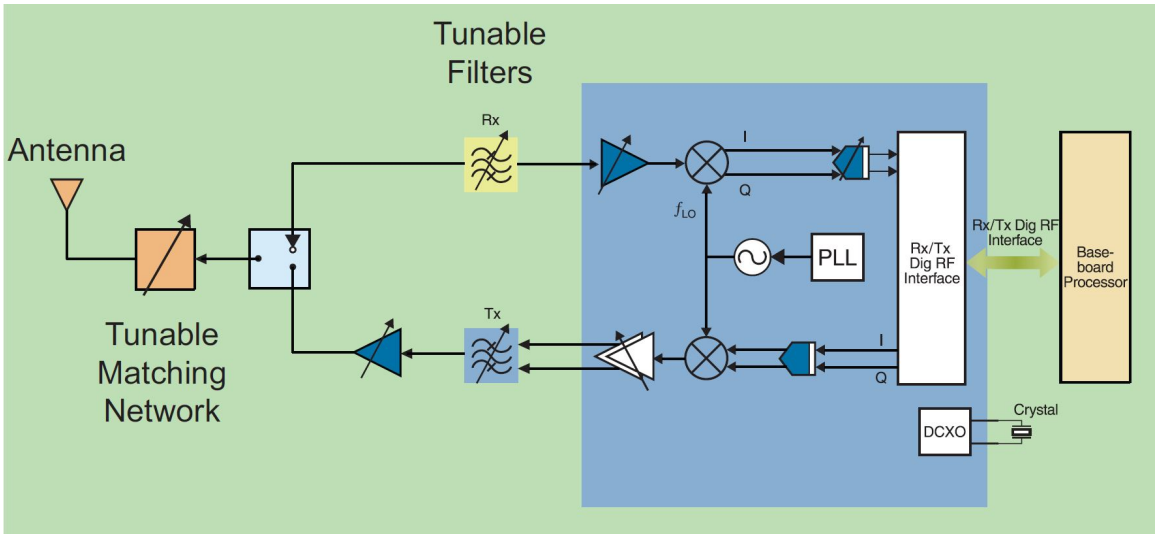

Figure 1.3: A concept implementation of tunable RF front-end.

importance to achieve miniaturized, frequency-agile and multifunctional systems. In order to realize tunable microwave devices, special tuning elements and techniques are required to be used and integrated into the device circuitry. Great efforts have been made to develop tunable microwave components with traditional technologies. Each of these tuning techniques has its own advantages and limitations. The main purpose of this dissertation is to propose a novel methodology for the implementation of electrically tunable microwave components, utilizing the advantages of conventional techniques, and overcoming some of the limitations. Before the description of the proposed design methodology, a general overview and comparison of different tuning technologies is delivered in the next section.

1.2 Tuning Technologies Overview

Extensive tuning technologies have been developed, such as conventional mechanical tuning elements (piezoelectric transducers/actuators), semiconductor varactors (PIN diodes and GaAs Schottky diodes), as well as newer technologies, such as microelectromechanical systems (MEMS). In addition, special functional materials such as ferromagnetic and ferroelectric, are also attractive in recent years for

implementing tunable microwave components.

1.2.1 Mechanically Tunable Techniques

Mechanically tunable technique utilizing piezoelectric transducers or actuators is a relatively early technology to realize tunability. The tuning mechanism is generally shifting a material or tuning screws to affect the resonant frequency or coupling effect of different structures in microwave devices. As presented in [6–8], piezoelectric transducers/actuators are used. Dielectric slab can be either moved vertically above a RF filter, or used to generate deformation on a conductive film to tune the dielectric resonator filters or evanescent-mode cavity filters. The mechanical tuning techniques can provide high-Q and high power-handling capabilities. However, the bulky size of tunable components raises the integration issue, and the low tuning speed (∼ms) greatly limits the utilization in the microwave range.

1.2.2 Semiconductor Varactors

Semiconductor varactors are popular elecments used for tuning, including PIN diodes and GaAs Schottky diodes. The capacitance of a varactor varies as a function of reverse voltage applied across its p-n junction. Basically, the working mechanism of a varactor is based on altering the effective thickness of the depletion region of the junction under a reverse DC voltage, which is equivalently similar to changing the distance of two plates of a capacitor to tune the capacitance. The capacitance is generally inversely proportional to the thickness of depletion zone, while the thickness of depletion region is proportional to the square root of applied voltage. Therefore, the variability of capacitance is inversely proportional to the square root of applied DC voltage [9]. The advantages enabling the popularity of semiconductor varactors are their availability, low cost, high tuning range, and low response time (∼ns), and semiconductor varactors are integrated into extensive microwave

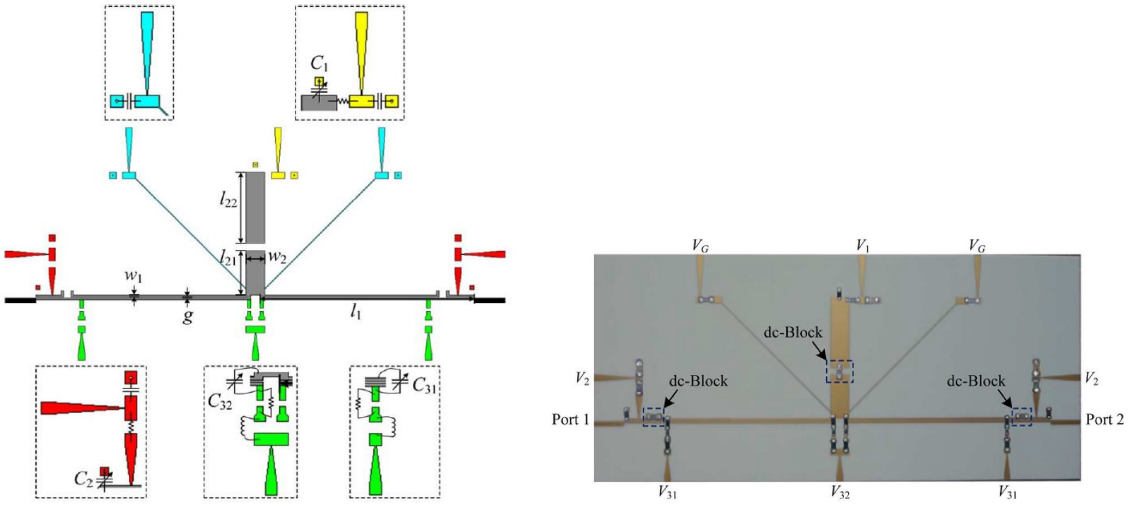

(a) (b)

Figure 1.4: Tunable BPF proposed in [10]: (a) schematic and (b) optical photo.

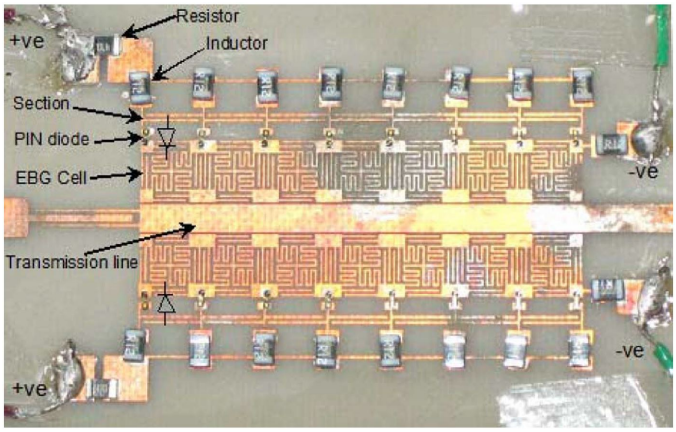

Figure 1.5: Switchable notch UWB tunable BPF in [11].

components to realize tunability. For example, in [10] as shown in Figure 1.4, semiconductor varactors are placed at various internal nodes of a bandpass filter to adjust the transmission poles and compensate the coupling strength, so that the center frequency and bandwidth of the filter can be tunable. In [11] shown in Figure 1.5, semiconductor varactors are embedded to the electromagnetic bandgap (EBG) of a notch filter, to control the connection and disconnection of main EBG unit cell and additional capacitive structures. The size of the EBG unit cell is therefore controllable and the notch band generated by the resonant nature of EBG structure

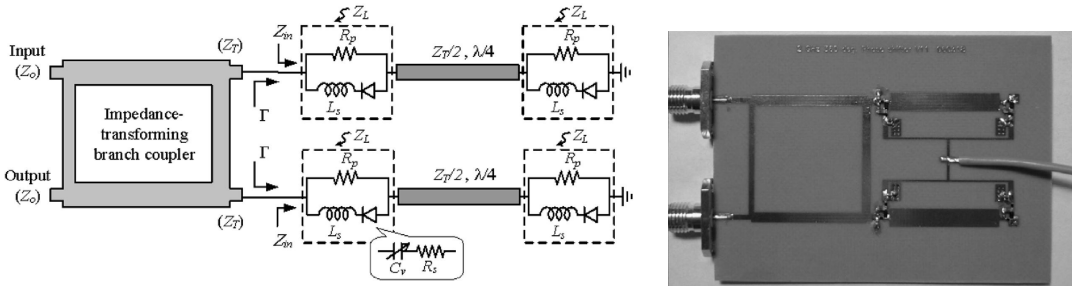

(a) (b)

Figure 1.6: Tunable reflection-type phase shifter in [12]: (a) schematic and (b) optical photo.

is tunable. Semiconductor varactors are used in [12] and incorporated into the impedance-transforming quadrature coupler, which can be seen in Figure 1.6, so that a tunable reflection-type phase shifter is implemented. The major limitations of semiconductor varactors are low quality factor, low power handling capability and low linearity, and PIN diodes consumes some DC power. Moreover, the introduction of semiconductor varactors brings in complicated biasing network and other auxiliary components as well, such as biasing pads, DC block capacitors, RF choke inductors, etc. The varactors and biasing network not only require large area, but also increase the complexity of systems.

1.2.3 RF MEMS Technology

RF MEMS, as an important class of technology, has been successfully applied in tunable RF device topologies. In general, RF MEMS devices enable the micrometer level movement of beams or patches to obtain a switching function or a variable capacitance controlled by applied DC voltage. Low loss is an important merit of RF MEMS devices ($\sim$0.05-0.2 dB in the frequency range of 1-100 GHz for MEMS switches [13]), and they also have high linearity, low power consumption, high capability of power handling, and high isolation (MEMS switches).

The good performance of RF MEMS technology brings in wide utilization

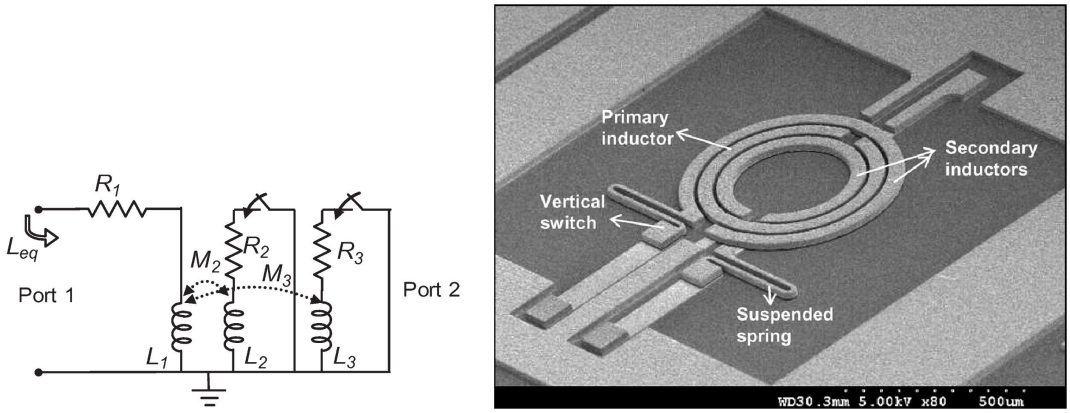

(a) (b)

Figure 1.7: MEMS enabled tunable inductor presented in [14]: (a) schematic and (b) SEM photo.

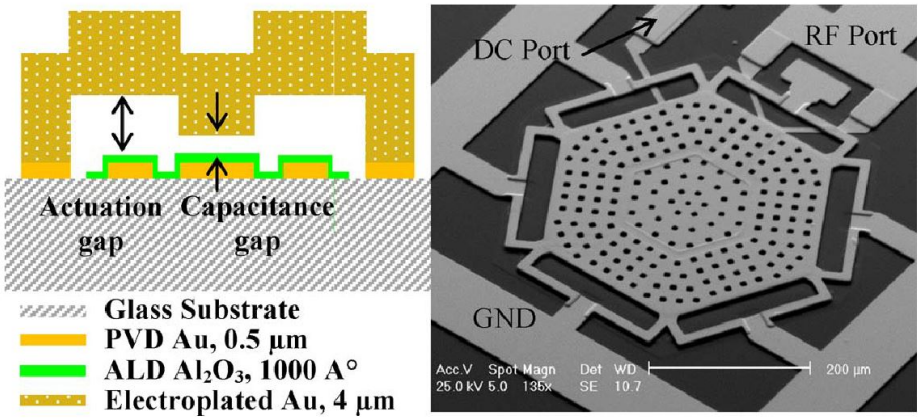

Figure 1.8: MEMS enabled tunable capacitor [15]: cross-section view (left) and top-down SEM photo (right).

in designing tunable microwave components. For example, in [14], RF MEMS technology is used to achieve a tunable inductor with high tuning range and Q factor. The tunability of inductance is enabled by switching the mutual inductance between primary coil and different secondary coils. Figure 1.7 shows the implementation. Yonghyun Shim *et al.* [15] reported a high-Q tunable MEMS capacitor, which is shown in Figure 1.8, with more than 6:1 tunability using multimetal surface micromachining process. The capacitance can be changed by adjusting the deformation of the hexagon patch controlled by DC voltage. Based on the proposed tunable RF MEMS capacitor, Yonghyun Shim *et al.* [16] further constructed a tunable MEMS bandpass filter

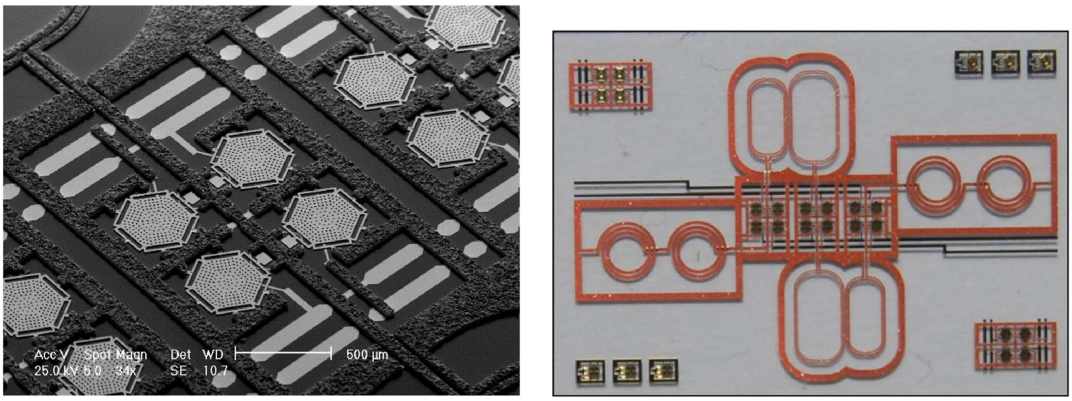

(a) (b)

Figure 1.9: MEMS enabled tunable BPF [16]: (a) SEM photo and (b) optical photo.

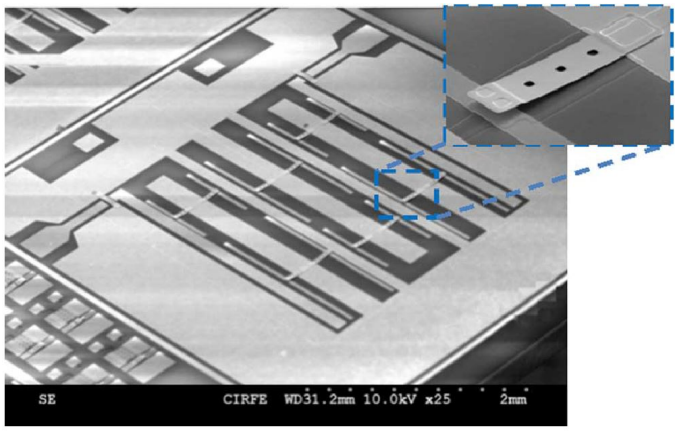

Figure 1.10: SEM image of switchable interdigital filter proposed in [17].

with continuous electrostatic tunability by using three tunable capacitor bands, each consisting of one continuously tunable capacitor and three switched capacitors. Figure 1.9 shows the SEM photo and optical photo. Another tunable RF MEMS bandpass filter is reported in [17], as shown in Figure 1.10, and the pass band can be tuned by switching on and off different resonators enabled by MEMS cantilevers.

The limitations of MEMS technology include high response time ($\sim\mu$s), complicated fabrication and low reliability. Additionally, since MEMS switches can only be switched between the status of on and off, it can only introduce discontinuous tunability.

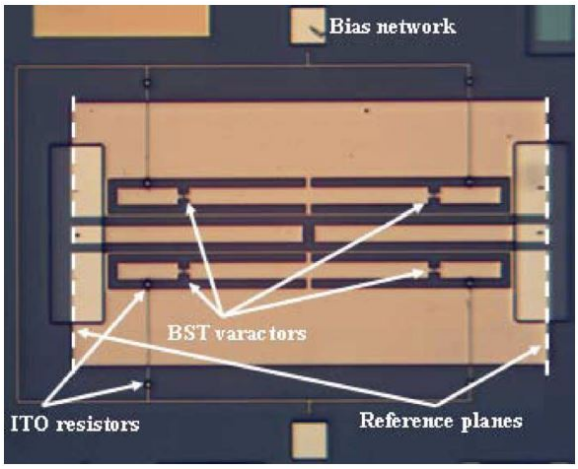

Figure 1.11: Optical image of the Ka-band tunable BPF presented in [22].

1.2.4 Ferroelectric Materials

In addition to the technologies illustrated above, ferroelectric is another category of materials which is also attractive and extensively explored. Barium Strontium Titanate (BST) and Lead Zirconate Titanate (PZT) are among various kinds of ferroelectric materials and have been widely utilized for many microwave applications requiring frequency agility, phase shifting, harmonic generation, or pulse shaping, such as fast tunable delay lines, filters and matching networks, and other electronically reconfigurable architectures [18]. The utility is enabled by the transverse piezoelectric effect and the ability to tune the ferroelectric materials' permittivity with an applied electric field. Therefore, voltage controlled varactors can be constructed by sandwiching a ferroelectric thin film between two metallic electrodes.

BST enabled varactors have been commonly used to control the frequency and/or phase response of various devices [19–23]. For example, in [22], a quasi-elliptic coplanar waveguide tunable bandpass filter operating at Ka-band enabled by BST varactors, shown in Figure 1.11, is reported, and utilizing the epitaxial BST-on-sapphire technology, an U-band filter is for the first time introduced. Yelong Wang *et al.* reported a tunable patch antenna in [23], and Figure 1.12 illustrate

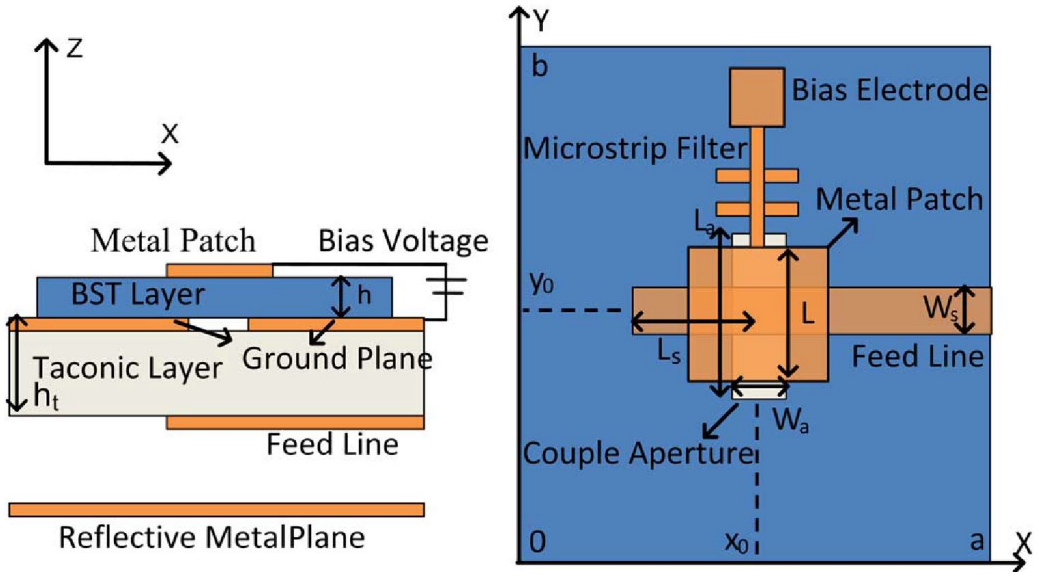

Figure 1.12: Side view (left) and top view (right) of tunable patch antenna using BST as substrate [23].

the schematic of the device. BST layer is used as substrate of the antenna, and the permittivity of substrate can be tuned by applying DC voltage between metal patch and ground such that the resonant frequency of the antenna is varied accordingly. Similar to BST, PZT is another ferroelectric material, and is also widely used for implementing tunable microwave components [24–26].

The main advantages of ferroelectric enabling the popular applications are high and tunable permittivity, low response time (∼ns), and continuous variation of permittivity with the tuning electric field. However, material loss, non-linearity and temperature sensitivity are particular limitations for ferroelectric materials. For most designs, the tuning method is generally limited to DC voltage, which is lack of flexibility.

1.2.5 Ferromagnetic Materials

In recent years, ferromagnetic materials have attracted great attention for their potential applications of performance enhancement, miniaturization and tunability.

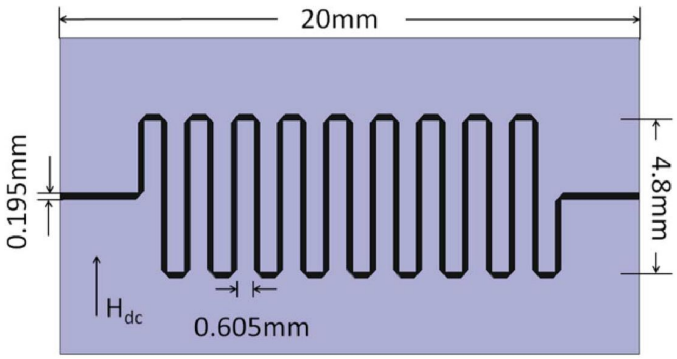

Figure 1.13: Layout of proposed tunable meander line phase shifter in [33] with YIG as substrate.

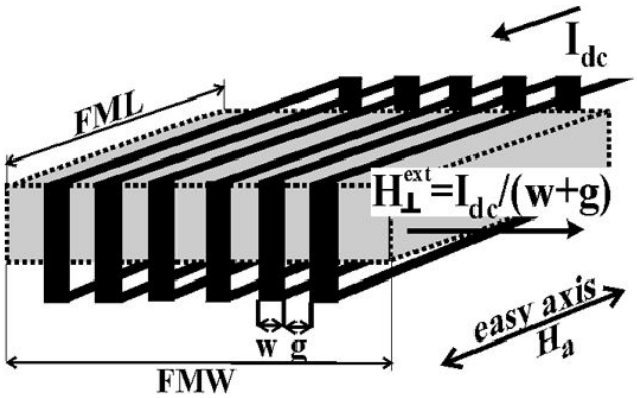

Figure 1.14: Sketch of tunable solenoid inductor with FeNi as magnetic core [34].

The tunable nature of ferromagnetic arises from the adjustable permeability subject to an external biasing magnetic field. Different kinds of ferromagnetic are extensively explored and various tunable microwave components have been developed and realized [27–35].

In [33], Yttrium-Iron-Garnet (YIG) crystal is used as substrate and a tunable phase shifter is reported, which is shown in Figure 1.13. When external biasing magnetic field is provided, the permeability of YIG substrate can be changed and the phase shift is accordingly tuned. However, along with the variation of phase shift, due to the permeability change of substrate, the characteristic impedance of the device is also changed. Marina Vroubel *et al.* reported an electrically tunable solenoid inductor with NiFe used as magnetic core in [34]. Figure 1.14 shows the

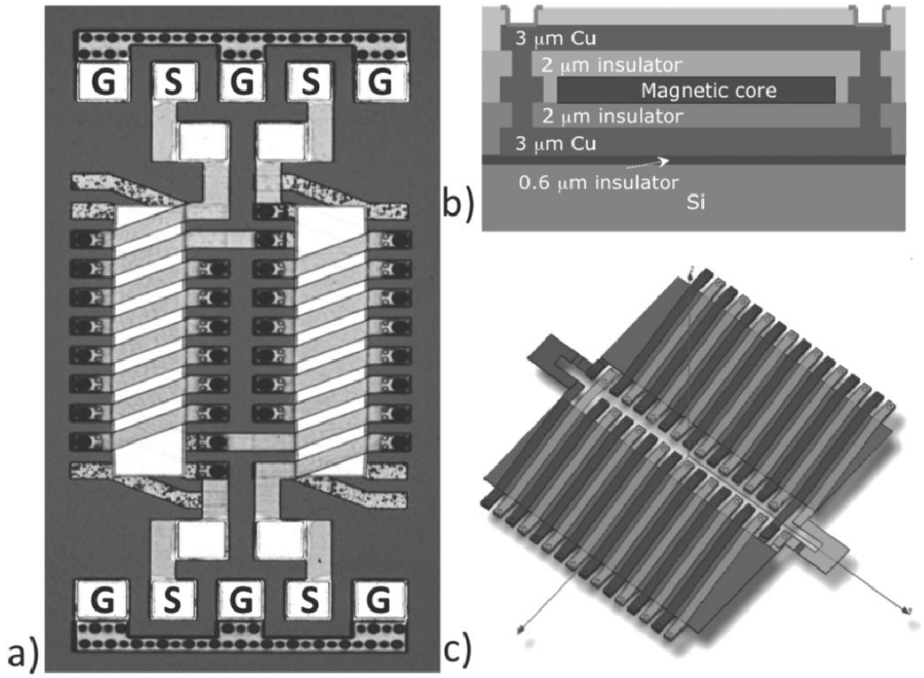

Figure 1.15: Solenoid transformer with laminated Permalloy as magnetic core [35]: (a) top view, (b) schematic of cross-section of transformer layout and (c) illustration of transformer with interleaved coils.

sketch of the device and operation principle. A static magnetic field can be generated when DC current is applied to the solenoid winding. The static magnetic field is oriented parallel to the hard axis of NiFe and change the permeability of magnetic core, resulting in the inductance variety of solenoid inductor. However, due to the bulk utilization of ferromagnetic, the operation frequency of solenoid inductor is limited by the natural ferromagnetic resonant (FMR) frequency, and the tunable inductor can work only below 1 GHz. In [35], Permalloy layers are inserted into coils of transformers. Figure 1.15 illustrates the device. Due to high permeability of Permalloy, the inductance of primary and secondary coils is greatly increased, and the coupling factor is significantly improved.

Overall, high permeability is a primary advantage of ferromagnetic materials, especially the permeability can be continuously tuned by biasing magnetic field. However, similar to ferroelectric materials, low linearity is a limitation for utilizing

Table 1.1: Comparison of Typical Tunable Technologies [13, 36, 37]

Tuning Technology	Mech.[1]	YIG	PIN diode	Varactor diode	BST	RF MEMS
Unloaded Q	>1000	>500	R_s=1-4 Ω	30-50[2]	30-150[2]	50-400
Tuning Speed	>10μs	ns	ns	ns	ns	μs
Bias	>100 V	N/A	10-400 mA	<30 V	<30 V	20-100 V
Linearity (IIP3: dBm)	high	<30	>33	10-35	10-35	>60
Power Handling	high	2 W	∼mW	∼mW	∼mW	1-2 W
Power Consumption	high	high	medium	low	negligible	negligible
Size	large	large	small	small	small	small
Cost	high	high	low	low	low	medium
Integration	difficult	difficult	good	good	good	good

Mechanical[1]
At 10 GHz[2]

ferromagnetic materials in designing microwave components. Moreover, for most tunable implementations enabled by ferromagnetic materials, external magnetic biasing field is required, which apparently introduces the integration issue.

1.3 Research Objective and Dissertation Overview

Table 1.1 summarizes the performance comparison among different tunable technologies reviewed in the previous section. Obviously, each of the existing tunable technologies has different advantages and limitations. The choosing is strongly depended on the particular system specifications.

Following the motivation and literature review demonstrated in the previous sections, the primary objective of this research is to use the advantages of conventional techniques and solve some of the limitations, and develop a new solution for tunable microwave applications. In this dissertation, the concept of dual tunability is

introduced and a novel methodology is proposed for implementing fully electrically tunable microwave components by integrating both selectively patterned Permalloy and PZT thin films. To fully illustrate the design methodology and validate the efficacy, the research is divided into three primary parts, and accordingly four main chapters are incorporated in the dissertation to deliver detailed description.

• *Part I: Demonstrate the concept and topology of selectively patterned Permalloy thin film enabled electrical tunability*

In Chapter 2, the idea of Permalloy thin film enabled electrical tunability is presented and tunable microwave transmission line is implemented utilizing this design topology. First, the ferromagnetic properties of Permalloy is presented in detail, and the working principle of selectively patterning Permalloy thin film to increase ferromagnetic resonant (FMR) frequency is theoretically analyzed and validated with magnetic simulation results. The selectively patterned Permalloy thin film is deposited on top of the signal line of coplanar waveguide (CPW) transmission line, and the performance of different orientations of thin film pattern parallel and perpendicular to the signal line is then compared and discussed respectively with measurement results. Permalloy thin film is integrated into conventional transmission line as a part of signal line, and thus no extra area or components is introduced. Instead of conventional tuning method utilizing external biasing magnetic field, DC current is applied between the two ports of CPW transmission line to generate static magnetic field for tuning the permeability of Permalloy thin film pattern [38]. The permeability variation of Permalloy thin film results in the tunability of signal line inductance density, and the electrically tunable transmission line is achieved. The detailed electrically tuning mechanism is illustrated. The tunability is strongly dependent on the tuning static magnetic field, while the magnetic field intensity is related to both the amount of DC current and signal line width. A group of transmission lines with different signal line widths is fabricated and measured to

analyze and demonstrate this effect. To improve the performance, new configuration of Permalloy thin film is theoretically explored and lamination structure is proved to be effective to increase the tunability.

• *Part II: Validate the topology efficacy of patterned Permalloy thin film enabled electrical tunability for tunable microwave devices*

Part I introduces the topology of Permalloy enabled electrical tunability. To prove the feasibility of this design method, in Chapter 3, patterned Permalloy thin film is successfully utilized in implementing electrically tunable inductors. Exploiting the high and tunable permeability, Permalloy thin film is at first integrated with spiral inductors to improve the performance and achieve tunability. The inductance and quality factor (Q factor) are significantly enhanced compared with regular spiral inductor without Permalloy, and the inductance can be tuned by DC current. Due to the selective patterning of Permalloy thin film, the operation frequency of tunable inductor reaches to several GHz. The performance of tunable spiral inductors with different thickness of Permalloy thin film is analyzed and discussed to provide clues for future optimization and improvement. In addition to the tunable spiral inductor, Permalloy thin film is then used to achieve a tunable 3-D solenoid inductor. Special configuration is adopted and patterned Permalloy thin film is used as magnetic core of solenoid inductor. Compared with the distribution of static magnetic field surrounding a metal wire generated by DC current, the magnetic field inside the solenoid winding is more uniform to tuned the permeability of Permalloy thin film. Therefore, compared to tunable spiral inductor, 3-D solenoid inductor more effectively use the DC current for tuning and larger tunability is achieved.

Chapter 4 proposes a prototype implementation of tunable bandpass filter (BPF) utilizing the concept of Permalloy enabled tunable transmission line, and further validates the efficacy of this design topology. The BPF is constructed with electromagnetic bandgap (EBG) resonators and working at 4 GHz. Permalloy thin

film is nano-patterned with e-beam (electro-beam) lithography to improve the FMR frequency and support the operation frequency of BPF. The center frequency of the BPF can be tuned when DC current is applied between input and output ports.

• *Part III: Demonstrate the methodology of Permalloy and PZT enabled dual tunability for fully electrically tunable microwave applications*

Part I and Part II of the research comprehensively demonstrate and validate the topology of Permalloy enabled electrical tunability. In Part III, a new design methodology integrating both Permalloy and PZT are demonstrated and validated for designing tunable microwave components. Permalloy introduces inductive tunability and PZT is capable of realizing capacitive tunability. By combining both inductive and capacitive tunability, the concept of dual electrical tunability is introduced and achieved. Chapter 5 demonstrates the dual tunability and dual tunability enabled characteristic impedance retaining capability, with several tunable microwave components implemented as validation.

This chapter is divided into two sections. The first section demonstrates a step impedance coplanar waveguide (SI-CPW) slow wave transmission line. Patterned Permalloy thin film is deposited on top of the high impedance sections of signal line to improve the inductance density, while PZT thin film is deposited into the gap between low impedance sections of signal line and ground to increase the capacitance density. The integration of Permalloy and PZT thin film not only enhances the performance, but also enables dual tunability of SI-CPW transmission line. When DC current and DC voltage are provided, the electrical length of transmission line can be inductively and capacitively tuned simultaneously, and equivalently the phase shift can be tuned. The dual tunability enabled characteristic impedance retaining capability is introduced and proved in this section.

Section two proposes a 3-D lumped elements electrically tunable phase shifter. The tunable solenoid inductor proposed in chapter 3 is used to construct the phase

shifter, and PZT thin film enabled tunable metal-insulator-metal (MIM) is introduced in stead of PZT gap capacitance utilized in the SI-CPW slow wave transmission line to increase the capacitance and reduce the tuning DC voltage. Compared with SI-CPW phase shifter, due to the utilization of optimized 3-D structure, significantly larger electrical tunability is achieved with much lower tuning DC current and DC voltage. The phase shift can be tuned electrically while the equivalent characteristic impedance is kept constant by selectively applying DC current and DC voltage, and the efficacy of characteristic impedance retaining is further validated.

As demonstrated above, the main body of research is presented in Chapter 2, 3, 4 and 5. The dissertation is concluded in Chapter 6. The author's work is summarized and contributions are itemized in this chapter. Future work of research is also provided.

Chapter 2

Permalloy and Permalloy Enabled Tunable Microwave Transmission Line

In Chapter 1, a general overview on microwave tunable techniques has been introduced. State-of-art tuning technologies including mechanical methods, semiconductor varactors, RF MEMS, ferroelectric and ferromagnetic materials and their utilization in the realizations of tunable microwave applications have been discussed and presented. Advantages and limitations of different tunable technologies are compared and analyzed. As demonstrated before, the main purpose of this dissertation is proposing a new design methodology to implement electrically tunable microwave components by integrating both ferromagnetic and ferroelectric materials, and achieve smart tunable microwave applications with dual electrical tunability. In literature review of the previous chapter, for most conventional tunable designs exploiting ferromagnetic materials, external biasing magnetic field is required for tuning, which apparently results in the integration issue. Therefore, before realizing dual electrical tunability, electrically tuning ferromagnetic materials must be achieved first. This chapter demonstrates the utilization of Permalloy, a kind of ferromagnetic material with good properties, and the operation mechanism of electrically tuning of Permalloy. Based on that, Permalloy enabled electrically tunable microwave transmission line is implemented.

This chapter begins with the introduction of classification of magnetism and magnetic materials. Then, fundamentals of ferromagnetic materials are

discussed and presented. The working principle of Permalloy enabled electrical tunability is analyzed and demonstrated afterwards and utilizing the results of theoretical discussion and analysis, electrically tunable microwave transmission line is implemented.

2.1 Classification of Magnetism

The phenomenon of magnetism can be presented macroscopically and microscopically [39, 40]. In macroscopical, materials react attractively or repulsively when they are exposed to other materials. In microscopical, magnetism is mainly due to the electrons of the atom, which have a magnetic moment originating from their motion. Even though nucleus also has a small magnetic moment, it is negligible compared with that of the electrons, and it has insignificant effect to the gross magnetic properties. For electrons, there are two kinds of motions, spin and orbital, and correspondingly two magnetic moments are associated with them, which are spin magnetic moment and orbital magnetic moment, respectively. In materials, atoms contain many electrons, and each electron spins about its own axis and moves along its own orbit. Since the magnetic moments associated with the two kinds of motions are vector quantity, the magnetic moment of the atom is the total vector sum of all its electronic moments. Accordingly, two possibilities can be raised and five kinds of magnetism can be classified:

1. The magnetic moments of all the electrons are oriented in a way that they cancel out each other, and the atom as a whole has no net magnetic moment. This mechanism results in diamagnetism.

2. The magnetic moments of all the electrons are partially canceled and the atom is left with a net magnetic moment, which is referred to as magnetic atom. This leads to paramagnetism, ferromagnetism, antiferromagnetism or ferrimagnetism.

Diamagnetism

Diamagnetism is a kind of very weak magnetism form. When no external biasing magnetic field is applied, there is no net magnetic moment in atoms of diamagnetic substances. However, when magnetic field is provided, the magnetization is produced, which is oriented in the opposite direction of the external magnetic field, and is strengthened as the increasing of biasing magnetic field. The susceptibility of diamagnetic materials, which is defined as the variation in magnetization with respect to the applied magnetic field, is small and negative, and is independent of temperature. The typical diamagnetic materials include He, Au and Cu.

Paramagnetism

Compared with diamagnetism, paramagnetic materials are composed of atoms or ions which have a net magnetic moment due to non-cancellation of the spin and orbital components. The coupling between magnetic moments are weak, so their alignment is random as a result of thermal energy. When external magnetic field is applied, the magnetic moments are aligned toward the same direction as magnetic field. However, due to the relatively small external magnetic field energy compared to thermal energy, only a small fraction of magnetic moments can be aligned so as to strengthen the practical field and magnetization. Therefore, the susceptibility of paramagnetic materials is positive and small. Moreover, the susceptibility is temperature dependent. When the temperature is increased, the thermal agitation enhances the randomization of magnetic moments alignment, resulting the variation of susceptibility. Some examples of paramagnetic materials are Ni, Fe and Co.

Ferromagnetism

Ferromagnetism is one of the strongest forms of magnetism. The most important characteristic property of ferromagnetic materials is spontaneous magnetization, resulting from the alignment of the magnetic moments located on an atomic lattice. The magnetization tends to lie along easy directions that are decided by crystal structure, atomic-scale texture or sample shape, even though external magnetic field is absent. The quantum mechanics can be described by Heisenberg model, which demonstrates the parallel alignment of magnetic moments introduced by exchange interaction between adjacent moments. The parallel alignment of the magnetic moments in ferromagnetic materials results in a strong internal magnetic field, and the susceptibility of ferromagnetic materials are positive and very large, as high as 10^6. The common ferromagnetic materials are Fe, Ni and Co.

Antiferromagnetism

Antiferromagnetism is different from ferromagnetism particularly in the manner of spin alignment. In antiferromagnetic materials, the exchange interaction between neighboring atoms results in anti-parallel alignment magnetic moments, and the magnetic moments with opposite direction cancel each other, showing no net magnetization as paramagnetic materials. Therefore, the susceptibility of antiferromagnetic materials is positive and very small. Some common materials of antiferromagnetism are Cr, FeO and MnO.

Ferrimagnetism

Ferrimagnetism is another kind of magnetic ordering. In terms of magnetic moments alignment resulted from exchange interaction, ferrimagnetism is similar to antiferromagnetism, and magnetic moments are anti-parallel aligned. However,

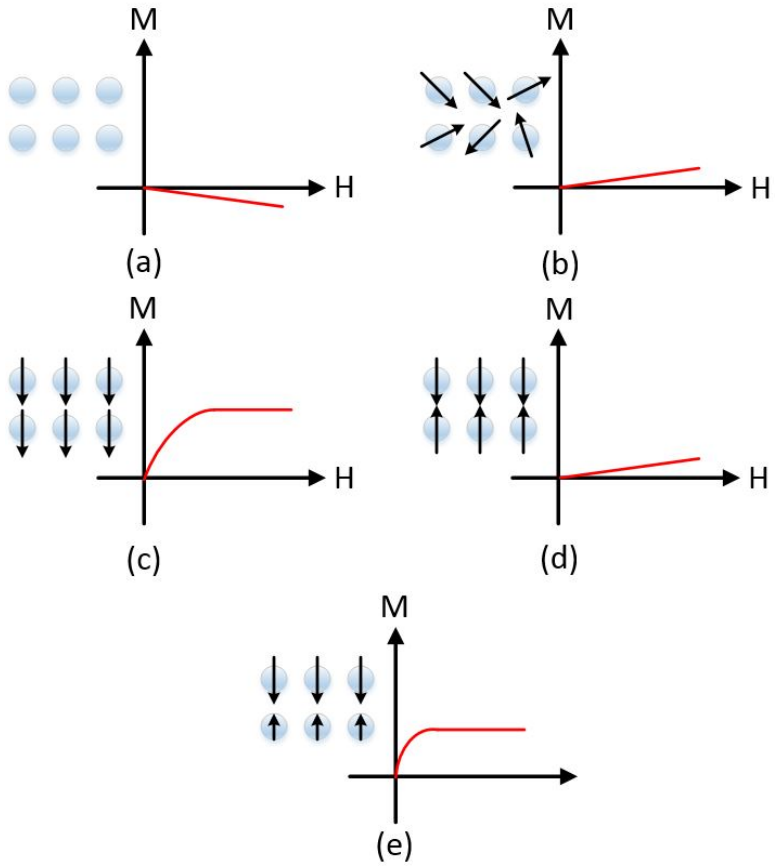

Figure 2.1: Magnetic moments ordering and M−H relation of (a) Diamagnetism, (b) Paramagnetism, (c) Ferromagnetism, (d) Antiferromagnetism and (e) Ferrimagnetism.

the anti-parallel aligned magnetic moments do not cancel each other so that the net magnetization is not zero in the materials. Therefore, ferrimagnetic materials behave similarly to ferromagnetic materials, except that the susceptibility is much lower. One of the most commonly used ferrimagnetic materials is Fe_3O_4. Other examples include MnZn and NiZn.

According to the ordering of magnetic moments, ferromagnetic, antiferromagnetic and ferrimagnetic materials are called magnetically ordered materials, while diamagnetic and paramagnetic materials are non-magnetically ordered due to the fact that no ordering in magnetic moments exists without the presence of applied external magnetic field. Figure 2.1 summarizes and illustrates the magnetic moments

orderings and M−H relations of five types of magnetism.

2.2 Ferromagnetic Materials

During the last decades, ferromagnetic materials have been greatly explored and developed, and become one of the most widely used materials among all kinds of magnetic materials because of their potential in a wide range of applications [41–44].

2.2.1 Fundamental Concepts

Some of the fundamental concepts and properties of ferromagnetic materials, such as magnetic energy, domain, hysteresis, and ferromagnetic resonance (FMR) frequency, are introduced as following.

Magnetic Energies

In magnetic materials, the most important energy is the exchange energy, which can be denoted as E_{ex}. The exchange energy illustrates the exchange interactions between two neighboring electrons, and as demonstrated before, those interactions contribute to parallel aligning adjacent atomic magnetic moments in the ferromagnetic materials, resulting in an internal magnetic field even without external applied magnetic field. The exchange interaction can be explained by Coulomb repulsion and Pauli exclusion principle, which sate that two electrons can not occupy the same quantum state within a quantum system. In a atomic system with many electrons, the total energy is denoted by Exchange Hamiltonian [45, 46]:

$$E_{ex} = \mathcal{H} = -2\sum_{i \neq j} J_{ij} S_i \cdot S_j \tag{2.1}$$

where S_i and S_j are the sum of all the atoms pairs on lattice sites i and j, respectively. J_{ij} is the exchange integral between S_i and S_j. When only nearest neighboring interactions are considered, J_{ij} can be simplified to a single exchange constant J.

If $J < 0$, equation 2.1 indicates antiferromagnetic interaction, which antiparallel aligns the two spins in the antiferromagnetic materials. When J is a positive value, it describes ferromagnetic materials, in which ferromagnetic interaction tends to parallel align two spins.

Another important type of magnetic energy is anisotropy energy E_a, which illustrates the phenomenon that magnetic moments tend to be aligned along the easy axis of the ferromagnetic materials. There are several kinds of anisotropy [39], including magnetocrystalline anisotropy, shape anisotropy, stress anisotropy, exchange anisotropy and anisotropy induced by process such as magnetic annealing, plastic deformation and irradiation. Among those anisotropy, only magnetocrystalline anisotropy is the intrinsic property of materials. Then, strictly, all the others are extrinsic or induced.

The magnetocrystalline anisotropy originates from the crystal−field interaction and spin−orbit coupling, or other inter-atomic dipole-dipole interaction [40]. When external magnetic field is applied trying to reorient the spin of an electron, the orbit of the electron tends to be reoriented as well due to the spin-orbital coupling. However, the orbit is strongly coupled to the crystal lattice and resists the attempt to rotate the spin axis. Then the magnetocrystalline anisotropy is defined as energy required to rotate the spin system of a domain away from the easy axis to the hard axis, which is also the energy to overcome the spin-orbit coupling. The expression for this energy is different according to the symmetries of materials. For a ferromagnetic material with uniaxial anisotropy, the magnetocrystalline anisotropy can be expressed as:

$$E_a = K_{u1} sin^2\theta + K_{u2} sin^4\theta + K_{u3} sin^6\theta + \cdots \tag{2.2}$$

where K_{un} are the anisotropy constants, θ is the angle between magnetization direction and easy axis.

The anisotropy can also be originated due to the shape of ferromagnetic samples, which is called shape anisotropy, and is highly related with our research in this

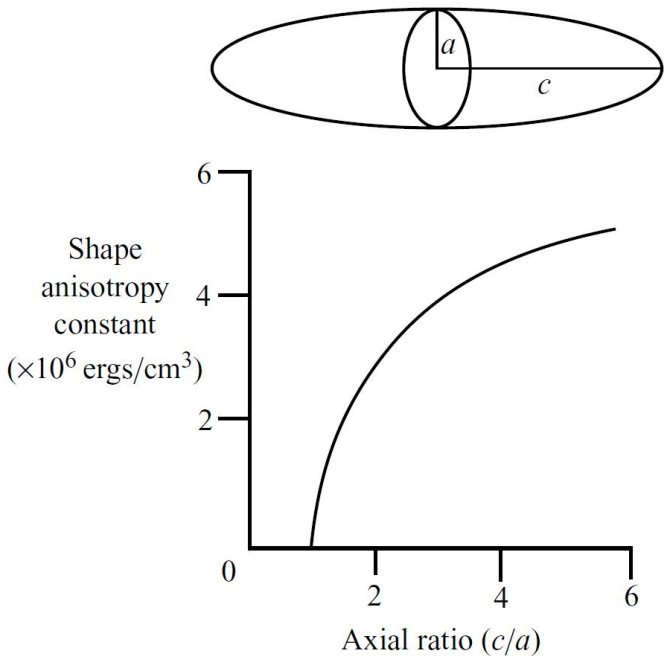

Figure 2.2: Shape anisotropy constant in a prolate spheroid of Co as a function of aspect ratio [47].

dissertation. If the shape of the ferromagnetic sample is spherical, the same applied magnetic field can magnetize the sample to the same extent in every direction. However, when the shape of the sample is non-spherical, magnetizing the sample along its long axis is easier than along a short axis, which is because the demagnetization field along the long axis is smaller than that along the short axis. Increasing the aspect ratio of sample can effectively increase the shape anisotropy energy. Figure 2.2 illustrates the shape anisotropy constant of Co as a function of aspect ratio. In our research in this dissertation, the ferromagnetic material is selectively patterned to increase the aspect ratio, so that the shape anisotropy is enhanced and the high frequency performance of the ferromagnetic materials is improved, which will be demonstrate in the following sections.

The magnetostatic energy E_{ms} is a type of magnetic energy generated by the demagnetization field in the sample [39]. Figure 2.3 illustrates the formation mechanism of demagnetization field. Suppose a prolate spheroid is magnetized by

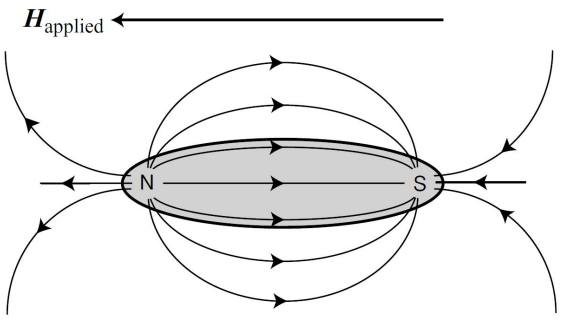

Figure 2.3: Magnetic field around a prolate spheroid [47].

an applied magnetic field, and a north pole and a south pole are generated at the two ends of the prolate spheroid, respectively. The magnetic field lines radiate from the north pole to the south pole outside the sample, while the magnetic field inside the sample is oppositely oriented, which tends to demagnetize the sample, and is called demagnetization field. The magnetostatic energy thus can be expressed, based on demagnetization field, as [39]:

$$E_{ms} = -\frac{1}{2}\int H_d \cdot M dv \tag{2.3}$$

where H_d is the demagnetization field, and M is the magnetization field of the sample. Accurately evaluating the distribution of H_d is difficult, and the demagnetization factor is introduced to calculate H_d:

$$H_d = -N_d M \tag{2.4}$$

where N_d is the demagnetization factor and it is a tensor strongly dependent on the shape of the magnetic sample. The detailed calculation methods can be referenced in [39].

For a magnetic sample, when an external biasing magnetic filed is provided, the Zeeman energy E_z is generated, which can be described as:

$$E_z = -\mu_0 \int H_{app} \cdot M dv \tag{2.5}$$

where H_{app} is the applied magnetic field, and M is the local magnetization. The Zeeman energy is minimized when H_{app} is parallel to M.

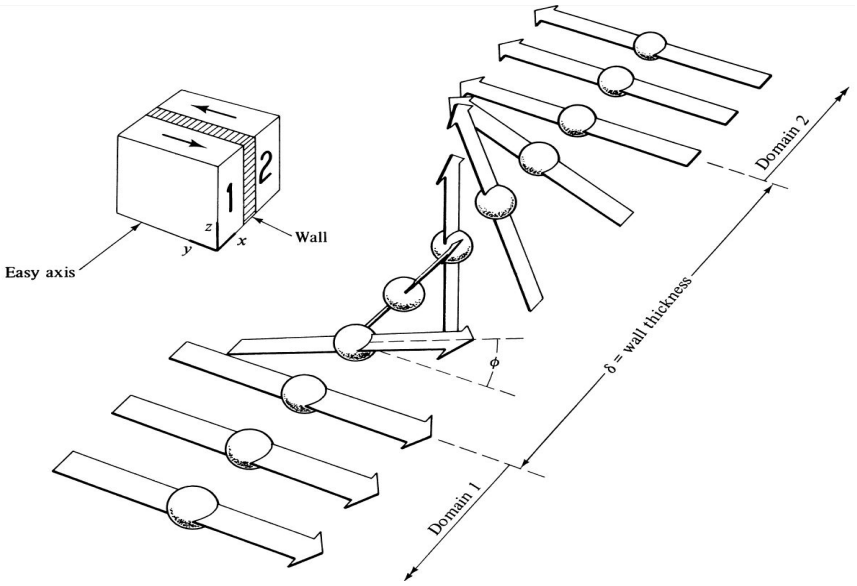

Figure 2.4: Structure of a 180° domain wall [39].

The final magnetization state and properties of the ferromagnetic sample is determined by the minimization of the sum of those energies described above.

Domain

Ferromagnetic materials have internal magnetic field due to the spontaneous alignment and magnetization, even in the absence of an applied magnetic field. However, the net magnetization of ferromagnetic materials as a whole is zero in the demagnetized state. The reason is that ferromagnetic material in the demagnetized state is divided into domains, within each of which all the magnetic moments are parallel aligned to each other. The boundaries between domains are domain walls, across which the direction of magnetic moments alignment gradually changes to a different one. Figure 2.4 illustrates the structure of a domain wall. When ferromagnetic materials are in the demagnetized state, the orientation of magnetic moments in domains are with such different directions that they can cancel each other, and therefore the net magnetization is zero. The direction along which the magnetic moments are aligned in a domain is its easy axis, and the direction perpendicular to

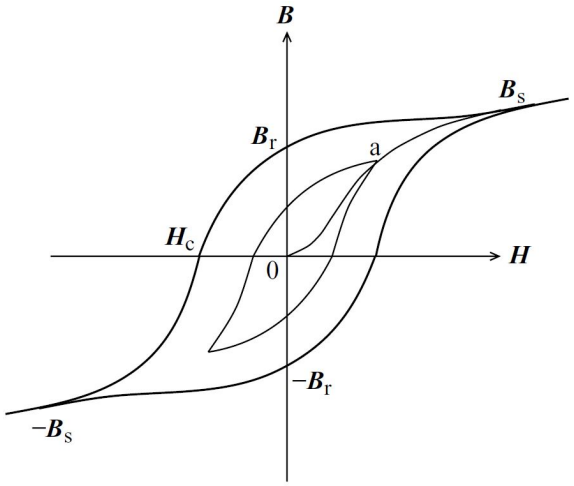

Figure 2.5: Hysteresis loop for a ferromagnetic [47].

the easy axis is hard axis. The easy axis indicates the direction of magnetic moments alignment which enables the domain in the lowest energy level, and the formation of domain structures contributes to minimize the total magnetic energy of ferromagnetic materials.

Hysteresis

Another phenomenon of ferromagnetic materials is the nonlinear magnetization behavior subject to an external magnetic field, and the magnetization curve is usually a hysteretic loop, which is demonstrated in Figure 2.5.

In the initial unmagnetized state, domains are oriented randomly so that the net magnetization is zero. When an external field is applied, the domains, of which the magnetization direction is similar to the external magnetic field, begin to grow, causing domain wall movement, while other domains with unfavorable magnetization orientation are shrunk. As the applied magnetic field is increased in the positive direction, the magnetic induction follows the curve from 0 to B_s and eventually the magnetization is saturated and saturation induction B_s is reached, where all the domain walls in the ferromagnetic materials are eliminated and a single domain is formed. It is notable that although magnetization is constant after saturation, B

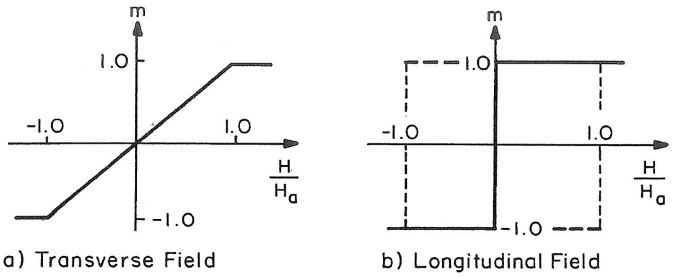

Figure 2.6: Hysteretic loops for two idealized magnetization cases: (a) hard−axis and (b) easy−axis magnetization process [48].

continues to increase along with H, due to $B = H = 4\pi M$. The curve of B from demagnetized state to saturation induction B_s is called the normal induction curve.

After the saturation, when applied magnetic field H is reduced to zero, the magnetic induction drops from B_s to B_r, which is called residual induction. The reason of the generation of residual induction is that domain walls are unable to fully reverse their motions back to the original positions even in the absence of external magnetic field. When the applied magnetic field is reduced in the negative direction, the magnetic induction is decreased to zero, where the required magnetic field is called coercivity (H_c). The coercivity is related to the hysteretic loss. A smaller coercivity value can introduce lower hysteretic loss.

When the reversed external magnetic field is further increased, the reverse saturation ($-B_s$) is achieve. The loop traced out from $-B_s$ to B_s is called the major hysteresis loop, and the loop is inversely symmetric about the origin.

The smaller loop inside the major hysteresis loop in Figure 2.5 is called minor hysteresis loop, which illustrates the case when initial magnetization is interrupted (for example, at point a shown in the figure) and magnetic field H is reversed.

Generally, magnetization processes along easy axis and hard axis are different [48], which show different appearances of hysterestic loops. For uniaxial ferromagnetic materials, a purely hard−axis magnetization process involves rotation movement of domain orientation into the direction of external applied magnetic field, which results

in a linear magnetization−magnetic field (M−H) loop. An easy−axis magnetization is related to domain wall movement in a direction that grows the favorably oriented domain. Figure 2.6 demonstrates the two idealized magnetization processes along hard axis and easy axis, respectively.

Ferromagnetic Resonant Frequency

The phenomenon of ferromagnetic resonant (FMR) was firstly observed in 1946 by Griffiths [49] and the theory was developed by Kittel in 1948 [50]. When a microwave signal is applied to a ferromagnetic sample and the sample is subject to a static magnetic filed, the magnetic moments precesses about the direction of the applied static magnetic field, and the microwave power is strongly absorbed if the frequency of the microwave transverse field is equal to the precessional frequency of the magnetic moments. In the absence of damping, the equation of motion can be expressed as [45]:

$$dM/dt = \gamma(M \times B_0) \tag{2.6}$$

where M is magnetization of the ferromagnetic sample, γ is the gyromagnetic ratio, and B_0 is the applied static magnetic field. The magnetization precesses at the Larmor frequency $f_L = \omega_0/2\pi$, where $\omega_0 = \gamma B_0$. The magnetization of the ferromagnetic is mainly due to the spin moments of the electrons, so the gyromagnetic ratio(γ) can be expressed as $\gamma = -(e/m_e)$, where m_e is the mass of an electron. The applied static magnetic field is usually replaced by the effective field H_{eff}, which takes anisotropy field into consideration, and Equation 2.6 can then be revised as:

$$dM/dt = \gamma(M \times B_{eff}) \tag{2.7}$$

Based on Equation 2.7, the famous Kittel's equation can be derived [45, 50] and used to estimate the FMR frequency:

$$\omega_0^2 = \frac{\gamma^2}{4\pi^2}[H_0 + H_{ani}(N_x - N_z)4\pi M_s][H_0 + H_{ani}(N_y - N_z)4\pi M_s] \tag{2.8}$$

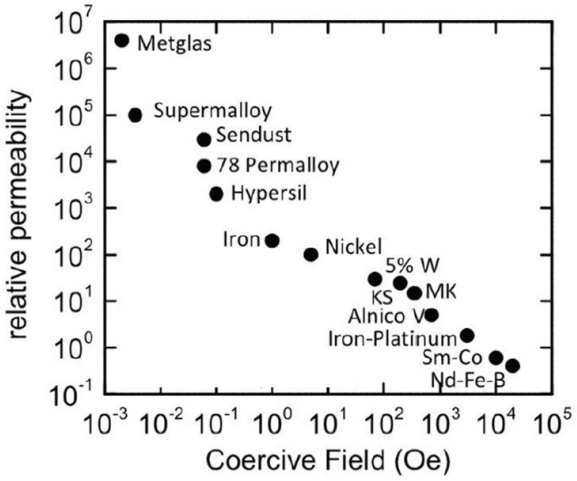

Figure 2.7: Comparison of different ferromagnetic materials regarding to coercivity and relative permeability [54].

where H_0 is the applied static magnetic field, H_{ani} is the anisotropy field, and M_s is the saturation magnetization; N_x, N_y and N_z are demagnetization factors along x, y and z direction, respectively. Some special cases are:

- Sphere: $N_x = N_y = N_z = \frac{1}{3}$, and then $\omega_0 = \frac{\gamma}{2\pi} H_0$;
- Thin film with static magnetic field perpendicular to the plane: $N_x = N_y = 0$, $N_z = 1$, and then $\omega_0 = \frac{\gamma}{2\pi}(H_0 - H_{ani} 4\pi M_s)$;
- Thin film with static magnetic field in plane: $N_y = N_z = 0$, $N_x = 1$, and then $\omega_0 = \frac{\gamma}{2\pi}[H_0 + H_{ani} 4\pi M_s)]^{(1/2)}$

2.2.2 Permalloy Thin Film

Among all kinds of ferromagnetic materials, Permalloy (Py) has been extensively explored and developed. Py is composed of 80% of Nickel (Ni) and 20% of Iron (Fe), and has good ferromagnetic properties such as large and tunable permeability, small magnetostriction, low coercivity, and no stress anisotropy [51–53]. Figure 2.7 demonstrates the comparison of Py with other ferromagnetic materials regarding to coercivity and relative permeability. It is clearly shown that compared with most of

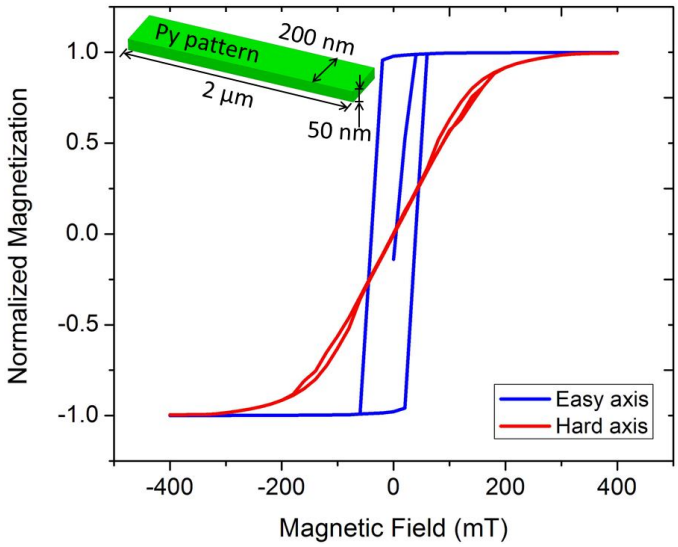

Figure 2.8: Simulated hysteresis loop of patterned Py thin film along easy axis and hard axis.

ferromagnetic materials, Py has larger relative permeability and smaller coercivity. The hysteresis loss of ferromagnetic materials is highly related to coercivity, and small coercivity can contribute to reduce the magnetic hysteresis loss. According to previous demonstration and Figure 2.6, magnetization along the hard axis of ferromagnetic materials has smaller coercivity than easy axis magnetization. To theoretically show the different hysteresis loop and coercivity of Py along easy and hard axis, magnetic simulation using Object Oriented Micromagnetic Framework (OOMMF) [55] is conducted. 50 nm thick Py thin film is patterned as a slim bar with the length of 2 μm and width of 200 nm. In this dissertation, standard parameters for Py (gyromagnetic ratio γ=2.8 GHz/kOe, exchange constant $A = 13 \times 10^{-12}$ Jm^{-1}, damping constant α=0.015, and anisotropy constant K_U=0) are used in all the magnetic simulation with OOMMF. Figure 2.8 shows the simulation results. It is clearly shown that compared with easy axis magnetization, the coercivity of hard axis magnetization is negligible. In this dissertation, the external biasing magnetic field is always parallel to the hard axis of the Py pattern to reduce the hysteresis loss. Most importantly, external biasing magnetic parallel to the hard axis can perform the

tuning of permeability of Py thin film, which will be demonstrated in the following section.

FMR frequency is a key factor of ferromagnetic material and it indicates the operation frequency limitation of utilizing Py in designing tunable microwave components. Py shows high and tunable permeability only when the working frequency is below FMR frequency, and if the working frequency exceeds the FMR frequency, the permeability becomes very low and even negative. However, the FMR frequency of un-patterned Py thin film is usually below 1 GHz, which apparently limits the utilization of Py on the microwave frequency range. The method to improve FMR frequency is indicated in Equation 2.8 by increasing the anisotropy field H_{ani}. According to previous introduction, anisotropy field is composed of several kinds of anisotropy, among which, magnetocrystalline anisotropy is determined by the crystalline structure of ferromagnetic materials and is the intrinsic property. Shape anisotropy is determined by the geometry of ferromagnetic materials and can be easily introduced. One of the common strategies to improve shape anisotropy is selectively patterning, which is the main strategy adopted in this dissertation. The Py thin film is elongated and patterned as slim rectangle bars to increase aspect ratio. As demonstrated before, demagnetization energy along the long axis is weaker than that along the short axis. Thus, by properly patterning Py thin film, high built-in shape anisotropy is introduced, and the total anisotropy field of Py thin film is improved so that the FMR frequency is increased consequently. According to our preliminary research [56], e-beam (electron-beam) lithography is employed to selectively pattern the Py thin film with the dimensions of 440 nm width and 10 μm length, and the FMR frequency of above 4.5 GHz is achieved. To obtain higher FMR frequency, larger aspect ratio is required to increase shape anisotropy field. E-beam lithography technique is optimized and the width of Py pattern is reduced to 150 nm with the same length, and the FMR frequency is improved to 6.3 GHz [57].

The method utilized to deposit Py thin film is DC magnetron sputtering, which is performed with Lesker CMS 18 system. Py thin film is deposited at room temperature in a 2.1 mT Argon (Ar) gas atmosphere. The substrate is rotated at 20 rpm and Py is sputtered by the accelerated Ar^+ ions and the deposition rate is controlled to be 0.023 nm/s. During the deposition, no extra magnetic field is provided. To increase the adhesion between Py and substrate, Chromium or Titanium of $5-10$ nm thick thin film is deposited first with e-beam evaporation system as adhesion layer.

2.3 Py Enabled Electrically Tunable Transmission Line

As demonstrated before, Py has large relative permeability and the permeability can be tuned by applying magnetic field. The large and tunable permeability widely enables Py in tunable microwave applications [34, 35, 58–63]. Among all the tunable applications, tunable transmission line is the fundamental element to construct other tunable microwave components. This section introduces the mechanism, properties, and implementation of Py enabled tunable coplanar waveguide (CPW) transmission line.

2.3.1 Orientation Analysis of Patterned Py Thin Film

Py thin film has large relative permeability. When Py thin film is integrated with transmission line, the inductance density (L) of transmission line can be significantly improved. However, the domain structure of Py thin film must be well-controlled to introduce good permeability performance. According to [64] and [65], possible domain patterns of ferromagnetic slim bars are either 180° domain or multi-domain structures, depending on the balance of anisotropy energies. The 180° domain pattern, with the magnetization oriented parallel to the direction of the anisotropy axis without an external magnetic field applied, is suitable for radio frequency application, especially in increasing the inductance density of transmission lines and inductors. Slimmer and

thinner ferromagnetic film wires are more likely to generate 180° domain patterns. In our design, Py is designed and patterned as slim bars with large aspect ratio and thickness of 100 nm or 200 nm to obtain in-plane uniaxial easy axis and the 180° domain.

The patterned Py thin film is integrated with transmission line by depositing the material on top of the signal line, and there are two possible directions to orient Py patterns: parallel and perpendicular. Parallel orientation refers to the long axis of Py patterns is parallel to the signal line, and the perpendicular orientation means the short axis of Py patterns is parallel to the signal line. In the radio frequency (RF) range, the hard axis permeability of Py patterns is higher than that of easy axis, which is perpendicular to the hard axis. It is because the magnetic flux along the hard axis is governed by the rotational magnetization (spin rotation), and more magnetic flux can be effectively generated along the ac coil current, resulting in significant improvement of inductance. Contrarily, along the easy axis, the hysteresis loop shows much bigger area, which means higher coercivity and loss (domain wall movement), resulting in large eddy current loss [66]. For parallel orientation, when an RF signal is provided to the transmission line, the generated electromagnetic field is perpendicular to the easy axis of Permalloy patterns and parallel to the hard axis. The magnetization oscillates with the external field and hard axis permeability is then able to be excited. Therefore, to achieve more inductance enhancement, the orientation of Py patterns is intentionally parallel to the signal line so that hard axis permeability can be excited when RF signal is provided.

To show the difference of inductance density improvement introduced by different orientations of Py thin film patterns, two CPW transmission lines, with Py deposited on top of the signal lines, were fabricated respectively. To reduce the complexity and time of fabrication for quick demonstration, Py thin film is micro−patterned with the dimensions of 20 μm by 5 μm and 5 μm space between Py patterns. The

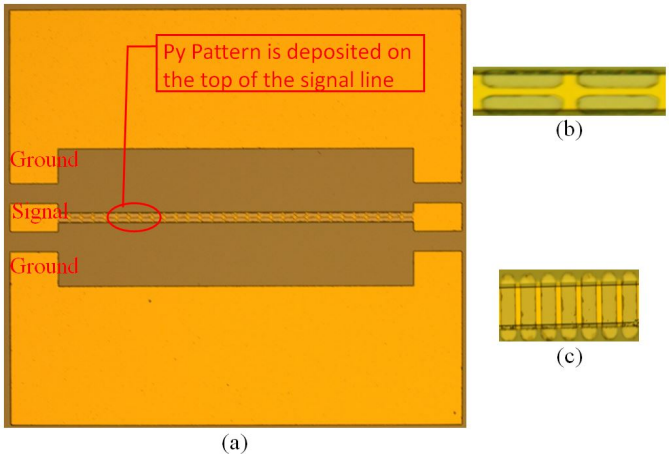

Figure 2.9: Optical photo of (a) fabricated patterned Py enabled tunable transmission line, (b) Py pattern on transmission line 1 with long edge parallel to the signal line and (c) Py pattern on transmission line 2 with long edge perpendicular to the signal line.

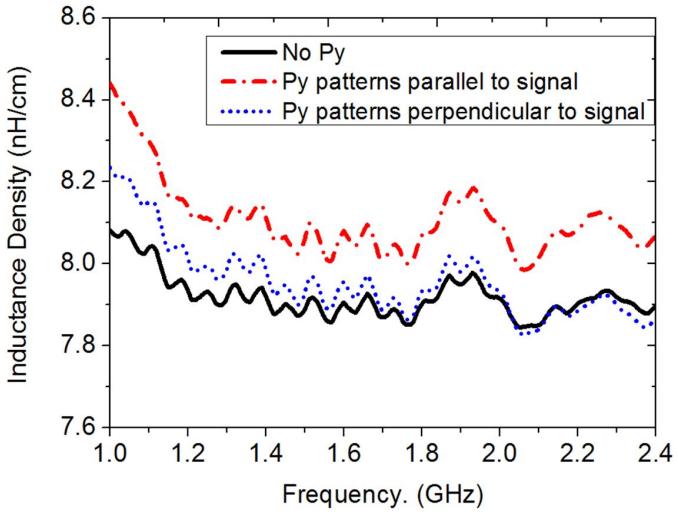

Figure 2.10: Measurement results of inductance density of transmission line without Py, with parallel and with perpendicular orientation of Py patterns, respectively.

thickness of Permalloy thin film is 100 nm. Figure 2.9 shows the optical image of fabricated patterned Py enabled transmission line. Parallel and perpendicular Py patterns are deposited and aligned on top of the two identical CPW transmission lines, respectively.

The inductance densities are extracted from the measured S-parameters with the method proposed in [67]. Figure 2.10 shows the measurement results. It can be seen

clearly from the curves that parallel orientation of Py slim bars has larger inductance density enhancement compared with that of perpendicular orientation. This has clearly confirmed and validated the requirement of adopting parallel oriented Py patterns.

2.3.2 Mechanism and Implementation of Py Enabled Tunable Transmission Line

In addition to the large permeability, the most important feature of Py to achieve tunable microwave applications is that the permeability can be tuned by applying biasing magnetic field. The mechanism of magnetic field tuning the permeability is due to re-alignment of magnetization. When biasing magnetic field is provided along the hard axis of the Py pattern, the magnetization direction is tilted away from its easy axis towards the hard axis, and the equivalent permeability is changed consequently. To qualitatively show the tuning procedure and mechanism, magnetic simulation is conducted with OOMMF. The specimen used in the simulation is a 200 nm thick Py thin film pattern with the dimension of 10 μm length and 1 μm width. In the simulation, standard parameters demonstrated before are used to define the property of Py, and different external magnetic field is provided along the hard axis of Py pattern to bias the specimen.

To obtain the spectrum of susceptibility, starting in an equilibrium state at each point of the Py specimen, a small time-varying external field is applied in addition to the biasing magnetic field to excite the system, which is given as [68, 69]:

$$h(t) = 7.96exp(-7.675t) \tag{2.9}$$

where the unit of $h(t)$ is A/m and t is in ps. The magnetization $M(r_i, t)$ at each point is then a function of time, and is the convolution of the applied field $h(t)$ and

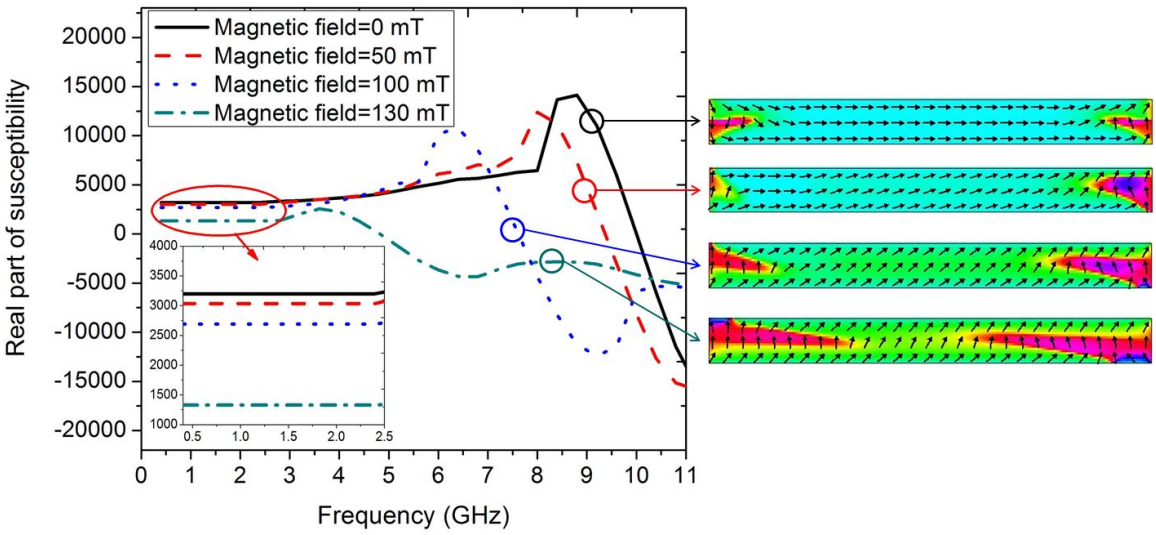

Figure 2.11: Simulation results of real part of Py pattern susceptibility versus frequency under different external biasing magnetic field (left) and correlated magnetization orientation of the Py pattern (right).

the susceptibility $\chi(r_i, t)$:

$$M(r_i, t) = \chi(r_i, t) * h(t) \tag{2.10}$$

$M(r_i, t)$ is summed over r_i and then averaged to obtain the local magnetic spectrum, and the magnetization in the time domain can be expressed as:

$$\overline{M}(r, t) = \sum_i M(r_i, t) / \sum_i i = \overline{\chi}(r, t) * h(t) \tag{2.11}$$

By using fast fourier transform (FFT) technique, the magnetization can be transformed to frequency domain:

$$\overline{M}(r, \omega) = \overline{\chi}(r, \omega) \cdot h(\omega) \tag{2.12}$$

where $h(\omega) = 7.96/(7.675 + 2\pi i\omega)$ and ω is in gigahertz.

Figure 2.11 shows the simulation results regarding to the real part of susceptibility of the Py pattern versus frequency under different external biasing magnetic field and correlated magnetization orientation of the Py pattern. When external magnetic field is applied along the hard axis of Py pattern, the magnetization orientation deviates from its easy axis and turns to hard axis, and consequently the equivalent susceptibility is reduced.

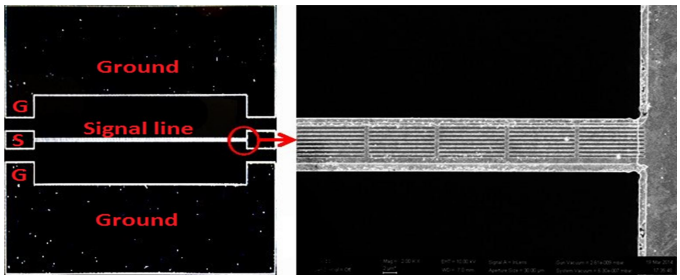

Figure 2.12: SEM photo of fabricated CPW transmission line (left) and Py patterns on top of the signal line (right).

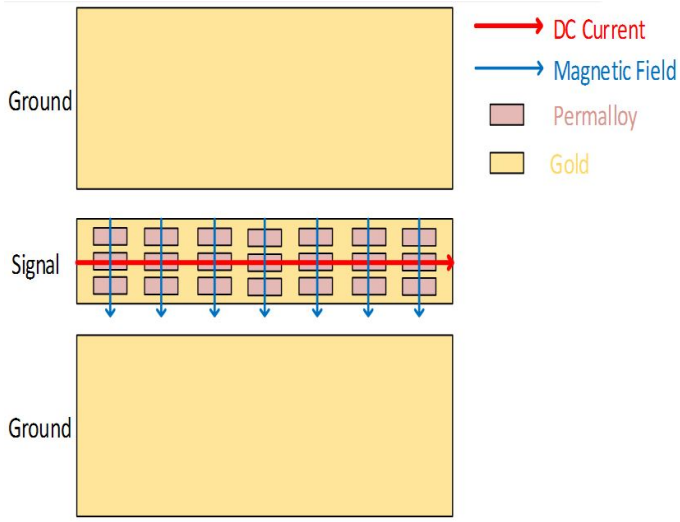

Figure 2.13: Schematic of electrically tuning mechanism utilizing dc current.

The theoretical analysis of tuning mechanism above enables the implementation of tunable microwave components. By integrating Py thin film into coplanar waveguide transmission line, tunable transmission line is designed and fabricated. The device is fabricated on high resistivity (10 k$\Omega-$cm) silicon substrate to reduce the dielectric loss. The metal of CPW transmission line is gold (Au) and is patterned employing photo lithography and liftoff process, with the dimensions of 750 μm lengh and 5 μm width. The thickness of Au is 1 μm. The Py thin film is deposited on top of the signal line. As discussed before, to increase the FMR frequency, Py thin film is patterned as nano-ranged slim rectangle bars utilizing e-beam lithography and liftoff process. The dimensions of Py pattern are 440 nm width and 10 μm length, and the thickness of thin film is 100 nm. Figure 2.12 shows the scanned electron microscope

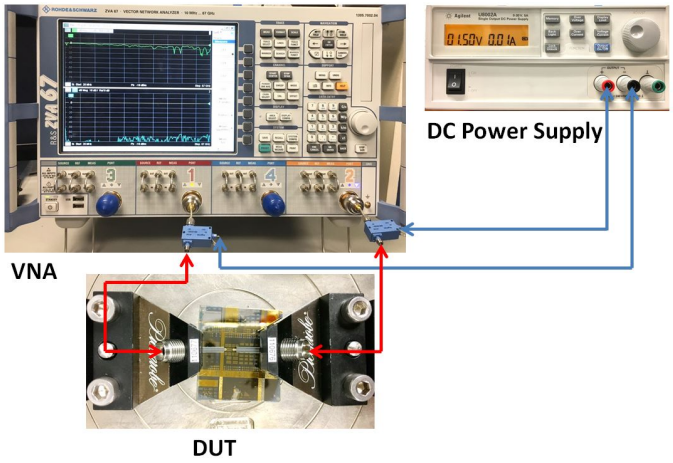

Figure 2.14: Schematic of measurement setup.

(SEM) photo of fabricated tunable CPW transmission line and Py patterns on top of the signal line.

According to the previous demonstration, most conventional tunable implementations utilizing ferromagnetic materials employ external biasing magnetic field to conduct the tuning, which apparently brings integration issues. In this dissertation, instead of the conventional way, a fully electrical tuning method is adopted utilizing dc current [38]. Figure 2.13 illustrates the mechanism of electrically tuning using dc current. When dc current is provided between the two ports of CPW transmission line, the static magnetic field is generated, and on top of the signal line where there are Py patterns, the static magnetic field is parallel to the hard axis of Py patterns so that it is able to rotate the magnetization and tune the permeability.

The measurement of the fabricated tunable transmission is conducted with Rhode & Schwarz ZVA 67 vector network analyzer (VNA) and a power source to provide the dc bias. By utilizing two bias tees, both dc and RF signal can be simultaneously applied to the device under test (DUT). Scattering parameters are extracted under different dc current and inductance density of transmission line is obtained by transformation. Figure 2.14 illustrates the setup of measurement.

The measurement results regarding to the inductance density versus frequency

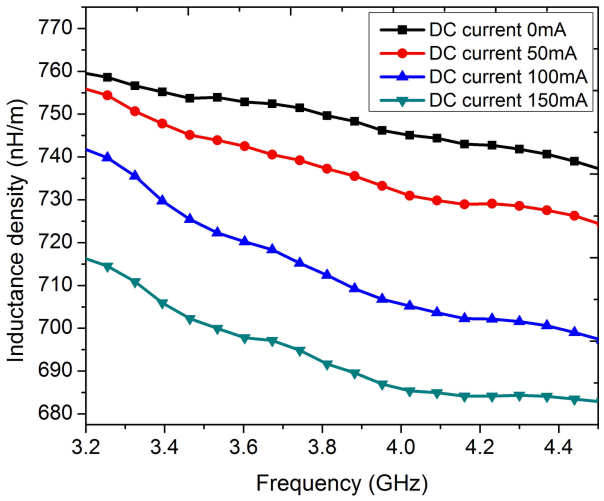

Figure 2.15: Measurement results regarding to the tunable transmission line inductance density versus frequency under different dc current.

Table 2.1: Inductance density of tunable CPW transmission line at 4 GHz.

DC current (mA)	0	50	150	200
Inductance density (nH/m)	746.2	733.3	706.8	687.0

under different dc current are shown in Figure 2.15, and Table 2.1 summarizes the results at 4 GHz. As the dc current is increased from 0 to 200 mA, the inductance density decreases accordingly from 746 nH/m to 687.0 nH/m. The reduction of inductance density of transmission line is due to the permeability decreasing under the static magnetic field generated by applied dc current, which is consistent to the previous theoretical analysis and prediction. The variation of inductance density shown in the measurement results effectively validates the efficacy of Py enabled tunability, and electrically tunable transmission line is realized.

To investigate the tunability effect of signal width, patterned Py thin film enabled CPW transmission lines with different signal line widths are fabricated and measured. The width sequence is 5 μm, 7 μm, 10 μm and 14 μm, and the length is kept to be 750 μm. Figure 2.16 and Table 2.2 shows the measured inductance tunability of CPW transmission lines with various widths.

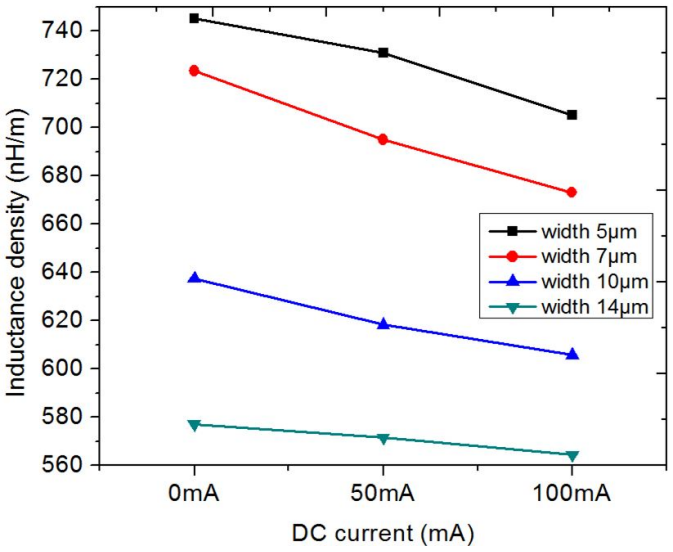

Figure 2.16: Measured inductance density of tunable CPW transmission lines with various widths.

Table 2.2: Inductance density of CPW transmission lines at 4 GHz with different line widths under different dc current.

Inductance density (nH/m)	5 μm	7 μm	10 μm	14 μm
0 mA	745.1	723.5	637.5	577.1
50 mA	731.0	694.9	618.4	571.6
100 mA	705.2	673.1	605.9	564.5

The measurement results clearly show that when the width of transmission line is increased, the inductance tunability drops accordingly. The reason is that the tunability is determined by the magnetic field generated by dc current. The maximum Ampere's field can be estimated per Ampere's law [70]:

$$H = I/2w \tag{2.13}$$

where I is the applied dc current and w is the width of signal line. From the equation, the smaller the signal width of the transmission line is, the larger the Ampere's field is generated for tuning, and more tunability can be acquired. Therefore, to improve the tunability, in addition to increasing the dc current, reducing the width of signal line is another option to generate larger magnetic field for tuning.

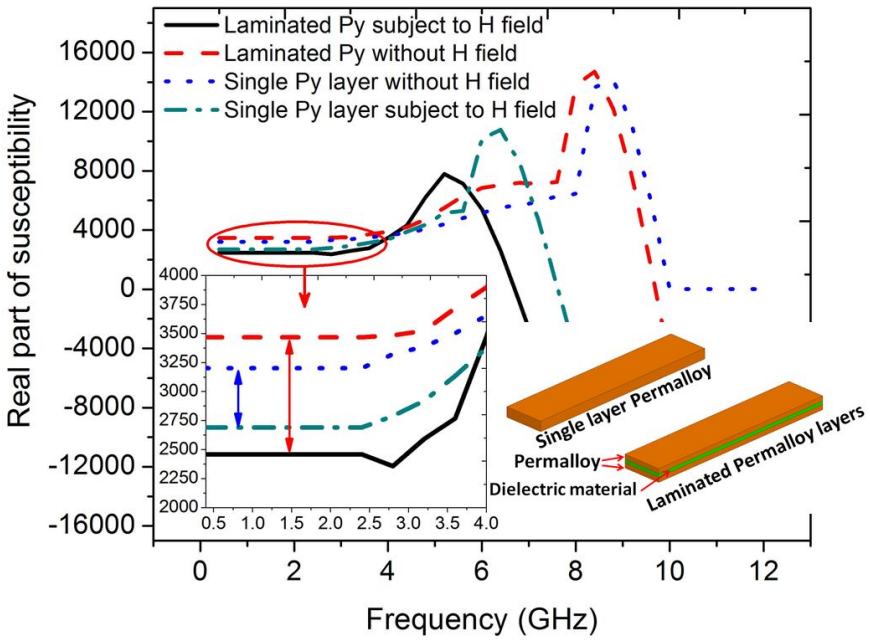

Figure 2.17: Simulated susceptibility of single layer and lamination structure.

2.4 Improvement of Tunability Utilizing Py Lamination Structure

Further improvement of Py enabled inductive tunability can be derived from structural considerations and utilizing different Py thin film configurations. Laminating thinner layers of Py thin films separated by high quality dielectrics can effectively increase the effective permeability and improve the inductive tunability. To prove the concept and validate the efficacy, qualitative magnetic simulation is conducted with OOMMF. The magnetic susceptibility of two Py bars are characterized respectively and compared. One of the bars has single Py thin film layer with the thickness of 200 nm and the other one is composed of two laminated Py layers, with each layer being 100 nm thick, so that the total thickness of ferromagnetic layer of the two bars is identical. The two laminated Py layers are separated by a layer of 50 nm thick dielectric material. The dimensions of the two bars are both 10 μm $\times$ 1 μm. Biasing magnetic field is applied along the short edge of Py bars, which is parallel to the hard axis of the pattern, to tune the susceptibility.

Figure 2.17 shows the simulation results regarding to the real part of magnetic susceptibility of single layer and lamination structure. Apparently, lamination structure shows larger susceptibility than single layer structure without biasing magnetic field. When magnetic field is provided, the susceptibility of both structures is reduced, and lamination structure introduces more susceptibility variation, which indicates larger inductive tunability.

The reason of the improvement in both susceptibility and inductive tunability may be due to the effective elimination of edge domain introduced by utilizing lamination structure [71]. By patterning the Py thin film as a slim bar with large aspect ratio, high built-in shape anisotropy is introduced and the magnetization can be aligned uniformly inside the body of the Py bar. However, for the single layer patterned Py thin film, low-permeability closure domains form at the edges of the pattern (edge domain), which can be observed from the magnetic simulation result of magnetization orientation shown on the right side of Figure 2.11. Since the magnetization of an edge domain is generally aligned along the signal flux direction, the edge domain responds to the excitation primarily by domain wall motion. The movement of domain wall is relatively a slow process, and thus the edge domain does not contribute significantly to high frequency permeability. Lamination structure is an effective method to suppress the formation of edge domain, since the magnetic flux closure occurs between adjacent Py layers through an antiparallel alignment of the magnetization in the adjacent magnetic layers. Further explanation is still under exploration.

2.5 Conclusion

This chapter mainly demonstrates the theory and mechanism of inductive tunability introduced by patterned Py thin film, and proposes the electrically tunable microwave CPW transmission line. The classification of magnetism is introduced first in this chapter, and the properties of diamagnetism, paramagnetism, ferromagnetism,

antiferromagnetism and ferrimagnetism are briefly demonstrated. Among all kinds of magnetism, ferromagnetic materials are most widely used and explored. Some of the fundamentals of ferromagnetism are introduced, including different magnetic energies, domain, hysteresis and FMR frequency. As one of ferromagnetic materials, Py has impressive magnetic properties, and is chosen to implement tunable components in this dissertation. The properties and fabrication of Py are introduced, and the method of selectively patterning Py thin film is utilized to improve the FMR frequency. To obtain good RF permeability performance, different Py pattern orientations are compared and analyzed when Py thin film is integrated with transmission line, and the experiment results indicate better performance of parallel orientation. Afterwards, Py enabled electrically tunable CPW transmission line is proposed and implemented by depositing patterned Py thin film on top of the signal line. The permeability tuning of Py by biasing magnetic field is proved theoretically by magnetic simulation with OOMMF, and the measurement results of tunable microwave transmission line validate the efficacy of Py enabled inductive tunability. The tuning method adopted to change the permeability of Py is dc current instead of the conventional external magnetic field, so that fully electrical tunability is realized, and no integration issue is introduced. The tuning effect of different signal line width is investigated to explore the method of generating larger static magnetic field for larger tunability. The tunability can be increased by utilizing lamination structure, and the efficacy is preliminarily proved by magnetic simulation with OOMMF. The proposed tunable transmission line provides a new topology for designing tunable microwave applications.

Chapter 3

Permalloy Thin Film Enabled Electrically Tunable Inductors

3.1 Introduction

In the previous chapter, Py thin film is patterned and integrated with CPW transmission line, and the inductance density of transmission line is significantly improved. Moreover, due to the tunable permeability of Py subject to magnetic field, the electrically inductive tunability of transmission line is realized. This chapter utilizes the same design topology and integrates the patterned Py thin film into inductors to achieve performance enhanced and electrically tunable inductors.

Inductors are one of the key components and widely used in modern RFIC and MMIC systems [72–75]. With the trend of increasing operating frequencies, high performance inductors are greatly demanded and indispensable in current and future communication systems. However, inductors generally take large chip area and play a limiting role in further reducing the size and cost of communication systems [76]. Electrically tunable inductors are highly capable of solving the technical bottlenecks with decreased complexity and size. Tunable inductors can be widely applied in frequency-agile radios, tunable filters, voltage-controlled oscillators and reconfigurable impedance matching networks.

Ferromagnetic films enabled tunable inductors have been widely explored with the use of single layer or lamination structure of ferromagnetic thin film, and promising results have shown that the inductance density can be greatly improved [56, 77, 78].

Among various types of inductors, the spiral inductor has been established as a standard passive component in high-frequency applications due to its high inductance density and quality factor (Q factor) [79–82].

3.2.1 Design

In our work, a three-turn tunable octagon spiral inductor is designed and fabricated. The line width of the inductor is 20 μm and space between lines is 15 μm. The outer diameter is 890 μm. To reduce the fabrication complexity and demonstrate the concept and mechanism of tunability, only one metal layer is used and one of the two ports of the inductor is configured inside the inductor as shown in Figure 3.1.

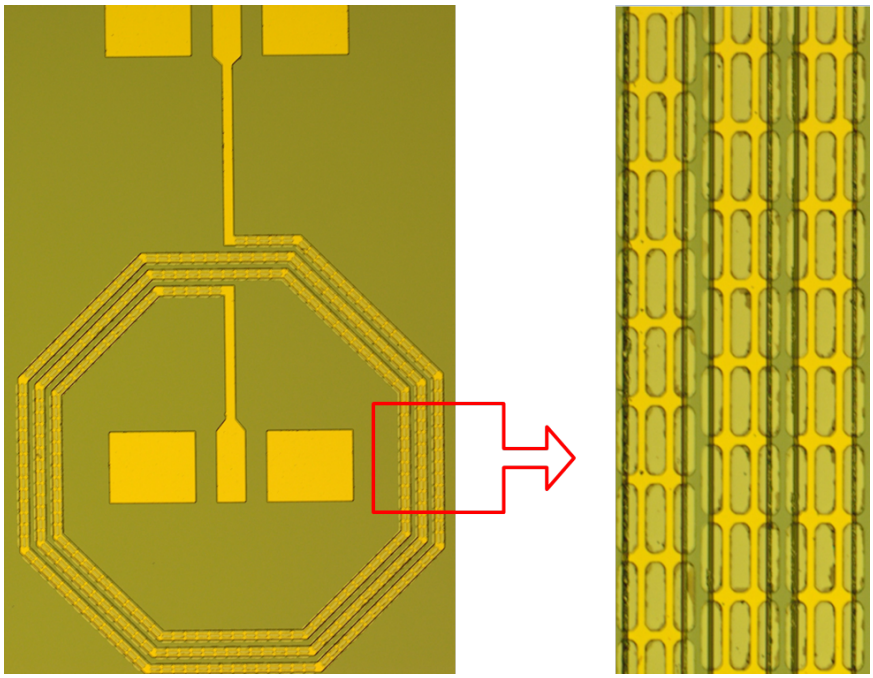

Figure 3.1: Optical photo of tunable octagon spiral inductor (left) and micro-patterned Py thin film (right).

Similar to the configuration of tunable CPW transmission line, Py thin film is deposited on top of the metal wires. Parallel oriented Py patterns are selected

to introduce high permeability along the hard axis, as described in the previous chapter. Since the permeability of the Py film is approximately determined by the ratio of saturation magnetization M_s and anisotropy field H_k [64], while the ferromagnetic resonance (FMR) frequency is proportional to $(M_s H_k)^{1/2}$, there is trade-off between FMR frequency and permeability. Higher permeability can be gained through decreasing the anisotropy field at the cost of the decrement of FMR frequency. In our design, the dimensions of Py thin film pattern are set to 20 μm by 5 μm to properly set the aspect ratio as well as the anisotropy field. The inductance density improvement and tuning range of inductors are proportional to the portion of its magnetic flux path which is filled with magnetic material. Surrounding all four surfaces of inductor wires with high permeability Py yields the largest improvement in both inductance density and tuning range [83]. However, considering the complexity of fabrication, patterned Py thin film is only deposited on top of the inductors wires in our design. Py pattern arrays are well designed so that the width of Py arrays is wider than that of the inductor wires, which can be seen in Figure 3.1. Although the thickness of Py thin film is much smaller than that of gold wires, DC magnetron sputtering is employed to deposit Py, and both sides of gold wires are well covered with Py thin film.

3.2.2 Fabrication and Measurement Setup

The inductor was fabricated depositing 1 μm thick gold on high resistivity (10 kΩ-cm) silicon substrate. Optical lithography and liftoff process were adopted to pattern the gold and Py thin film. Tunable inductors with 100 nm and 200 nm thick Py thin film were fabricated respectively, to compare the inductance enhancement and tunability.

According to the demonstration of previous chapter, dc current can be applied to conduct the tuning of the permeability of Py. Therefore, scattered parameters (S parameters) were measured under different dc current biasing conditions with Rhode

& Schwarz ZVA 67 Vector Network Analyzer and GSG RF probes. DC current and RF signal were simultaneously applied through bias tees between the input and output ports of the inductor. Figure 3.2 shows the DUT (device under test) on the probe station and the measurement configuration.

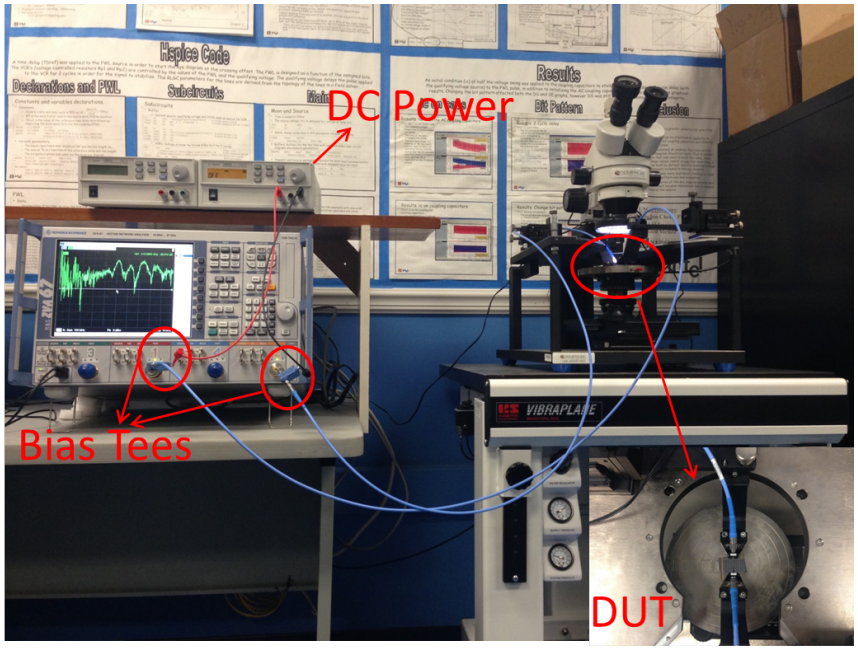

Figure 3.2: Measurement setup and the DUT on probe station (DC current and RF signal are provided simultaneously between input and output ports of tunable inductors).

The quality of the tunable inductor is denoted by inductance and quality factor (Q factor). From the measured S parameters, admittance parameters (Y parameters) can be obtained by transformation and the inductance and Q factor can be defined, respectively, as:

$$L = Im(1/Y_{11})/\omega \tag{3.1}$$

$$Q = -Im(Y_{11})/Re(Y_{11}) \tag{3.2}$$

where Y_{11} is reflection Y parameter and ω is radian frequency [84].

On-wafer multiline TRL (Through-Reflect-Line) calibration [85] is performed to deembed the losses from cables, connectors, bias tees, probes and the parasitic effect

from the measurement GSG pads. ANSYS High Frequency Structural Simulator (HFSS) and multi-level optimizations are employed to get better results used for on-wafer calibration.

3.2.3 Measurement Results and Discussions

Measurement results regarding to the inductance, tunability and quality factor of inductors with 100 nm and 200 nm thickness Py thin films are shown in Figure 3.3, Figure 3.4 and Figure 3.5. Table 3.1 and Table 3.2 summarize the data at 2.2 GHz under different dc bias conditions.

Table 3.1: Summary of Inductance at 2.2 GHZ.

Biasing Conditions	No Py (nH)	100 nm Py (nH)	200 nm Py (nH)
DC=0 mA	9.44	14.54	14.83
DC=200 mA	9.44	14.2	14.25

Table 3.2: Summary of Q Factor at 2.2 GHz.

Biasing Conditions	No Py (nH)	100 nm Py (nH)	200 nm Py (nH)
DC=0 mA	2.30	3.62	2.64
DC=200 mA	2.30	3.89	2.93

It can be seen from Figure 3.3 that with the application of 100 nm thickness Py thin film deposited on top of the metal wires, the inductance of inductor is significantly increased. At 2.2 GHz, the inductance is increased from 9.44 nH to 14.54 nH, which is a 54% increment. The increase is due to the high permeability along the hard axis of Py thin film. Measurement results also indicate that the inductance of the Py enabled inductors can be tuned by the applied dc current. When 200 mA dc current is provided between the two ports of the inductor, the inductance is tunable from 14.54 nH to 14.20 nH, which is about 2.4 % tuning range. According to the illustration in Chapter 2, when dc current is applied, the static magnetic field is generated and is parallel to the hard axis of the Py pattern. The equivalent permeability of the Py thin

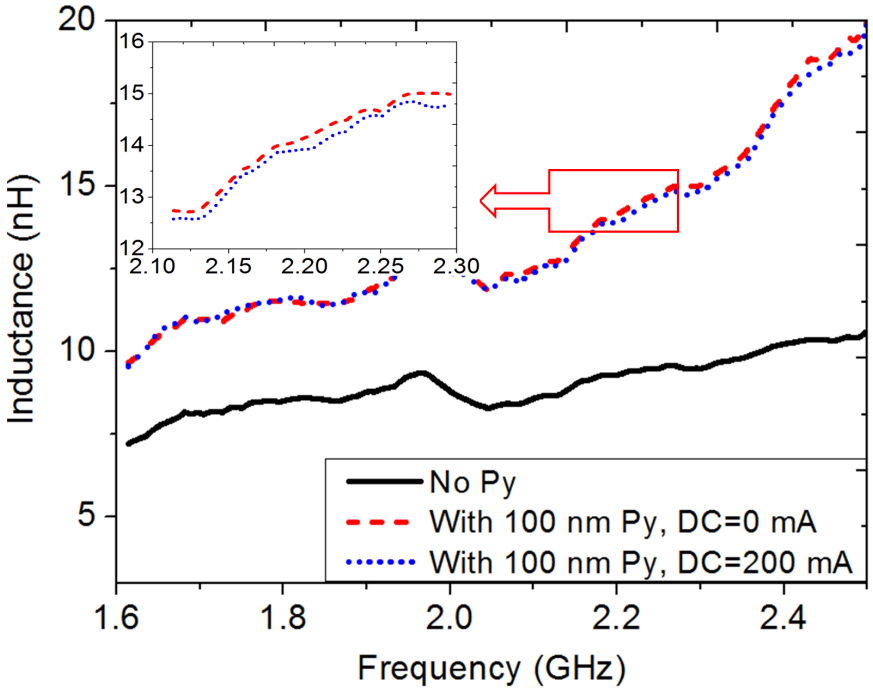

Figure 3.3: Measurement result of inductance with 100 nm Py thin film.

film is tuned and consequently the inductance of the inductor is varied. Applying

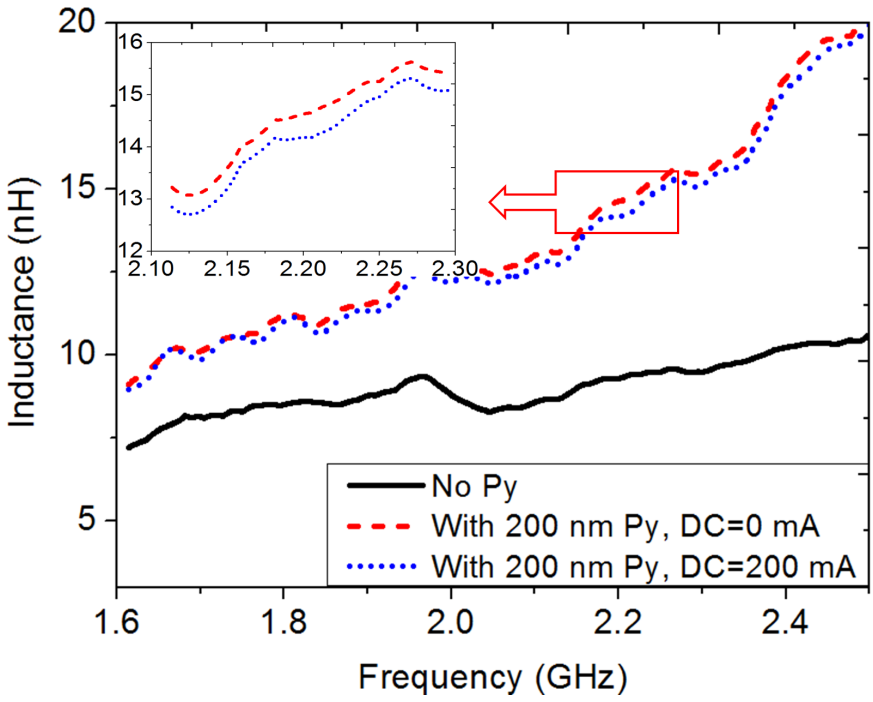

Figure 3.4: Measurement result of inductance with 200 nm Py thin film.

thicker Py film can further increase the inductance density, which can be seen from

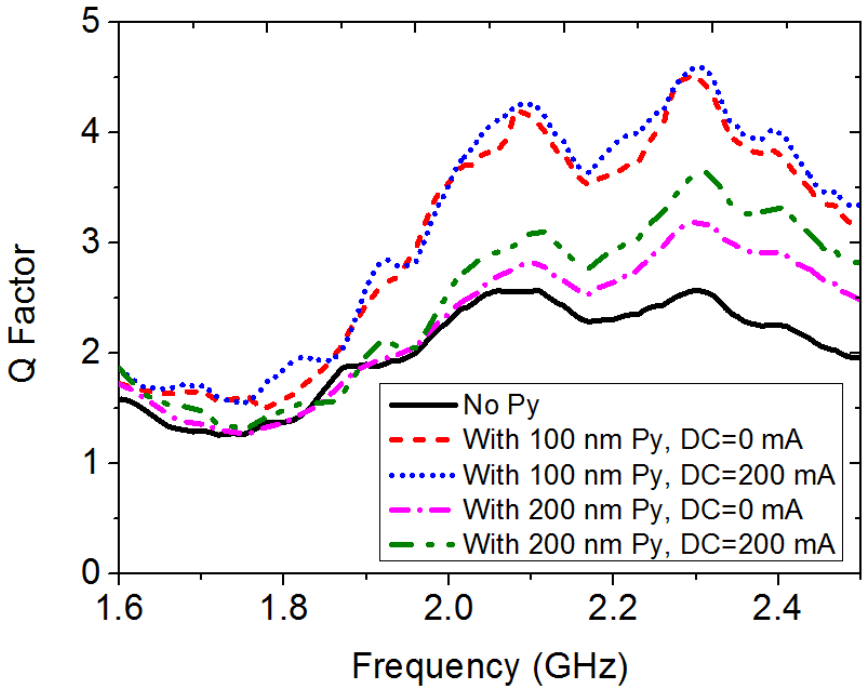

Figure 3.5: Measurement result of Q factor.

Figure 3.4. The inductance is increased 57 % from 9.44 nH to 14.83 nH with the utilization of 200 nm Py thin film. The tunability of inductance is also increased with the thicker film. With 200 mA DC current applied, the inductance is tunable from 14.83 nH to 14.25 nH at 2.2 GHz, which is equivalent to 4.1 % tunability.

From Table 3.1 it can be seen that double thickness (200 nm) of Py thin film only introduces a little absolute inductance enhancement compared with 100 nm Py thin film. The reason is that increasing the inductance of the inductors mainly relies on the improvement of the permeability of Py thin film deposited on the surface of the gold wires of the inductors. However, thicker soft ferromagnetic films does not evidently introduce the increment of absolute value of permeability according to [86], where Cobalt-based soft ferromagnetic is discussed and the theory can be applied to most of the soft ferromagnetic materials. The Newton's method is utilized to compute the intrinsic permeability of soft ferromagnetic materials based on the measurement and the results show that bigger film thickness of soft ferromagnetic

does not introduce larger permeability value. Thicker Py film is utilized mainly because it can bring in more tunability, mostly due to more magnetic moments per volume whose magnetization orientation can be effectively changed under external dc magnetic field.

In Table 3.2, with the 100 nm Py integrated to the inductor, the quality factor is increased from 2.30 to 3.62 compared to that of the regular inductor without Py. The reason is that the Py thin film brings in the enhancement of the inductance [87] and the Q factor is calculated as:

$$Q = 2\pi f \cdot L/R_s \tag{3.3}$$

where f is the working frequency, L is the inductance and R_s is the resistance of the magnetic inductor body, which increases with the operating frequency due to skin effect. The significant inductance enhancement by integrating 100 nm Py thin film is predominant over the extra eddy current loss introduced by Py and the Q factor is improved consequently. When 200 mA DC current is applied, the Q factor further increases from 3.62 to 3.89 even though the inductance value is reduced, which is due to the decrease of effective permeability of the Py thin film, leading, in turn, to lower eddy current loss [34]. On the other hand, when 200 nm Py thin film is integrated in the inductor, the quality factor only increases from 2.30 to 2.64. That is because compared with 100 nm Py thin film, thicker film does not have significantly higher permeability nor introduces much more inductance enhancement. On the contrary, thicker Py film results in more eddy current loss due to smaller resistance. The relatively small quality factor of the entire structure mainly attributes to the small thickness of inductor metal, which is only 1 μm.

Due to the time consuming of DC magnetron sputtering process, only 200 nm thick Py thin film is deposited. Larger inductance tunability can be achieved by further increasing the thickness of integrated Py thin film. However, the thickness needs to be well controlled to guarantee negligible induced eddy current. In Chapter 2, the

performance of Py lamination structure is theoretically discussed and its potential utilization for improving the permeability and inductive tunability is shown through magnetic simulation. By using laminated Py thin films, the inductance of tunable inductor can be significantly improved and simultaneously the inductive tunability can be effectively increased. Another method to increase the tunability is to deposit patterned Py thin film on all the four surfaces and fully surround the inductor wires to form an entire magnetic loop and confine the static magnetic field generated by the dc current. The static magnetic field utilization efficiency thus can be significantly improved to tune the permeability.

3.3 Tunable Solenoid Inductor

The achieved tunable spiral inductor has further validated the efficacy of patterned Py thin film enabled inductive tunability for the microwave applications, and the performance of inductor can be varied by fully electrical method. However, the inductive tunability of the tunable spiral inductor is relatively small, and it mainly attributes to the limitation of planar configuration. When Py thin film is deposited on top of inductor wires, the inductive tunability is dependent on the effective static magnetic field intensity generated by the applied dc current. However, the magnetic field on the top surface of the inductor wires, where there are Py patterns, is not uniform, and only a very small part of magnetic field loop near the Py patterns can be effectively used for tuning, resulting in low tuning efficiency and limited inductive tunability.

Compared with planar spiral inductor, solenoid inductor has the capability of efficiently taking advantage of the magnetic core, and largely confining the magnetic flux to the coils [34, 88, 89]. In this section, a new tunable inductor is proposed and implemented utilizing 3-D solenoid structure with specially designed magnetic core.

3.3.1 Design

The solenoid inductor with 6 turns was designed and fabricated. Figure 3.6(a) and Figure 3.6(b) show the schematic of implemented solenoid inductor and magnified partial view, respectively. To improve the inductance and realize inductive tunability, patterned Py thin film is used to construct the magnetic core of the solenoid inductor. However, due to the high conductivity of Py, it cannot be used directly, and a novel strategy is adopted to design the magnetic core. Two layers of Py thin films were exploited, with a thickness of 100 nm for each layer. The first layer of Py was deposited on top of the gold (Au) wires of bottom solenoid layer, while the second layer was configured beneath the Au wires of top solenoid layer, which is clearly shown in Figure 3.6(b). To separate the top and bottom layers of solenoid winding as well as the two Py thin film layers, a layer of silicon dioxide (SiO_2) is used as insulator. Therefore, the two layers of Py thin films and the SiO_2 insulator form the sandwich-like magnetic core of the solenoid inductor. The dimension of magnetic core is 190 μm $\times$ 170 μm, and the total area of the solenoid inductor is smaller than 0.05 mm^2. To improve the ferromagnetic resonance (FMR) frequency, Py thin film is patterned as long bars with large aspect ratio to introduce the shape anisotropy [90] as discussed before, and Py patterns are 50 μm long and 5 μm wide. According to the demonstration in Chapter 2, in the RF range, the hard axis permeability of Py patterns is higher than that of easy axis, which is perpendicular to the hard axis. Therefore, to achieve more inductance enhancement, the orientation of Py patterns is intentionally parallel to the Au wires so that hard axis permeability can be excited when RF signal is provided.

To analyze inductance improvement and tunability introduced by the integration of Py thin film, a regular solenoid inductor without Py thin film was fabricated for comparison. The regular solenoid inductor has the same dimension as the Py enabled

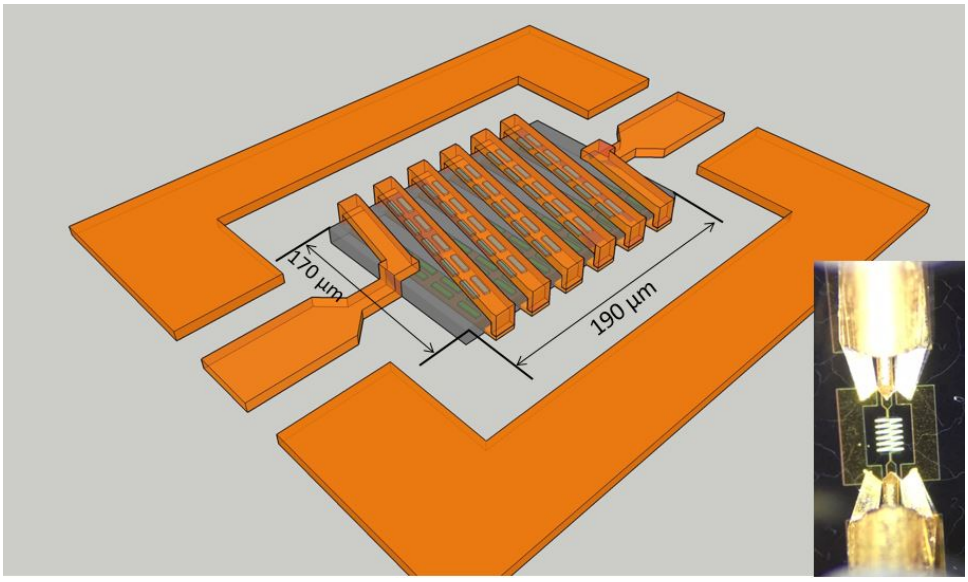

(a)

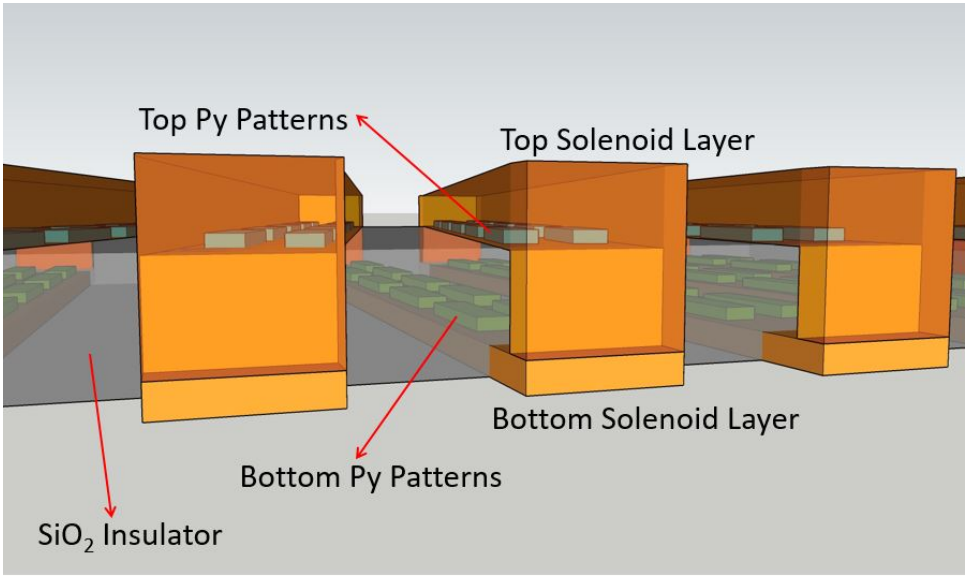

(b)

Figure 3.6: (a) Schematic of 3-D tunable solenoid inductor and (b) magnified partial view.

tunable inductor and utilizes the same SiO_2 as insulator.

3.3.2 Fabrication

The solenoid inductor was fabricated on the high resistivity (10 kΩ·cm) silicon wafer utilizing surface micro-machining techniques. The process is briefly shown in Figure

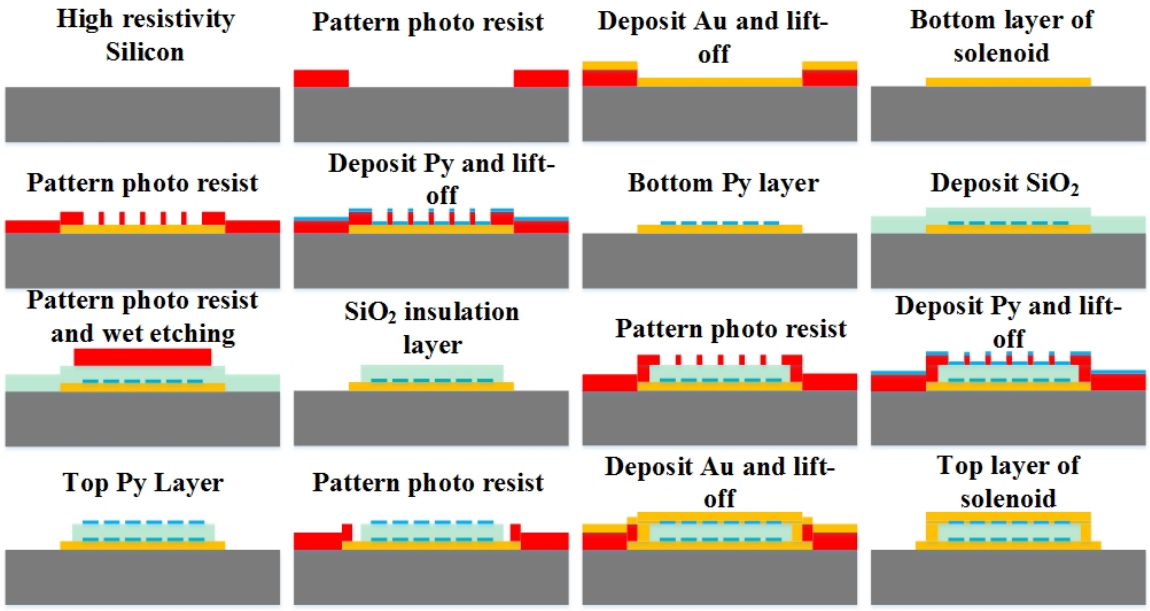

Figure 3.7: Surface micro-machining process of 3-D tunable solenoid inductor.

3.7. The bottom Au layer of solenoid winding was deposited with E-beam Evaporation method and patterned with lift-off process. The thickness of the bottom gold layer was measured to be 300 nm. 100 nm thick Py thin film was then deposited on top of the bottom solenoid Au wires utilizing DC Magnetron Sputtering and was patterned as long bars using lift-off method. Then SiO_2 with a thickness of 800 nm was deposited with Inductively Coupled Plasma Chemical Vapor Deposition (ICP-CVD) and was patterned with wet etching to form the insulator between top and bottom layer of solenoid winding. The dimension of SiO_2 insulation layer was carefully controlled so that the Py patterns were fully covered while the endings of bottom solenoid Au wires were exposed to connect with the solenoid top layer. Before the deposition of top Au layer, another 100 nm thick Py was deposited and patterned with lift-off process. Afterwards, 1 μm thick top Au layer was deposited and lift-off method was used for patterning to form the top layer of solenoid windings.

The thickness settings of Au layers of solenoid winding, Py thin film patterns and SiO_2 insulation layer take the fabrication capability and limitations into consideration. The small thickness of Au solenoid winding, especially the bottom layer of solenoid

winding, whose thickness is only 300 nm, causes deterioration of the quality factor and it will be shown in the next section.

3.3.3 Measurement Results and Discussions

The device properties of the two fabricated solenoid inductors with and without Py thin film were measured, respectively, with the similar test configuration measuring the spiral inductors.

Figure 3.8 and Figure 3.9 show the measured results regarding to the inductance and quality factor versus frequency, respectively, under different dc currents. Table 3.3 summarizes the measurement results at 2 GHz. It is obvious that compared to regular solenoid inductor, Py thin film introduces significant inductance improvement, due to its high permeability. At 2 GHz, the inductance of regular solenoid inductor is 0.93 nH while the Py enabled solenoid inductor shows the inductance of 1.14 nH, which is 22.6% improvement. When different biasing dc currents are provided, the inductance of Py enabled solenoid inductor can be continuously tuned. At 2 GHz, when dc current is increased from 0 mA to 150 mA, the inductance is correspondingly decreased from 1.14 nH to 1.02 nH, which is 10.5% tunability.

Table 3.3: Summary of Measurement Results at 2 GHz.

Biasing Conditions	Inductance (nH)	Q Factor
wo/Py	0.93	0.96
w/Py, DC=0 mA	1.14	0.8
w/Py, DC=50 mA	1.09	0.77
w/Py, DC=100 mA	1.06	0.74
w/Py, DC=150 mA	1.02	0.71

The inductance tunability of Py enabled solenoid inductor is due to the permeability variation of Py thin film under dc biasing condition. When dc current is provided to the solenoid inductor, a static magnetic field with highly uniform intensity and direction is generated, and is confined to the interior of the solenoid. The direction

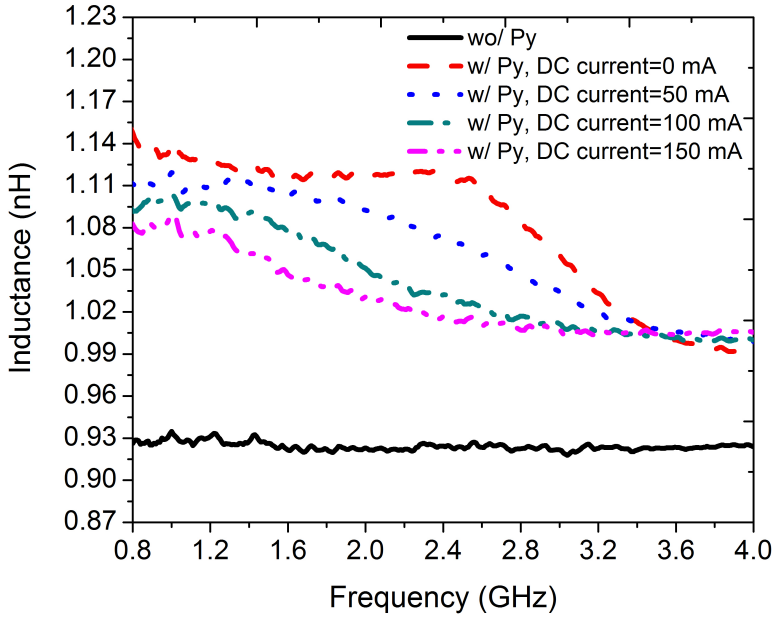

Figure 3.8: Measurement results of inductance at different frequency under different dc current.

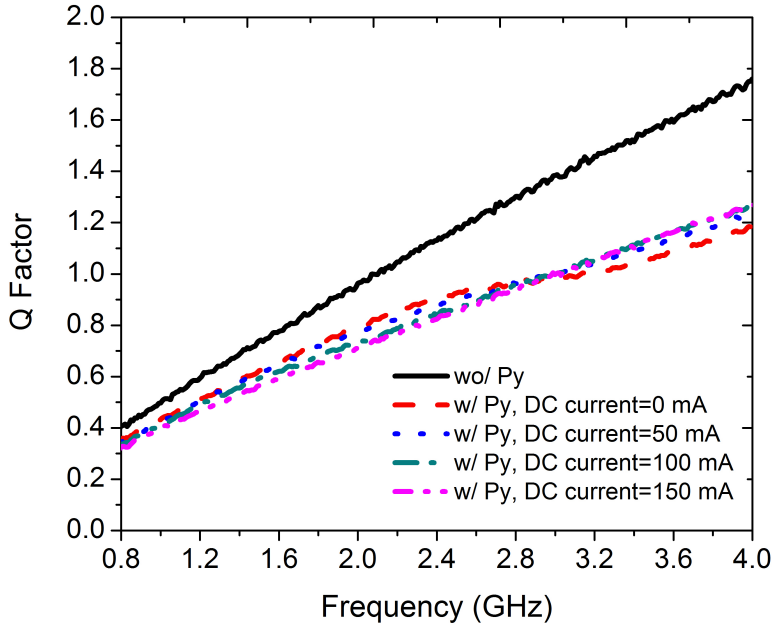

Figure 3.9: Measurement results of Q factor at different frequency under different dc current.

of the static magnetic field is along the long axis of solenoid and is parallel to the hard axis of Py patterns. The static magnetic field causes the rotational movement of magnetization and thus tunes the effective permeability of Py, as is analyzed in the previous chapter.

Compared with conventional solenoid inductors utilizing solid ferromagnetic materials as magnetic core, selectively patterning Py thin film effectively increases the FMR frequency and the working frequency of Py enabled solenoid is significantly improved. It is shown in Figure 3.8 that the operation frequency of tunable solenoid inductor is up to 3.2 GHz with significant inductance enhancement and tunability. The roll-off of inductance mainly attributes to the rapid increasing of eddy current loss inside the Py thin film with respect to the frequency.

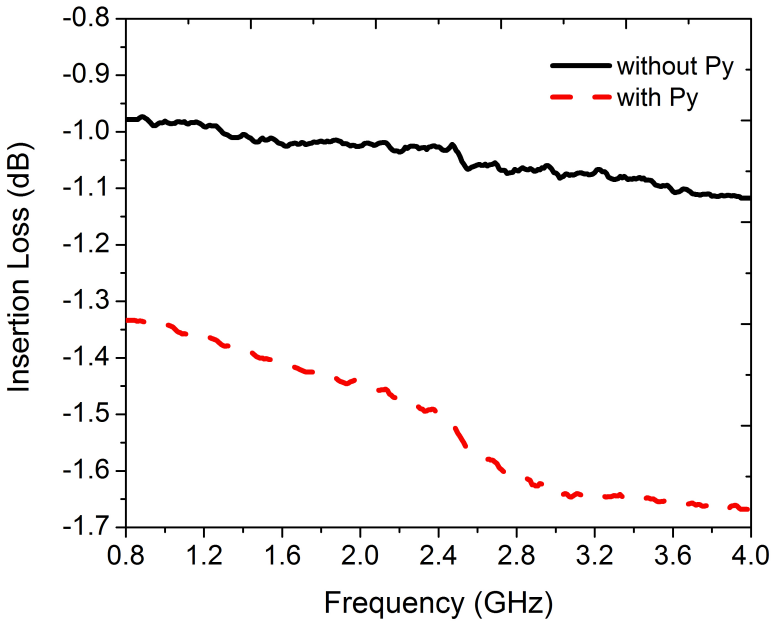

Figure 3.10: Measured results regarding to the insertion loss comparison of solenoid inductor with and without Py thin film.

The quality factor measurement results in Figure 3.9 and Table 3.3 show that integrating Py thin films causes slight quality factor deterioration. Compared with

regular solenoid inductor, Py enabled solenoid inductor reduces the Q factor from 0.96 to 0.8. The extra eddy current loss introduced by Py thin film contributes to the decrease of Q factor. Moreover, as the working frequency is increased, the Q factor difference between regular solenoid inductor and Py enabled solenoid inductor becomes larger, due to more rapid increase of eddy current inside the Py thin film. To evaluate the amount of loss introduced by integrating Py thin film, the measured insertion loss of solenoid inductors with and without Py is depicted in Figure 3.10. It is clearly shown that extra 0.4 dB loss is introduced by Py thin film at 2 GHz. Laminating thinner layers of Py thin films separated with high quality dielectrics can effectively reduce introduced loss due to eddy current. Since the thickness of each Py thin film is greatly reduced, its resistance is significantly increased, resulting in the decrease of induced eddy current and the correspondent loss.

The small Q factor and relatively high insertion loss mainly attribute to the small thickness of Au wires of solenoid winding as mentioned before. To increase the Q factor, fabrication process needs to be optimized such that thicker Au can be deposited.

The Joule heating effect should be considered in case of applying dc current to the solenoid inductor for tuing. When dc current is provided, the temperature of the device is increased due to the existence of dc resistance. The thermal energy can cause such effects as enhanced magnetization rotation, domain reconfiguration and domain wall depinning, and contribute to tilt the magnetization orientation away from easy axis to the hard axis [38], resulting in the variation of permeability. The temperature increment can be estimated by the variation of dc resistance. When dc current is provided from the power supply, the dc voltage between the two ports of the device is measured automatically and the dc resistance can then be obtained by calculation. In the measurement, the maximum dc current of 150 mA and a small current of 1 mA are applied, respectively, and the variation of dc resistance is about

0.5 ohm. The corresponding temperature increment of $\Delta T = 25°C$ can be estimated from:

$$R = R_0[1 + \beta(T - T_0)] \tag{3.4}$$

where R and R_0 are the final dc resistance and initial dc resistance of the device, respectively; T and T_0 are the final temperature and initial temperature of the device, respectively. β is the resistivity temperature coefficient of Au and the value is $3.4 \times 10^{-3}/°C$. The saturation magnetization variation can be estimated from Bloch's $T^{3/2}$ law [91]:

$$M_s(T) = M_s(0)(1 - AT^{3/2}) \tag{3.5}$$

where A is material dependent coefficient. According to the calculation, the decrease of saturation magnetization is less than 1%. Due to the negligible variation of saturation magnetization, the inductive tunability can be mainly attributed to the biasing static magnetic field generated by the applied dc current rather than the thermal effect.

3.4 Couclusoin

Electrically tunable spiral inductor enabled with patterned Py thin film is proposed and implemented. Tunable inductors with different thickness of Py thin films are designed, fabricated and measured. Contributed by the high and electrically tunable permeability of Py thin film, inductance and quality factor of implemented inductors are significantly increased and fully electrical tunability is realized. Over 50% inductance enhancement and over 4% tunability are achieved by integrating Py thin film. In addition to the tunable spiral inductor, utilizing patterned Py thin film and special configuration to form magnetic core, a novel 3-D electrically tunable solenoid inductor is implemented. The fabrication process employing surface micro-machining technique is introduced in detail. Due to the selective patterning of Py enable magnetic core, the working frequency of the solenoid inductor is up

to several GHz. When DC current is provided, the inductance can be varied over 10%. Compared with planar tunable spiral inductor, tuning efficiency of dc bias has been greatly improved due to confined magnetic field inside magnetic core of 3-D solenoids. Much less dc bias is required while the inductive tunability is significantly improved. The implementations of tunable inductors have futher validated the efficacy of utilizing selectively patterned Py thin film for designing electrically tunable microwave components.

Chapter 4

Permalloy Thin Film Enabled Electrically Tunable Bandpass Filter

4.1 Introduction

In the previous chapters, Py enabled electrically inductive tunability is proposed and analyzed, and the efficacy of using this design strategy for tunable microwave components is validated by implementing tunable CPW transmission line and tunable inductors. In this chapter, the design strategy is further explored and tunable CPW transmission line is directly employed to construct a first Py enabled electrically tunable bandpass filter (BPF) prototype.

Tunable bandpass filters are highly needed to support multiple frequency bands with the reduction of system size and complexity in rapidly developing modern wireless communication systems. Reconfigurable and tunable technologies are widely explored and utilized to bandpass filters for replacing classical filter banks so that the system size and complexity can be reduced [6, 29, 92–96].

The proposed tunable BPF works at 4 GHz, and the center frequency can be electrically tuned by dc current without introducing extra devices and biasing field.

4.2 EBG-CPW Cell and Resonator

Electromagnetic bandgap coplanar waveguide (EBG-CPW) structure is adopted in bandpass filter design [97]. EBG structures are functioning to control the electromagnetic wave propagation due to its slow-wave passband and stopband

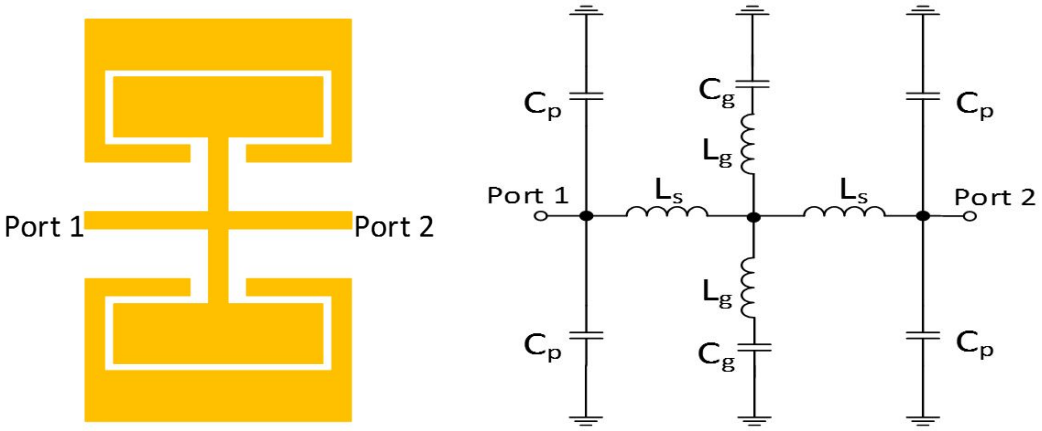

Figure 4.1: Schematic of EBG-CPW cell (left) and equivalent circuit model (right).

characteristics, and are widely used in bandpass filter design to achieve miniaturization and suppression of spurious frequency passbands.

The EBG-CPW cell and its equivalent lumped elements equivalent circuit model are shown in Figure 4.1. Two rectangle patches are in shunt connection with signal line, which is between port 1 and port 2, and is surrounded by ground plane. The signal line is modeled as inductance (L_s) and two shunt capacitance (C_p). The shunt connection line between the signal line and the rectangle patch is modeled as L_g, and the gap capacitance between the rectangle patch and ground is modeled as C_g. The ABCD matrix of the equivalent circuit of the EBG cell is:

$$\begin{vmatrix} A & B \\ C & D \end{vmatrix} = \begin{vmatrix} 1+\frac{Z_1(Z_1+2Z_2+Z_3)}{Z_2Z_3} & Z_1(2+\frac{Z_1}{Z_2}) \\ \frac{(Z_1+Z_3)^2+2Z_2(Z_1+Z_3)}{Z_2Z_3^2} & 1+\frac{Z_1(Z_1+2Z_2+Z_3)}{Z_2Z_3} \end{vmatrix} \tag{4.1}$$

where

$$Z_1 = j\omega L_s \tag{4.2}$$

$$Z_2 = j\omega\frac{L_g}{2} + \frac{1}{j\omega 2C_g} \tag{4.3}$$

$$Z_3 = \frac{1}{j\omega 2C_g} \tag{4.4}$$

According to the ABCD matrix, S_{21} can be determined by:

$$S_{21} = \frac{2}{A + B/Z_0 + CZ_0 + D} \tag{4.5}$$

The phase angle θ_{21} is:

$$\theta_{21} = arctan(\frac{Im(S_{21})}{Re(S_{21})}) \tag{4.6}$$

Based on EBG-CPW cell, the EBG-CPW resonator is constructed by adding two pairs of inductively coupled shunt short stubs to the two sides. Figure 4.2 shows the EBG-CPW resonator and its lumped elements equivalent circuit. The short-circuited CPW shunt stub can be represented by the inductance T-network, and indicated by L_1 and L_2 in the equivalent circuit [98, 99]. The utilization of EBG-CPW structure

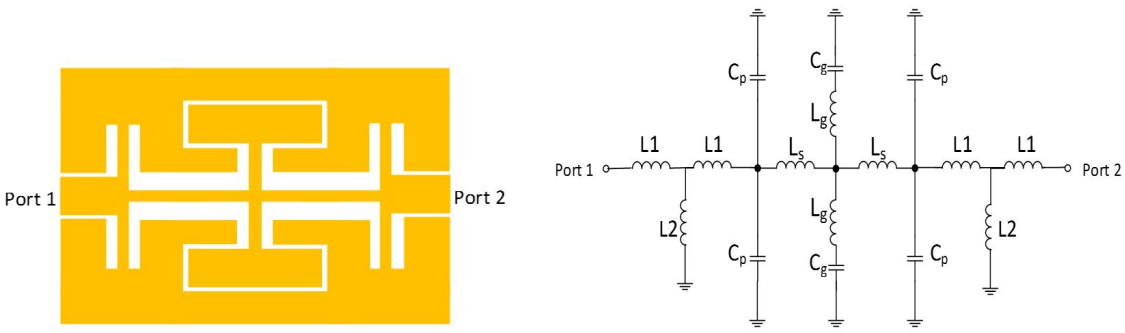

Figure 4.2: EBG-CPW resonator and equivalent circuit model.

for designing bandpass filter is based on several considerations. First, compared with conventional direct coupling CPW bandpass filter [100], EBG-CPW is more compact, the size of which is reduced by more than 50% due to the smaller length of EBG-CPW resonator than the conventional half-wavelength resonator. This is because EBG-CPW structure can provide more effective equivalent capacitance and inductance, especially the capacitance C_g from rectangle patches. Second, from the equivalent circuit of EBG cell, the inductance of EBG-CPW resonators is mainly contributed by the signal lines. Therefore, when patterned Py thin film is integrated to the signal line to construct the tunable transmission line as presented in the previous chapters, the equivalent total inductance of the EBG-CPW resonator can be affected maximally so that larger center frequency tunability can be acquired. Third, different from the normal capacitive coupling BPFs, the adopted EBG-CPW structure provides a direct path for dc current from the input port to the output port

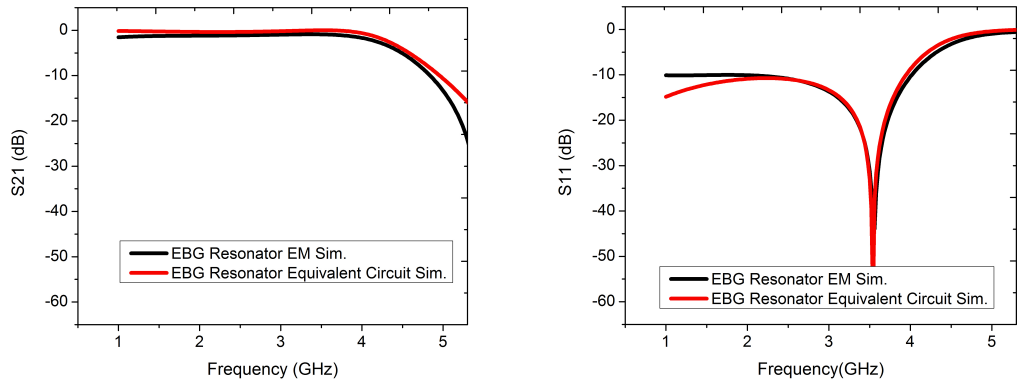

Figure 4.3: Simulation results of EBG-CPW cell and equivalent circuit model.

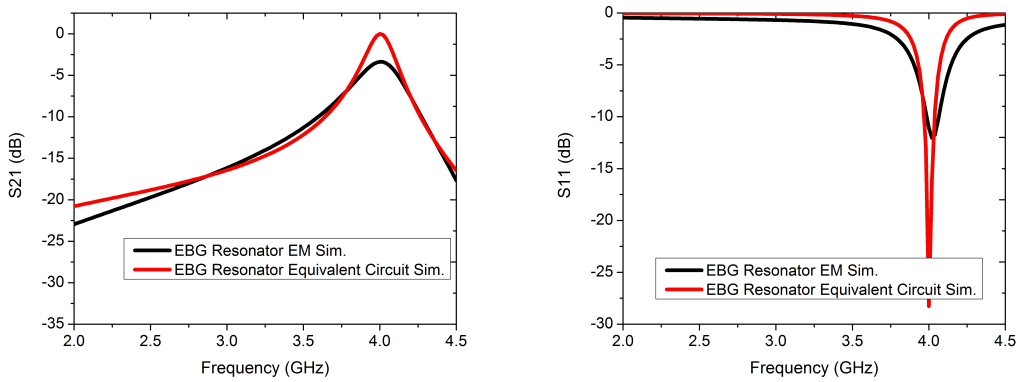

Figure 4.4: Simulation results of EBG-CPW resonator and equivalent circuit model.

to tune the permeability of Py thin film when it is deposited on top of the signal line. Fourth, the resonant frequency of EBG-CPW resonator can be adjusted easily by changing the structural dimensions, especially the dimension of patches. Thus the resonant frequency adjustment is easier and the design procedure is significantly simplified. Fifth, EBG structure is intrinsically transparent to electromagnetic (EM) wave with certain wavelengths while it prevents the propagation of EM wave with other wavelengths. Due to this feature of controlling the propagation of EM wave, EBG structures enabled BPFs have the capability of harmonic passband suppression.

The EM simulation of EBG-CPW cell and EBG-CPW resonator, and their lumped elements equivalent circuit simulation, are performed by High Frequency Structural

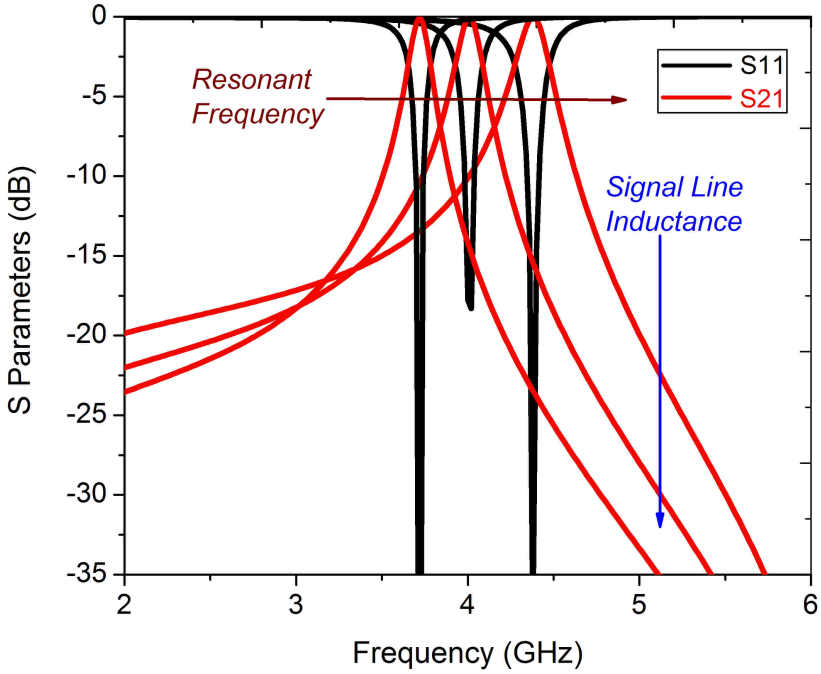

Figure 4.5: Simulation result of resonant frequency of EBG-CPW resonator versus signal line inductance.

Simulator (HFSS) and Advanced Design System (ADS), respectively. Figure 4.3 shows the simulation results of EBG-CPW cell. It can be seen that the EM simulation and equivalent lumped elements circuit simulation are consistent and matched with each other. The low-pass feature of EBG-CPW cell can be seen and the propagation of EM wave can be controlled and suppressed when operation frequency is above the cut-off frequency.

Figure 4.4 shows the EM and equivalent circuit simulation results of EBG-CPW resonator. The resonant frequency is at 4 GHz. For EBG-CPW resonator, signal line inductance is dominant, which is represented by L_s in the equivalent lumped elements circuit, and the resonant frequency of the EBG-CPW resonator is highly dependent on it. To show the correlation of the signal line inductance and resonant frequency of the resonator, equivalent circuit simulation is conducted with ADS and Figure 4.5

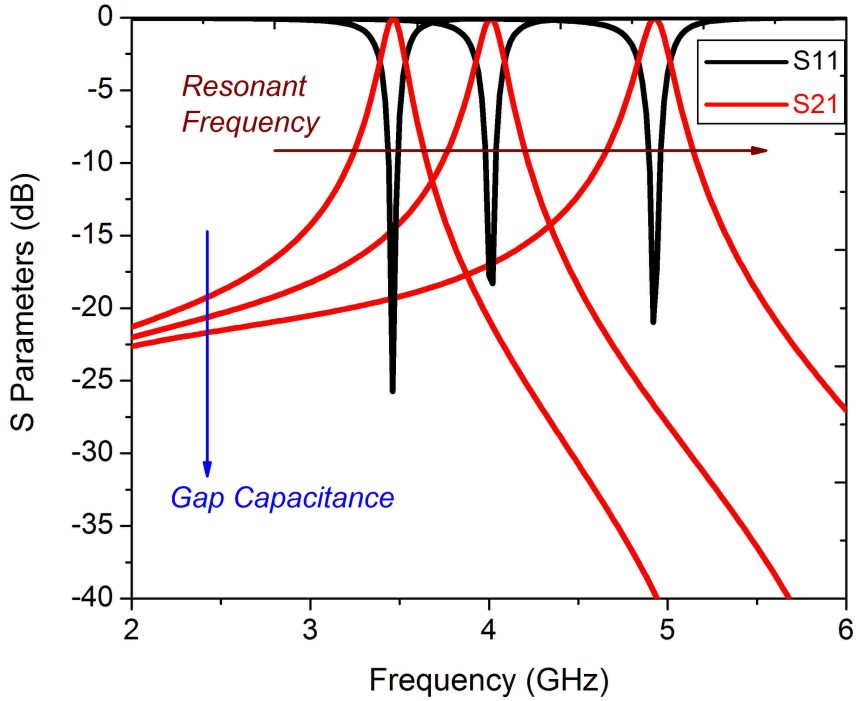

Figure 4.6: Simulation result of resonant frequency of EBG-CPW resonator versus gap capacitance.

shows the simulation result. The resonant frequency of the EBG-CPW resonator is increased to higher frequency with the value of L_s being reduced. The simulation result indicates that the working frequency of the resonator can be easily tuned by changing the signal line inductance.

Another parameter that is able to strongly determine the resonant frequency of EBG-CPW resonator is gap capacitance between rectangle patches and ground, which is represented as C_g in the lumped element equivalent circuit. ADS is employed to conduct the simulation to characterize the resonant frequency versus gap capacitance, and the simulation results are shown in Figure 4.6. From the simulation result it is clearly seen that when the gap capacitance is reduced, the resonant frequency is increased. The method to change the gap capacitance is adjusting either the dimensions of the rectangle patches or the space between the rectangle patches and

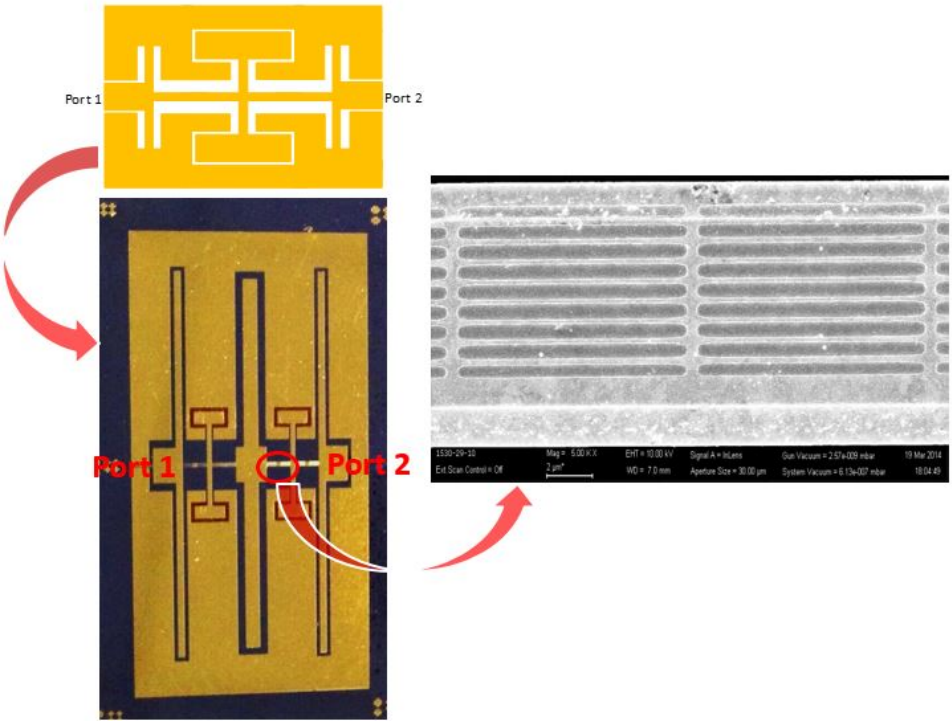

Figure 4.7: Optical photo of tunable BPF composed of two EBG-CPW resonators, and SEM photo of Py pattern.

ground.

4.3 Design of Patterned Py Thin Film Enabled Tunable Bandpass Filter

The bandpass filter is composed of two EBG-CPW resonators, which is shown in Figure 4.7, and is fabricated on high resistivity (10 $k\Omega$-cm) silicon substrate to reduce the dielectric loss. The fabrication process utilizes surface micro-machining technique and is much similar to that utilized to fabricate tunable spiral inductor demonstrated in Chapter 3. Coplanar waveguide transmission line is fabricated with 1 μm Au. The tunability of center frequency can be achieved by tuning the resonant frequency of the EBG-CPW resonator. As is discussed, the signal line inductance can be varied to change the resonant frequency of the resonator, and according to the previous chapters, the inductance density of transmission line can be tuned by integrating

patterned Py thin film. Similarly, to electrically tuned the center frequency of EBG-CPW BPF, Py thin film is utilized and deposited on top of the signal line of each EBG-CPW resonator. The FMR frequency required must be larger than the passband frequency of bandpass filter. To improve the FMR frequency of Py thin film, the same strategy adopted in the previous chapters is employed and Py thin film is selectively nano-patterned as slim bars with e-beam lithography. The length and width of Py patterns are 10 μm and 440 nm, and the thickness of thin film is 100 nm. Figure 4.7 shows the Py pattern. According to [56], the FMR frequency is improved to be above 4.5 GHz.

The tuning method is similar to the previous chapters. DC current is utilized and provided between input and output port of the tunable bandpass filter. Short stubs are replaced by open stubs to provide sole route for dc current so that the dc current can be concentrated to signal line, where Py patterns are deposited, and effectively used for tuning.

4.4 Measurement Results and Discussion

Similar configuration and setup as chapter 3 is utilized for measurement. Standard SOLT (Short-Open-Load-Through) instead of TRL calibration is performed to deembed the losses from cables, connectors, bias tees and RF probes. DC current is applied with the use of bias tees to the input and output ports of the filter for center frequency tuning. Figure 4.8 shows the measurement result regarding to the center frequency tuning of the tunable BPF. The center frequency is 4 GHz originally with no dc current being applied. As the dc current is increased to 400 mA, the center frequency shifts to 4.02 GHz. As is discussed in the previous chapters, when dc current is provided, the static magnetic field is generated, resulting in the reduction of the permeability of Py thin film on the top of the signal line. The signal line inductance is consequently reduced and the center frequency of the BPF is increased.

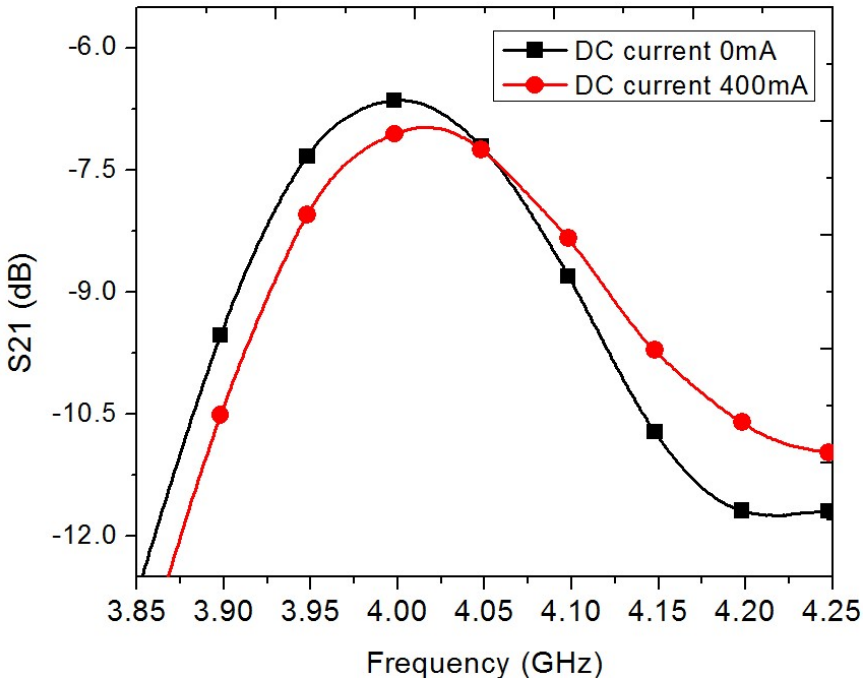

Figure 4.8: Measurement result of tunable BPF under different dc biasing current.

The relatively large insertion loss mainly attributes to the small thickness of Au layer, which is only 1 μm. The impedance mismatch introduced by integrating Py thin film also contributes to the high insertion loss. The proposed tunable BPF is a prototype to demonstrate and validate the efficacy of nano-patterned Py thin film enabled tunable microwave wave applications. Further exploration of design and optimization strategy will be developed to improve the performance and tunability of the tunable BPF.

4.5 Conclusion

Electrically center frequency tunable bandpass filter prototype enabled with selectively nano-patterned Py thin film is proposed and demonstrated, and electrically inductive tunability introduced by Py in the microwave applications is further explored and developed. Design principles of bandpass filter composed of EBG-CPW resonators are analyzed and illustrated. Py thin film is utilized to tune the signal

line inductance of EBG-CPW resonator and the center frequency tunability of the bandpass filter is achieved. The center frequency can be tuned by dc current provided between two ports and no external magnetic biasing field is required. Different tunable range can also be achieved with selective patterning configurations and increased thickness of Py film.

Chapter 5

Electrically Tunable Microwave Components with Dual Tunability

5.1 Introduction

In the previous chapters, Py is successfully applied and integrated to implement tunable microwave components without external biasing magnetic field and extra area being introduced, and electrically inductive tunability is achieved by tuning the permeability of patterned Py thin film with dc current. The design strategy utilizing patterned Py thin film for realizing electrically tunable microwave tunable applications is fully validated.

In this chapter, in addition to employing patterned Py thin film to improve the inductance density and achieve inductive tunability, ferroelectric thin film is introduced and utilized to increase the capacitance density and obtain the capacitive tunability. With the simultaneous integration of ferromagnetic and ferroelectric thin films, electrically dual tunability is achieved. The dual tuning capability not only improves the tuning range and design flexibility, but enables the capability of characteristic impedance retaining.

This chapter firstly demonstrates the properties of ferroelectric materials briefly and introduces Lead Zirconate Titanate (PZT), which is a popular ferroelectric material and utilized in this dissertation to achieve capacitive tunability. The principle of dual tunability and characteristic impedance retaining is then theoretically analyzed. To prove the concept and validate the efficacy of dual

tunability, a tunable transmission line phase shifter with step impedance slow wave structure is proposed and implemented. Afterwords, based on the tunable solenoid inductor proposed in Chapter 3, a 3-D compact tunable phase shifter is implemented. The tunability is significantly improved, and tuning efficiency is greatly increased compared with tunable transmission line phase shifter. Moreover, the electrically dual tunability enabled characteristic impedance retaining capability is clearly shown for the first time.

5.2 Fundamentals of Ferroelectric Materials

Ferroelectric materials are a subset of piezoelectric and pyroelectric materials, and are a class of dipolar dielectric materials exhibiting a spontaneous electrical polarization, which can be re-oriented by electrical field in a certain temperature range. The spontaneous polarization is highly dependent on temperature. When the temperature is below a specific phase transition temperature, which is called Curie temperature, T_c, ferroelectric materials exhibit a non-zero spontaneous polarization even when no electric field is applied, and materials are in ferroelectric phase. The appearance of spontaneous polarization is due to the formation of electric dipoles. The crystalline structure of ferroelectric materials exhibits a slight deformation, and the center of positive charge and negative charge does not coincide when the temperature is below T_c, and as a result electric diples are formed. When the temperature is above T_c, spontaneous polarization disappears and ferroelectric materials become paraelectric. Ferroelectrics show a peak in permittivity at T_c, which can be seen in Figure 5.1.

Figure 5.2 illustrates the relationship of polarization and electrical field for normal dielectric materials, ferroelecric phase and paraelectric phase of ferroelectric materials. In normal dielectric materials, the electrical polarization display linear dependence on the applied electric field, as is shown in 5.2 (a). The resultant permittivity, which can be determined by the slope of the polarization versus electric field (PE) curve, is

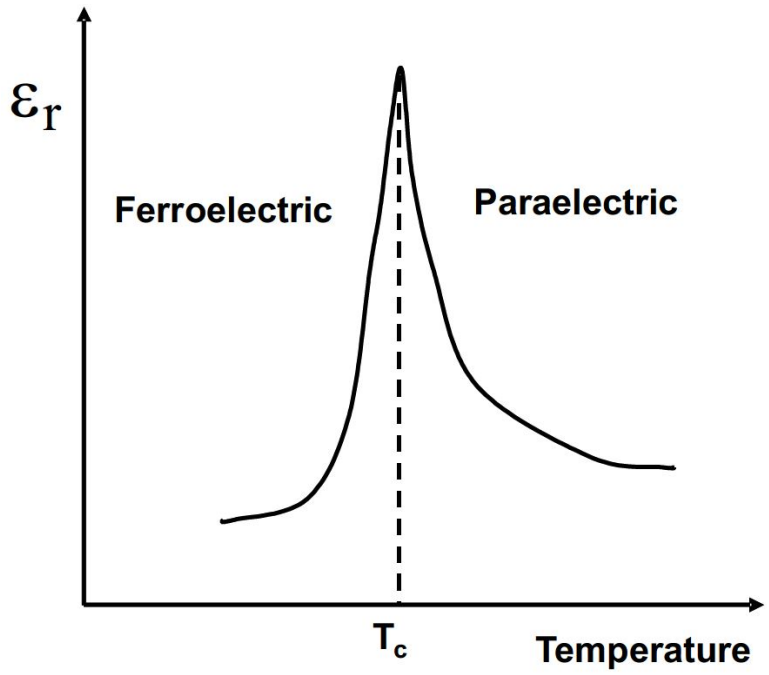

Figure 5.1: Permittivity versus temperature and phase transition of ferroelectrics [101].

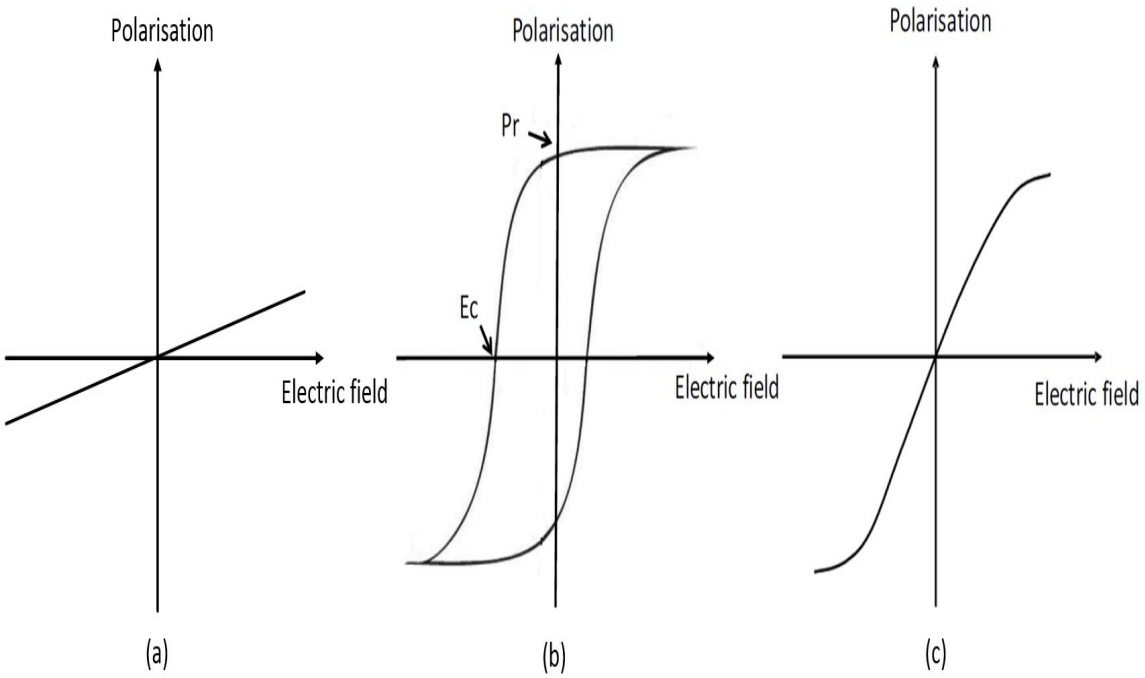

Figure 5.2: Polarization versus electrical field for (a) normal dielectrics, (b) ferroelectric phase when T<T_c and (c) paraelectric phase when T>T_c [101].

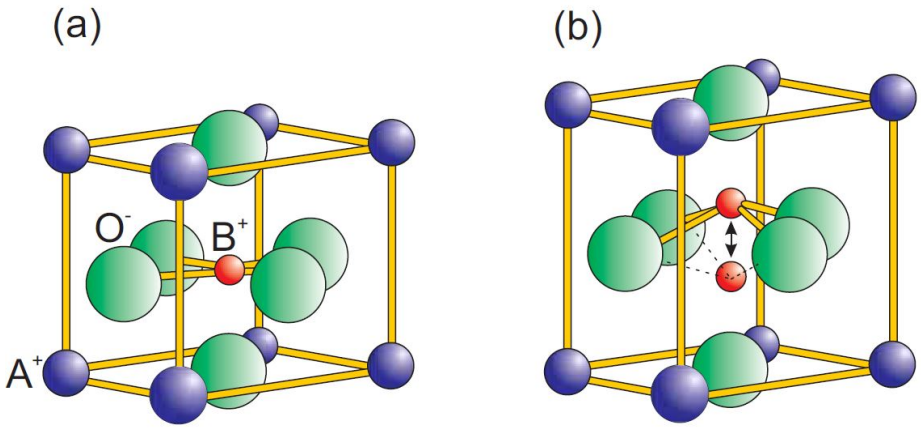

Figure 5.3: Perovskite crystal with (a) symmetrical structure exhibiting no spontaneous polarization and (b) unsymmetrical structure showing spontaneous polarization [103].

a constant. However, for ferroelectric materials under Curie Temperature T_c and in the ferroelectric phase, the polarization does not disappear when the external field is zero, and exhibits a remanent polarization P_r. A coercive field E_c is required to bring the polarization back to zero, and a PE hysteresis loop is observed and is shown in Figure 5.2 (b). When the temperature is above T_c the ferroelectric materials are in paraelectric phase and the polarization is a non-linear function of applied electric field, which can be seen in Figure 5.2 (c), resulting in nonlinear permittivity. It is notable that most ferroelectric materials are used in their paraelectric phase above T_C for microwave applications [102], because in the paraelectric phase, lower loss tangent can be obtained compared with ferroelectric phase, mainly due to the absence of domain walls.

Most of the useful ferroelectric materials have perovskite crystalline structure, which is characterized and represented by the chemical formula ABO_3, and is illustrated in Figure 5.3. B^{4+}-ion is located in the center of crystalline and is positively charged. Six O^{2-}-ions are around the B-ion and are negatively charged. The corners of the crystalline unit cell are occupied by eight positively charged A^{2+}-ions. If the perovskite crystal is in symmetric state (Figure 5.3), no spontaneous polarization is

exhibited. The material becomes ferroelectric when the crystalline lattice loses its symmetry, which is demonstrated in Figure 5.3 (b). In this non-centrosymmetric state, the B-cation has two stable states, and ferroelectric material then can be influenced by an external electric field. When an electric field is applied, both B^{4+} cations and O^{2-} anions shift from their original equilibrium positions and electric dipoles are formed. In the ferroelectric phase when the temperature is below Curie temperature, the ions are subject to a spontaneous displacement in the absence of an electric field and remain permanently displaced, while in the paraelectric phase when the temperature is above Curie temperature, the ions return to their initial equilibrium positions after the electric field is removed [104]. Since the dielectric constant depends on displacement of cations or anions, the ferroelectric materials with perovskite crystal structure have huge dielectric constant, and the dielectric constant can be varied by applying electric field.

Among ferroelectric materials, Lead Zirconate Titanate ($PbZr_xTi_{1-x}O_3$, PZT) is attractive due to its good ferroelectric and mechanical properties and is widely used to implement memories, piezoelectric actuators/sensors, transducers and tunable microwave applications [25, 105–110]. PZT has the perovskite structure with Ti- and Zr-ions occupying B site of primitive ABO_3 cell, Pb-ions replacing A site at the corners, and O-ions being located at the center of faces of the cell. The permittivity of PZT is thus very huge and can be tuned by applying external biasing electric field.

The method used to make PZT precursor in this dissertation is standard sol-gel [90]. 1.731 mL Titanium (IV) Isopropoxide and 1.169 mL Zirconium (IV) Propoxide are mixed first at room temperature, and the well mixed solution is poured into 10 mL 2-Methoxyethanol solvent. The solution is then heated to 90°C and 3.594 g Lead (II) Acetate Trihydrate is added. The prepared PZT precursor is spin-coated to the wafer sample, and finally crystallized at 650°C in oxygen atmosphere for 30 minutes. If PZT is to be deposited on silicon, a 30 nm thick SiO_2 thin layer is

deposited on silicon wafer in advance to improve the adhesion between PZT and silicon. When metal-insulator-metal (MIM) capacitor is constructed, platinum (Pt) can be used as bottom electrode beneath the PZT due to the good stability against high temperature and oxidation, and a 10 nm thick titanium (Ti) is deposited first as adhesion layer between Pt and silicon wafer.

5.3 Principle of Dual Tunability and Characteristic Impedance Retaining

From the basic transmission line theory and high frequency low loss approximation, the general expression for the complex propagation constant is [111]:

$$\gamma \simeq j\omega\sqrt{LC}\sqrt{1-\frac{j}{2}(R/\omega L+G/\omega C)} \tag{5.1}$$

so that

$$\alpha \simeq \frac{1}{2}(R\sqrt{C/L}+G\sqrt{L/C}) = \frac{1}{2}(R/Z_0+GZ_0) \tag{5.2}$$

$$\beta \simeq \omega\sqrt{LC} \tag{5.3}$$

where R, L, G and C are series resistance per unit length, series inductance per unit length, shunt conductance per unit length, and shunt capacitance per unit length, respectively. α and β are attenuation constant and phase constant, respectively. ω is the radian frequency. Z_0 is the characteristic impedance and can be expressed, by the same order approximation, as:

$$Z_0 = \sqrt{(R+j\omega L)(G+j\omega C)} \simeq \sqrt{L/C} \tag{5.4}$$

Accordingly, the phase velocity and electrical length are:

$$v = \omega/\beta = 1/\sqrt{LC} \tag{5.5}$$

$$\theta = \beta l = \omega l\sqrt{LC} \tag{5.6}$$

respectively, where l is the physical length of the transmission line.

By varying L and C with the same ratio, a transmission line with a constant physical length (l) can have a variable electrical length (θ) and a fixed characteristic impedance, which originates the dual tunability and characteristic impedance retaining.

5.4 Electrically Tunable Slow Wave Transmission Line Phase Shifter

The theory is firstly introduced by realizing an electrically tunable slow wave transmission line phase shifter with both inductive and capacitive tunability. Phase shifters are of importance in RF and MMIC applications such as phase array antennas, beam forming networks, power dividers, noise cancelling systems, modulator, frequency converters and other wireless communication systems [112–115]. To meet the requirements of compact size, low cost and low insertion loss across the required bandwidth, frequency-agile electrically tunable phase shifters are highly demanded to solve the technical challenges [33, 116, 117].

In this section, based on the step impedance coplanar waveguide (SI-CPW) slow wave transmission line, both pattered Py and PZT thin films are integrated to achieve an electrically tunable phase shifter with dual tunability.

5.4.1 Design

The SI-CPW slow wave transmission line can be realized by placing alternating narrow and wide conducting sections, which is shown in Figure 5.4(a). The narrow sections can provide higher impedance and inductance density, and the wide sections can introduce lower impedance and larger capacitance density. PZT thin film is grown and patterned between the wide sections and ground, which can be seen from Figure 5.4(b). Due to the high and tunable permittivity of PZT, the capacitance density of transmission line can be improved and capacitive tunability is introduced. Py is

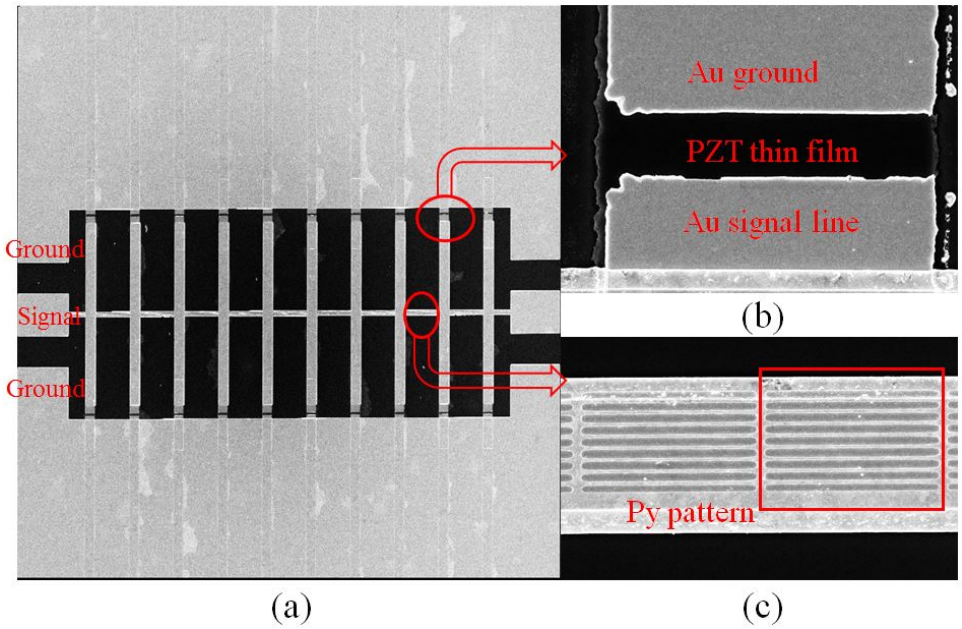

Figure 5.4: SEM photo of (a) fabricated slow wave CPW structure, (b) zoom-in view of PZT thin film between signal line and ground, and (c) patterned Py thin film.

deposited and nano-patterned on top of the narrow conductor sections and Figure 5.4(c) is the SEM photo of Py patterns. Since Py has high and tunable permeability, the inductance density of the transmission line can be significantly enhanced and inductive tunability is brought in. By simultaneously integrating PZT and Py thin films, miniaturization can be achieved and dual tunability is realized.

5.4.2 Fabrication

The tunable phase shifter was fabricated on the high resistivity (10 $k\Omega \cdot cm$) silicon wafer utilizing surface micro-machining techniques. The process is briefly shown in Figure 5.5. A 30 nm thick SiO_2 layer is deposited first on the silicon with Inductively Coupled Plasma Chemical Vapor Deposition (ICP-CVD) to increase the adhesion between PZT and substrate. PZT precursor was prepared with the sol-gel method demonstrated before, and was spin-coated on the substrate. The thickness of PZT thin film was controlled to be 100 nm. Afterwards, PZT thin film was crystallized at 650°C in the oxygen atmosphere for 30 minutes, and wet etching

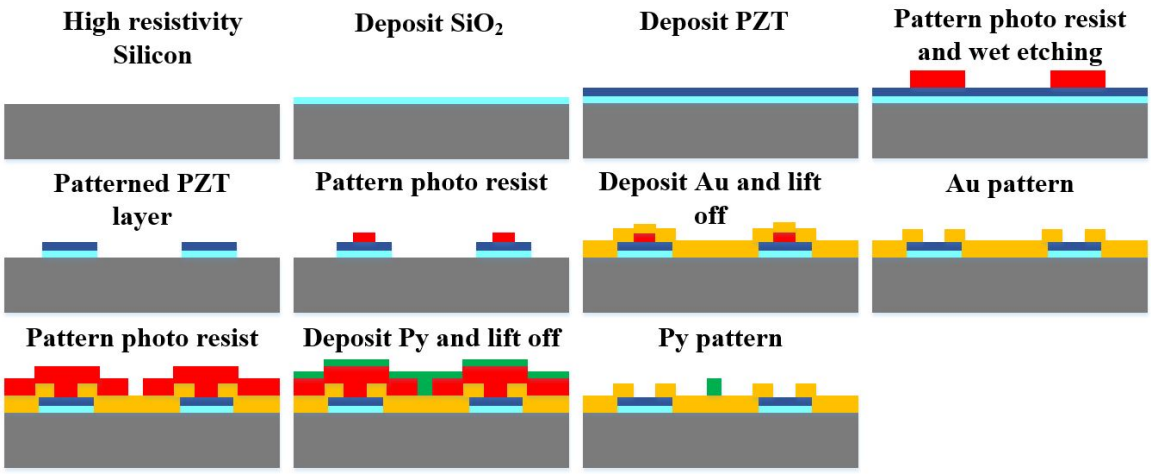

Figure 5.5: Surface micro-machining process of SI-CPW slow wave transmission line.

method was used to pattern the PZT thin film. The utilized etchant is composed of $1BHF : 2HCl : 4NH_4Cl : 4H_2O$ solutions proposed in [118]. BHF represents buffered hydrofluoric acid and functions as a main composition to etch PZT. HCl is used to remove residuals generated on the silicon substrate when PZT is etched. NH_4Cl is used as an additive to decrease the undercutting of the obtained PZT pattern. After completing PZT patterning, 1 μm thick Au was deposited with E-beam Evaporation method and patterned with lift-off process, to form the step impedance signal line and ground. Py thin film was then deposited on top of the signal line by dc magnetron sputtering and was patterned as long bars using e-beam lithography and lift-off method. The thickness of Au layer was limited by fabrication capability. The small thickness of transmission line metal layer causes the deterioration of the quality factor and it will be shown in the next section.

5.4.3 Measurement Results and Discussion

Integrating PZT and Py generates extra loss due to the natural hysteresis feature of ferroelectric and ferromagnetic materials. Moreover, since Py is a kind of good conductor, it additionally introduces loss resulting from eddy current. To demonstrate and compare the loss coming from PZT and Py thin films, insertion loss and Q factor

Table 5.1: Summary of Measurement Results of Transmission Lines at 2 GHz.

Parameters	Only Au	Au with PZT	Au with Py	Au with both PZT and Py
Insertion Loss	1.43	1.49	1.55	1.69
Q Factor	2.70	2.66	2.31	2.15

of a group of different slow wave transmission lines, with the same dimensions as the proposed tunable transmission line, composed of only gold, gold with PZT, gold with Py and gold with both PZT and Py, respectively, are fabricated and measured.

Figure 5.6 shows the measurement results of insertion loss and quality factor, and Table 5.1 summarizes the measurement results at 2 GHz. It can be seen that additional loss is brought in and the quality factor deteriorates as a result of PZT and Py integration. The Q factor deterioration caused by PZT is minor. Compared with the transmission line with only Au, negligible reduction of Q factor by 0.04 at 2 GHz is found for Au transmission line integrating PZT thin film only. The main reason is that the integrated PZT has a thickness of only 100 nm and the film is only deposited to the small area of the 3 μm gap between the low impedance sections and the ground of SI-CPW transmission line. Most of the loss comes from the Py thin film. The Q factor drops by 0.4 at 2 GHz due to the integrated Py. The loss of Py comes from two parts. The first part is its intrinsic hysteresis loss and the other part of loss comes from the eddy current. Since Py has high conductivity, eddy current is generated when RF signal is provided and the eddy current can result in extra conductor loss and deterioration of quality factor.

The transmission line parameters of the SI-CPW slow wave phase shifter can be extracted by utilizing the method proposed in [67]. The complex propagation constant can be denoted as:

$$e^{-\gamma l} = \frac{1 - S_{11}^2 + S_{21}^2}{2S_{21}} \pm K^{-1} \tag{5.7}$$

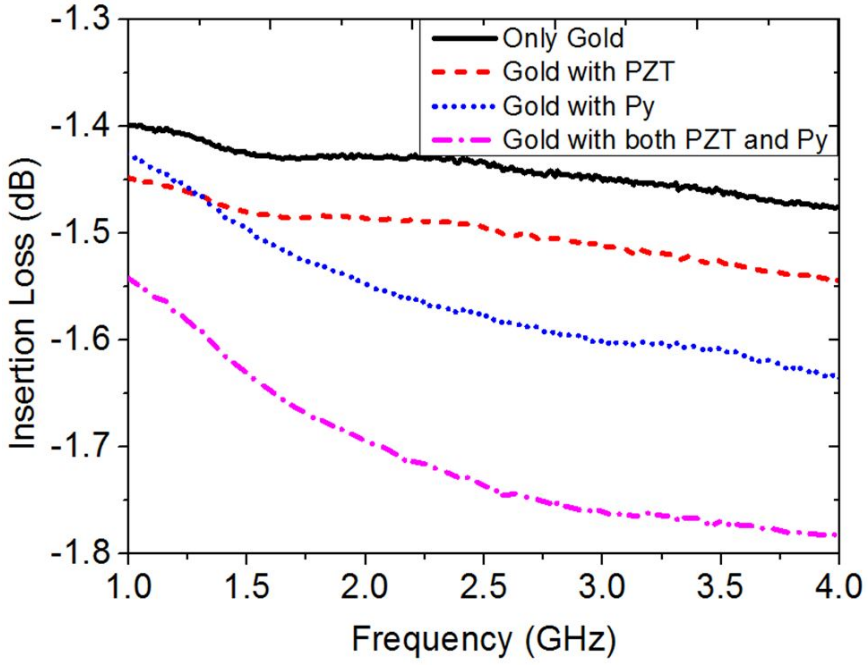

(a)

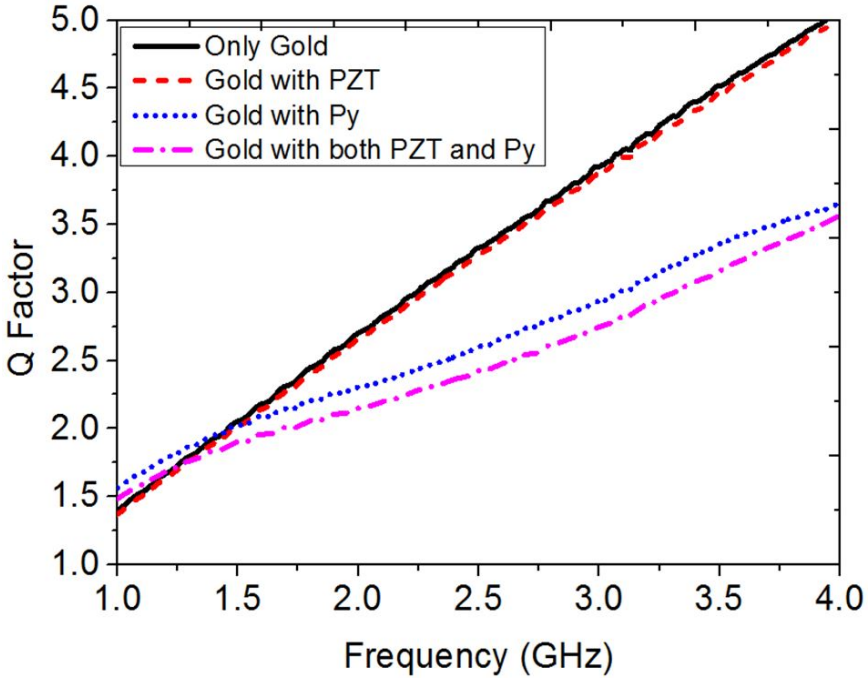

(b)

Figure 5.6: Measurement results of (a) insertion loss and (b) Q factor of the group of transmission lines with different configurations.

where

$$K = \left\{ \frac{(S_{11}^2 - S_{21}^2 + 1)^2 - (2S_{11})^2}{(2S_{21})^2} \right\}^{\frac{1}{2}} \tag{5.8}$$

Table 5.2: Summary of Extracted Measured Transmission Line Parameters.

Structure	dc Voltage (V)	dc Current (mA)	Inductance (nH/cm)@2 GHz	Capacitance (pF/cm)@2 GHz	Characteristic Impedance (Ω)
Regular SI-CPW	0	0	10.7	0.591	42
Thin films enabled SI-CPW	0	0	12.1	0.816	39
Thin films enabled SI-CPW	5	50	11.7	0.764	39
Thin films enabled SI-CPW	15	200	11.2	0.664	40

and l is the physical length of transmission line. The complex characteristic impedance can be calculated by:

$$Z^2 = Z_0^2 \frac{(1+S_{11}^2)^2 - S_{21}^2}{(1-S_{11}^2)^2 - S_{21}^2} \tag{5.9}$$

Once γ and Z are determined, then according to the basic transmission line relationships:

$$\gamma = \sqrt{(R+j\omega L)(G+j\omega C)} = \alpha + j\beta \tag{5.10}$$

$$Z = \sqrt{\frac{(R+j\omega L)}{(G+j\omega C)}} \tag{5.11}$$

Then

$$R = Re(\gamma Z) \tag{5.12}$$

$$L = Im(\gamma Z)/\omega \tag{5.13}$$

and

$$G = Re(\gamma/Z) \tag{5.14}$$

$$C = Im(\gamma/Z)/\omega \tag{5.15}$$

Table 5.2 summarizes the extracted measured L and C results of the implemented SI-CPW slow wave transmission line. Due to the high permittivity and permeability of PZT and Py, respectively, compared with regular step impedance transmission

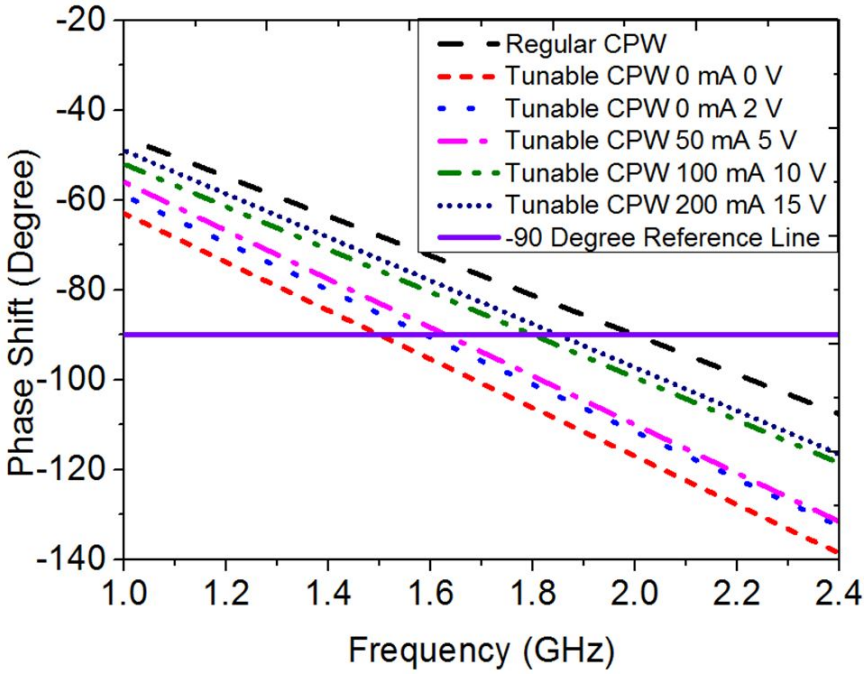

Figure 5.7: Measured phase shift of the implemented regular and thin films enabled SI-CPW slow wave transmission lines, respectively, under different dc biases.

line without PZT and Py, the tunable counterpart integrating both PZT and Py thin films has significant improved the capacitive and inductive density by 36% and 13.3%, respectively. The permittivity of PZT thin film and the permeability of Py thin film are electrically tunable by dc voltage and dc current, respectively. By selective application of dc voltage and current, inductance and capacitance density are electrically tunable while capable of keeping the characteristic impedance the same. The tunable slow wave coplanar waveguide transmission line can be used as tunable phase shifter. The working frequency of the implemented phase shifter for a fixed 90° shifts from 2 GHz to 1.5 GHz compared with regular phase shifter without PZT and Py as shown in Figure 5.7. With the applied dc current and dc voltage, the operating frequency of the phase shifter can be tuned maximally from 1.5 GHz to 1.85 GHz continuously, which is equivalent to 23% electrical tunability.

To describe the figure-of-merit of the tunable phase shifter, degree per unit loss is adopted. From Table 5.1 and Figure 5.7, at 2.0 GHz, the insertion loss of the

Table 5.3: Comparison of Tunable Phase Shifter with State of Art.

Ref.	Phase tunability (°/cm)	Figure of merit (°/dB)	dc bias	Magnetic field bias (oe)	Freq. (GHz)
[33]	36	72	No	100	6.75
[119]	14	N/A	30 V	1700	6
[120]	N/A	20.3	6 kV/cm	200	5.95
[121]	20	40	No	70	6
This work	32	57	200 mA/15 V	No	2

transmission line with only Au is 1.43 dB and the achieved phase shift is 90°, resulting in 62.9° per unit loss. When PZT and Py thin films are integrated, the insertion loss is increased to 1.69 dB and the figure-of-merit is 66.3° per unit loss, based on the 112° phase shift achieved. Integrating Py and PZT thin films effectively increases the electrical length compared to the conventional transmission line with the same physical length due to the enhancement of inductance density and capacitance density, respectively, and more phase shift can be achieved at the same operation frequency. However, since more loss is introduced at the same time, the figure-of-merit of the phase shifter is not increased significantly. When 200 mA dc current and 15 V dc voltage are applied, the change of insertion loss is quite slight while the phase shift is tuned to 96°. The figure-of-merit is consequently decreased to 57° per unit loss.

When dc voltage is applied between signal line and ground, the static electric field is generated, which changes the spontaneous electric polarization and consequently the equivalent permittivity is reduces. Due to the physical limitation of fabrication, the minimum space between wide conductor sections of slow wave transmission line and ground is set to 3 μm, resulting in a large dc voltage required to achieve the designed tunability. Further improvement can be done by utilizing MIM structure to reduce the tuning voltage [105].

Table 5.3 shows comparison on the performance and biasing conditions of the presented phase shifter with state-of-art literature. Similar performance has been

achieved for the presented technology. The proposed phase shifter is fully electrically tunable with simultaneous inductive and capacitive tunability without the application of external biasing magnetic field. In addition, dc current and voltage can be independently applied to tune the working frequency of phase shifter. Although 200 mA has been applied to tune inductance, negligible dc power consumption (∼mW) is added and further reduction of power can be achieved with thicker metal.

5.5 3-D Lumped Element Electrically Tunable Phase Shifter

In the previous section, electrically tunable phase shifter based on SI-CPW slow wave transmission line is implemented, and the methodology of integrating both ferromagnetic and ferroelectric materials for dual tunability has been preliminarily validated. However, since the PZT thin film is deposited in the gap of signal line and ground to construct metal edge capacitor, and limited by the fabrication capability, the dimension of the gap is large (3 μm), resulting in large dc biasing voltage needed for tuning. An effective method to improve the capacitive tunability and reduce the tuning voltage is utilizing metal-insulator-metal (MIM) structure. In Chapter 3, Py enabled electrically tunable solenoid inductor is proposed, and considerable inductive tunability is achieved. In this section, PZT thin film enabled tunable MIM capacitor and Py enabled tunable solenoid inductor are employed, and a lumped element electrically tunable phase shifter is constructed and implemented.

5.5.1 Theory and Design

Figure 5.8 shows the schematic of achieved tunable phase shifter, illustrating the circuit topology composed of lumped inductors and capacitors. Three tunable solenoid inductors demonstrated in Chapter 3 are used to construct the tunable phase shifter and two pairs of PZT enabled tunable MIM capacitors are in shunt connection with the tunable inductors. The lumped-element equivalent circuit of the tunable

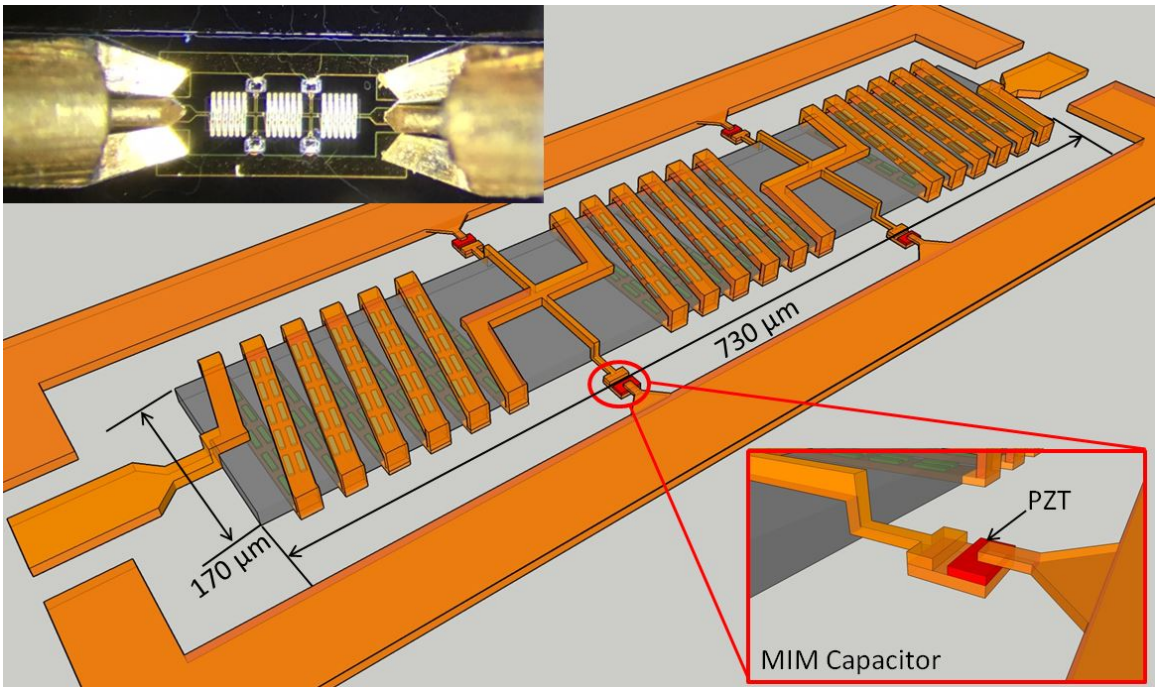

Figure 5.8: Schematic of Py and PZT enabled tunable phase shifter and magnified view of MIM capacitor. The inset on the upper left is the optical photo of fabricated phase shifter under the probes.

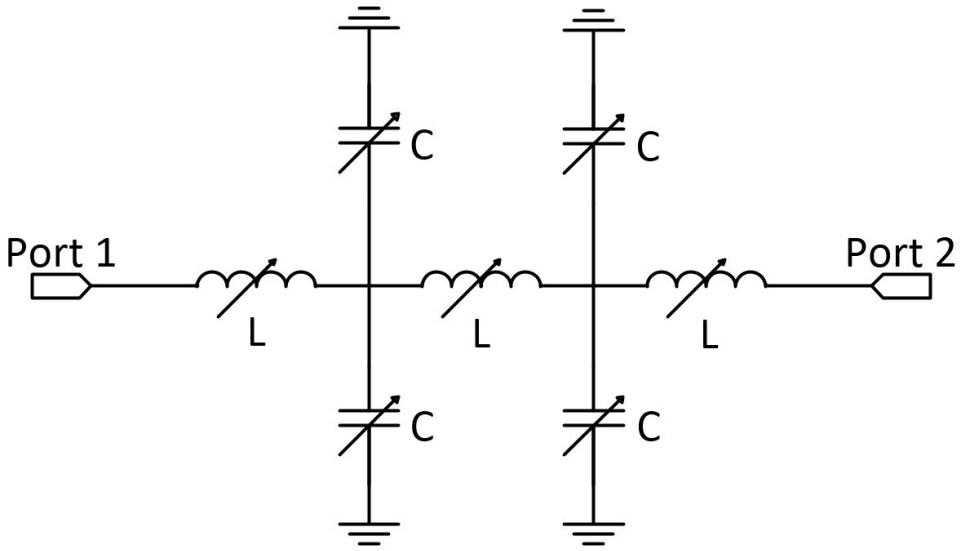

Figure 5.9: Lumped elements equivalent circuit of tunable phase shifter.

phase shifter is shown in Figure 5.9. The ABCD matrix for the lumped-element equivalent circuit, normalized to the characteristic impedance Z_0, can be given

as [122]:

$$\begin{vmatrix} A_0 & B_0 \\ C_0 & D_0 \end{vmatrix} = \begin{vmatrix} 1 & X_L \\ 0 & 1 \end{vmatrix} \begin{vmatrix} 1 & 0 \\ 2Y_C & 1 \end{vmatrix} \begin{vmatrix} 1 & X_L \\ 0 & 1 \end{vmatrix} \begin{vmatrix} 1 & 0 \\ 2Y_C & 1 \end{vmatrix} \begin{vmatrix} 1 & X_L \\ 0 & 1 \end{vmatrix} = \begin{vmatrix} A_1 & B_1 \\ C_1 & A_1 \end{vmatrix} \tag{5.16}$$

where

$$A_1 = 1 + 2X_L Y_C(3 + 2X_L Y_C) \tag{5.17}$$

$$B_1 = X_L(1 + 2X_L Y_C)(3 + 2X_L Y_C) \tag{5.18}$$

$$C_1 = 4Y_C(1 + X_L Y_C) \tag{5.19}$$

and

$$X_L = j\omega L/Z_0 \tag{5.20}$$

$$Y_C = j\omega C Z_0 \tag{5.21}$$

L is the inductance of tunable solenoid inductor. C is the capacitance of tunable MIM capacitor, and can be calculated by:

$$C = \frac{\varepsilon_0 \varepsilon_r A}{d} \tag{5.22}$$

where A is the effective area of MIM capacitor and d is the distance between top and bottom plates, equivalent to the thickness of the PZT thin film. ε_0 is the permittivity of free space and ε_r is the relative permittivity of PZT thin film.

The transmission term S_{21} of S-parameters is calculated as:

$$S_{21} = \frac{2}{A_0 + B_0 + C_0 + D_0} = \frac{2}{2A_1 + B_1 + C_1} \tag{5.23}$$

and the transmission phase is denoted by:

$$\varphi_{21} = tan^{-1}(S_{21}) \tag{5.24}$$

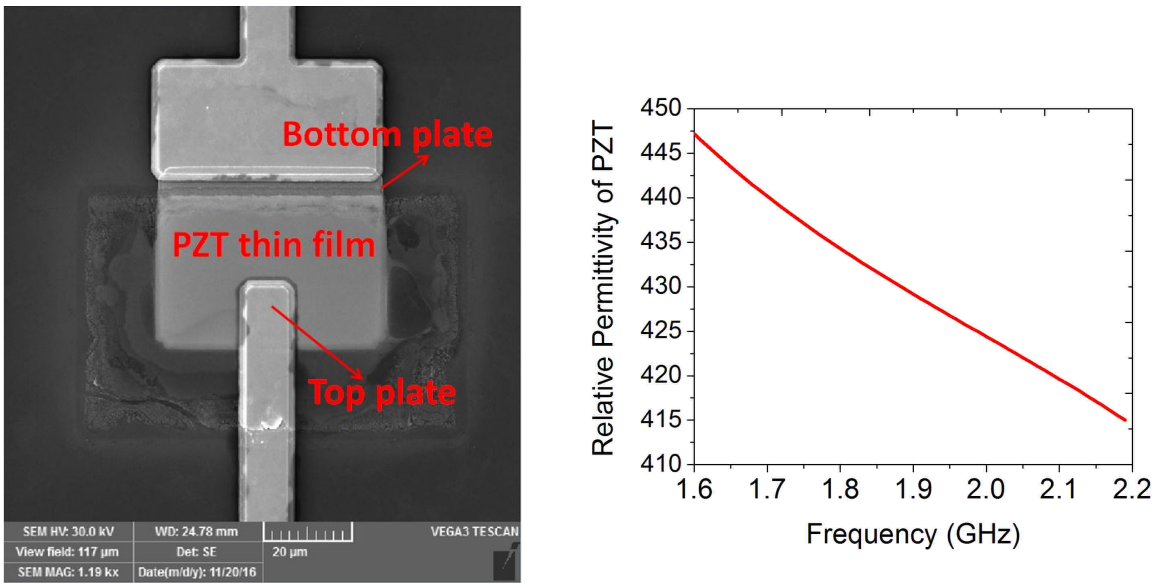

(a) (b)

Figure 5.10: (a) SEM photo of PZT enabled MIM capacitor and (b) extracted relative permittivity of PZT thin film.

The inductance L can be directly obtained from the measurement data shown in Figure 3.9. To obtain the relative permittivity (ε_r) profile of PZT thin film, a standalone PZT enabled MIM capacitor is fabricated and the relative permittivity is extracted from the measurement data by converting S parameters to Y parameters and then calculating the capacitance. Figure 5.10 shows the SEM photo of the fabricated PZT enabled MIM capacitor and the relative permittivity of PZT thin film. The obtained relative permittivity of PZT can be utilized to design tunable MIM capacitor with different dimensions.

The phase of the phase shifter can be varied by tuning the inductors and capacitors. The topology and working principle of Py enabled tunable solenoid inductor have been demonstrated in Chapter 3. For the tunable MIM capacitor design, PZT thin film is used as insulator and is inserted between top and bottom electrodes to form parallel plate capacitor, which can be seen in Figure 5.8. The bottom electrode is connected to ground and top electrode is in connection with the solenoid inductor, and the capacitance is determined by the overlapping area of

top and bottom plates. When the dc voltage is applied between the two electrodes, the induced electrical field can change the permittivity of PZT thin film and the capacitance can be tuned accordingly.

5.5.2 Fabrication

The fabrication process of tunable phase shifter starts from the bottom electrode and PZT thin film of MIM capacitor. The bottom electrode is formed with Pt/Ti bilayer as introduced before, which has been widely used with improved adhesion for PZT film [123]. Pt is selected mainly due to its good stability in high temperature and oxidizing environments, which is crucially required during the crystallization process of PZT. Ti is used to promote adhesion between Pt and substrate. 10 nm thick Ti and 100 nm Pt were first deposited and patterned employing e-beam evaporation and lift-off methods, respectively. PZT precursor was prepared with sol-gel method, which has been demonstrated in the previous section, and was spin-coated on the substrate. The thickness of PZT was controlled to be 200 nm. Afterwards, PZT thin film was crystallized at 650°C in the oxygen atmosphere for 30 minutes, and wet etching method was used to pattern the PZT thin film. After the completion of bottom electrode and PZT thin film, the fabrication of Py enabled solenoid inductor begins and the procedure is shown in Figure 3.7. The top electrode of PZT enabled MIM capacitor was finished together with the top Au layer of solenoid inductor by depositing 1 μm thick Au and patterning with lift-off method.

5.5.3 Results and Discussion

The fabricated tunable phase shifter was measured with similar configuration to test Py enabled tunable solenoid inductor demonstrated before. In addition to a power source to provide dc current for tuning the inductance of solenoid inductor, another

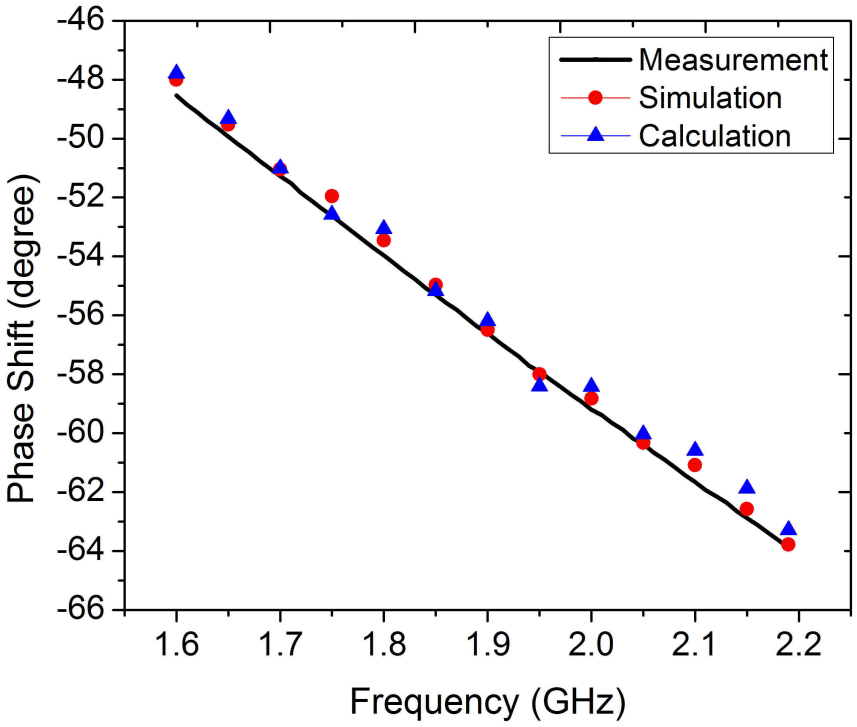

Figure 5.11: Phase shift comparison among measurement, simulation and theoretical calculation without dc bias.

power source was exploited to apply dc voltage for tuning the capacitance of MIM capacitor.

To validate the efficacy of design theory and lumped-element equivalent model of the proposed pahse shifter, simulation is conducted with Agilent ADS software and theoretical calculation is performed with equations (5.16)-(5.24). According to Figure 3.8, the inductance (L) of the tunable solenoid inductor is 1.12 nH. The area (A) of the PZT enabled MIM capacitor is 25 μm^2 (5 μm$\times$5 μm), and the thickness of PZT thin film (d) is 200 nm. The relative permittivity of PZT thin film can be directly obtained from Figure 5.10 (b). The parameters demonstrated above are imported to the simulation and the theoretical calculation, and the results are compared with measurement data. Figure 5.11 shows the comparison between simulation, calculation and measurement results regarding to the phase shift of the device without dc bias,

and a good agreement is reached.

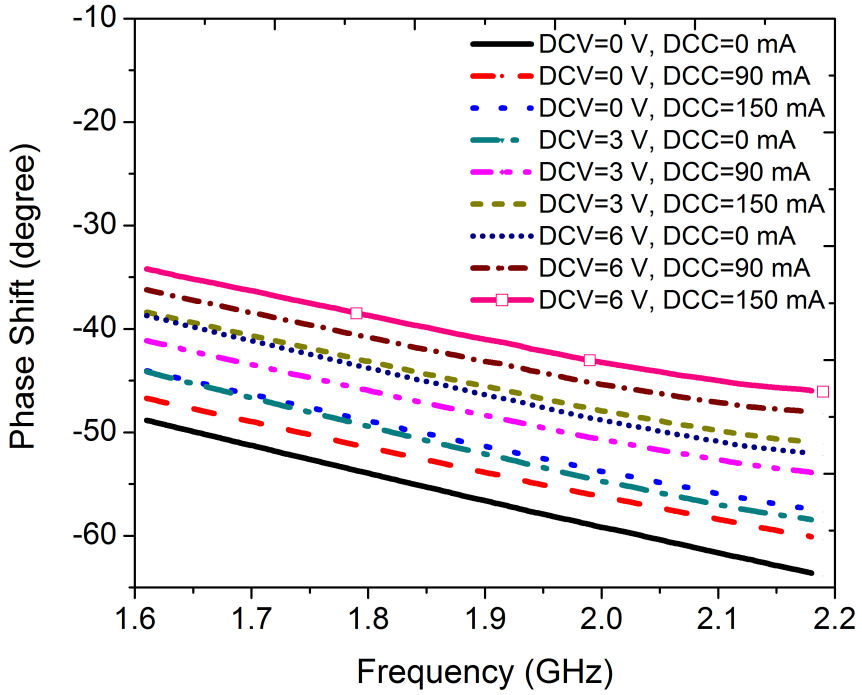

Figure 5.12: Measurement results of phase shift of the device versus frequency under different dc biasing conditions.

Figure 5.12 shows the measurement results regarding to phase shift of fabricated tunable phase shifter at different frequency and dc biasing conditions. Continuous phase variation is achieved by providing different dc biasing conditions. DC current and dc voltage can be applied independently or simultaneously to conduct the tuning. Table 5.4 summarizes the measurement data at 2 GHz with maximum dc current and/or dc voltage. The phase shift of the phase shifter at 2 GHz is 59.2° without any

Table 5.4: Summary of Phase Shift at 2 GHz.

DC Bias (Voltage, Current)	Phase Shift (°)
0 V, 0 mA	59.2
0 V, 150 mA	53.8
6 V, 0 mA	48.8
6 V, 150 mA	43.8

dc bias. When 150 mA dc current is provided between the two ports of the phase shifter, the phase is changed to 53.8°, which is equivalent to 9.1% tunability. The phase variation is caused by the inductance reduction of solenoid inductors when dc current is provided, which is the inductive tunability. The phase of the phase shifter is tuned from 59.2° to 48.8° when dc voltage is applied between the input port and ground, and the tunability is 17.6 %. The applied dc voltage generates electrical field between the two electrodes of MIM capacitors and tunes the permittivity of PZT thin film, resulting in the variation of the phase of the device, which is capacitive tunability. When 150 mA dc current and 6 V dc voltage are simultaneously provided, both inductive and capacitive tunability are achieved and the phase is changed from 59.2° to 43.8°, which is equal to 26.9% tunability. Considering the length of the phase shifter is 730 μm, the length normalized tunability has reached to 210°/cm. The inductive and capacitive tunability enable the phase shifter with dual-tuning capability and significantly improve the tuning range and flexibility. Moreover, the tuning can be performed by fully electrical tuning methods with dc current and dc voltage.

As mentioned before, the dual tunability enables the capacility to retain the characteristic impedance when phase is tuned. According to equation (5.4) and equation (5.6), varying L and C with the same ratio can tune the electrical length of transmission line and keep the characteristic impedance the same. Regarding the tunable phase shifter as an equivalent transmission line, the equivalent characteristic impedance can be extracted from equation 5.9. By carefully providing different dc current and dc voltage biasing combinations, inductors and capacitors of the phase shifter can be tuned with the same ratio to maintain the characteristic impedance while the phase shift is varied. Figure 5.13 shows the measurement results at 2 GHz regarding to the equivalent characteristic impedance and phase shift of the tunable device under different dc biasing combinatinos. By carefully selecting dc current and

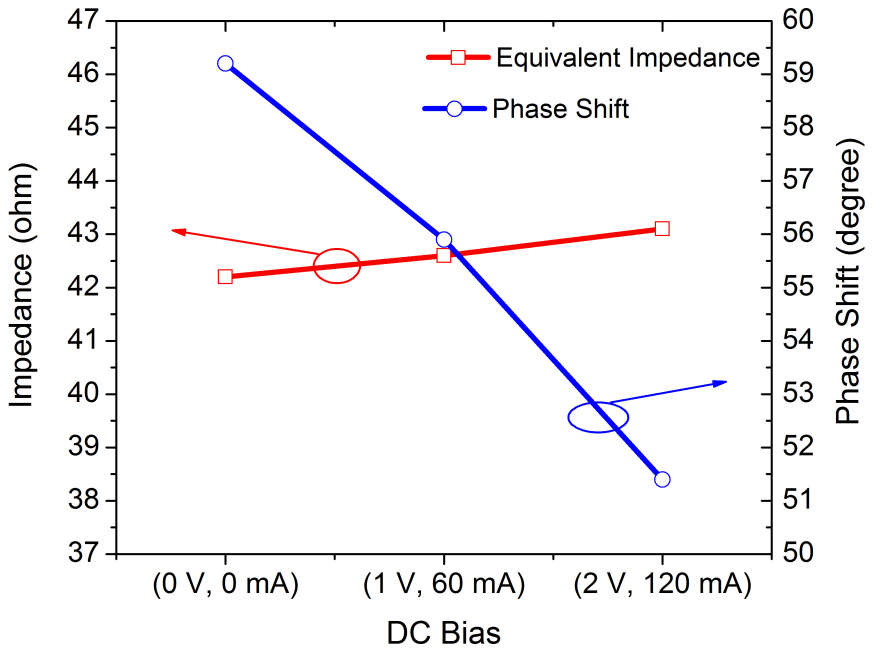

Figure 5.13: Measurement results of equivalent characteristic impedance and phase shift of the device versus frequency under different dc biasing conditions.

dc voltage, the phase is tuned from 59.2° to 51° while the variations of characteristic impedance is within 1 Ω, which effectively proves the concept and validates the efficacy of dual tunability to retain the characteristic impedance.

In addition to the phase shift tunability, the loss of phase shifter is also investigated. Figure 5.14 depicts the measured results of insertion loss and the tunable phase shifter shows around 5 dB loss. According to the measured results of tunable solenoid inductor in Chapter 3, the insertion loss at 2 GHz is about 1.4 dB. Since the tunable phase shifter is composed of 3 inductors, the conclusion can be drawn that the relatively large insertion loss of phase shifter is primarily from the tunable solenoid inductor, which mainly due to the small thickness of Au and integration of Py thin film. The performance of the phase shifter can be denoted by the figure-of-merit (FOM) of degree per unit loss. Considering the phase shift of 59.2° and 5 dB loss at 2 GHz, the calculated FOM is 11.84°/dB.

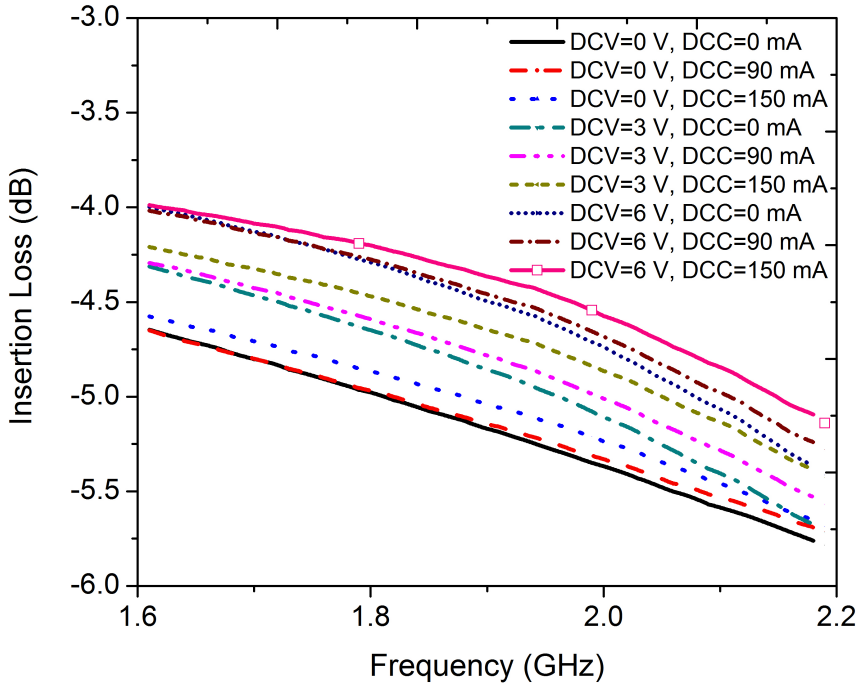

Figure 5.14: Measurement results of insertion loss at different frequency under different dc biasing conditions.

Table 5.5: Comparison of Tunable Phase Shifter.

Ref.	Phase tunability (°/cm)	Figure of merit (°/dB)	dc bias	Magnetic field bias (oe)	Freq. (GHz)
[90]	32	57	200 mA/15 V	No	2
[120]	N/A	20.3	6 kV/cm	200	5.95
[121]	20	40	No	70	6
This work	210	11.84	150 mA/6 V	No	2

Table 5.5 summarizes the length normalized phase tunability, FOM and biasing conditions for tuning of the state-of-art literature. Significantly higher length normalized phase tunability is achieved due to the compact lumped elements structure composed of thin films enabled tunable solenoid inductors and MIM capacitors, and the capability of dual tunability. Tuning of the phase is realized by fully electrical methods with dc current and dc voltage, and no external biasing magnetic field is

required, which avoids the integration issue.

Compared with tunable SI-CPW transmission line phase shifter implemented in the previous section, due to the novel combined utilization of tunable 3-D solenoid inductor and tunable MIM capacitor, the required dc bias is significantly reduced while the tuning efficiency and electrical tunability is greatly improved. The larger dual tunability compared with previous work also noticeably enables the impedance retaining capability.

5.6 Conclusion

Electrical dual tunability is proposed and demonstrated in this chapter. By integrating both patterned Py and PZT thin films into microwave components, inductive and capacitive tunability is realized simultaneously, and smart tunable microwave components are achieved, which can be tuned by dc current and/or dc voltage. With dual tunability, tuning range can be significantly improved and design flexibility can be increased. Moreover, the most important advantage that dual tunability introduces is the characteristic impedance retaining capability, with which the performance of tunable microwave components can be tuned while the impedance can be kept constant. The efficacy of proposed design methodology is effectively validated by implementing two different types of tunable phase shifters. The first tunable phase shifter is based on a planar structure with Py and PZT thin films integrated into SI-CPW transmission line. The tunable phase shifter has both inductive and capacitive tunability, which can be tuned by applying dc current and dc voltage, and promising phase tuning range is achieved. In addition to the planar transmission line phase shifter, based on tunable solenoid inductors and MIM capacitors, a novel 3-D lumped-element tunable phase shifter is proposed and implemented. Compared with the planar counterpart, 3-D structure effectively increases the tuning efficiency, and significantly improves phase tuning

range. Moreover, the 3-D configuration greatly miniaturize the dimension of device due to higher density of inductance and capacitance of solenoid inductor and MIM capacitor, respectively. Due to larger inductive and capacitive tuning range of 3-D tunable phase shifter, impedance retaining is clearly demonstrated. The proposed tunable components and design methodology can be widely exploited to design arbitrary tunable microwave components, such as tunable bandpass and bandstop filters. The dual tunability and characteristic impedance retaining capability is essentially useful in designing LC impedance matching network.

Chapter 6

Summary and Future Work

6.1 Dissertation Summary

Novel design methodology integrating patterned ferromagnetic (Py) and ferroelectric (PZT) thin films for realizing smart tunable microwave applications has been proposed, demonstrated and validated in this dissertation . Tunable microwave components are crucial elements for achieving reconfigurable and frequency-agile radio systems. With the application of proposed design methodology, tunable microwave components can have both inductive and capacitive tunability, and are capable of retaining characteristic impedance. The performance of components can be tuned by utilizing fully electrical methods, such as dc current and dc voltage. No extra external biasing condition is required, which avoids the integration issue, and since Py and PZT thin films are fully integrated with microwave components, no extra area or auxiliary components are introduced.

The first part of the dissertation proposes and validates the topology of Py enabled electrically inductive tunability. Fundamental properties of Py are introduced and by selectively nano-patterning Py thin film as slim bars, FMR frequency has been significantly improved to fit for the utilization in the microwave frequency range. To increase the high frequency permeability, the orientation of Py patterns is discussed due to the difference between easy axis and hard axis permeability in RF frequency range, and parallel orientation is adopted for larger RF permeability. The optimization results of FMR frequency and high frequency permeability of Py thin

film are used to design electrically tunable CPW transmission line. Py thin film is nano-patterned and is deposited on top of the signal of CPW transmission line. When dc current is applied, the generated static magnetic field is parallel to the hard axis of Py patterns, and the permeability of Py thin film is tuned so that the inductance density of transmission line is changed. Compared with conventional tuning method utilizing external biasing magnetic field, employing dc current effectively avoids the integration issue and electrical tunability is achieved.

The implementation of electrically tunable transmission line preliminarily proves the concept of Py enabled electrically inductive tunability. To further validate the efficacy and develop the applications of topology, two tunable inductors and a tunable bandpass filter are designed and fabricated. A planar tunable spiral inductor is proposed first and by integrating patterned Py thin film, inductance is significantly increased by more than 50%, and the inductance can be tuned by maximally 4% when dc current is applied. To improve the tuning efficiency and inductive tunability, a novel 3-D solenoid inductor is designed with specially configured Py enabled magnetic core. Compared with its planar counterpart, the required dc current is reduced while the tunability is greatly improved, which is more than 10%. For the tunable bandpass filter design, EBG structure is adopted and the achieved tunable CPW transmission line is utilized. When dc current is provided between the two ports of BPF, the center frequency can be tuned and shifts to a higher frequency.

The implementations of tunable transmission line, tunable inductors and bandpass filter have fully validated the efficacy of Py enabled electrically inductive tunability. Based on that, the second part of the dissertation demonstrates the novel design methodology by integrating both patterned Py and PZT thin films. Py can introduce inductive tunability and PZT is capable of realizing capacitive tunability. By combining both inductive and capacitive tunability, the concept of dual electrical tunability and resultant impedance retaining capability are introduced, and the

design methodology is proved by implementing two types of tunable phase shifters. The first tunable phase shifter is based on step impedance coplanar waveguide slow wave transmission line structure. Patterned Py thin film is deposited on top of the high impedance sections of signal line and PZT thin film is deposited between low impedance sections of signal line and ground to form metal edge capacitor. When dc current and dc voltage are provided, the working frequency to achieve 90° phase shift can be tuned from 1.5 GHz to 1.85 GHz. Equivalently, at 2 GHz, the phase can be tuned by 30°, and the length normalized phase tunability is 32°/cm. In addition to the planar tunable transmission line phase shifter, based on the achieved Py enabled tunable solenoid inductor and PZT enabled tunable MIM capacitor, a novel compact 3-D lumped-element tunable phase shifter is implemented. Compared with planar phase shifter, the required dc current and dc voltage are greatly reduced while the tunability is improved. Due to the larger tunability and smaller component size, the length normalized phase tunability has reached to 210°/cm. Moreover, the notable tunability has clearly demonstrated the impedance retaining capability for the first time.

6.2 Future Work

6.2.1 Improving the Tuning Efficiency and Tunability

In the dissertation, tunable microwave components with both planar and 3-D structures are implemented and explored. Compared with planar structure, 3-D architecture has achieved significantly larger tuning efficiency and electrical tunability. For example, due to the utilizing of magnetic core, the solenoid inductor effectively confines the static magnetic field inside the core and generates more uniform magnetic field for tuning. Compared with planar spiral inductor, significant tunability improvement has been realized. Another example is PZT enabled tunable

capacitor. In the dissertation, MIM capacitor has larger tunability with much lower applied dc voltage compared to its metal edge counterpart. Other architectures and configurations of tunable microwave components will be further explored and developed trying to maximally utilize the static magnetic field generated by dc current.

In addition to the optimization from the structure of microwave components, another method to improve the tunability is investigating new configurations of Py thin film. As discussed in the dissertation, magnetic simulation has shown that laminating Py thin film with high quality dielectric layers can effectively increase the variation of permeability. Other configurations of Py thin film will be further explored, and by combining both structural optimization of microwave components and ferromagnetic materials, the tunability will be greatly improved, and the dc consumption will be effectively reduced.

6.2.2 Utilizing Ferrite for Inductive Tunability

The ferromagnetic material used in this dissertation is Py due to its good magnetic and mechanical properties. Other soft ferromagnetic alloys include Co-Nb-Zr, Co-Ta-Zr, Fe-Hf-N, Co-Fe, Co-Fe-Si-O, Ni-Fe-SiO_2, and so on [124]. Ferromagnetic materials feature high and tunable permeability, which is preferred for implementing tunable microwave components. However, those magnetic films have very low resistivity ($\rho < 10^{-2}\,\Omega \cdot cm$), and thus often induce large eddy currents, which, in turn, causes extra loss and deteriorates Q factor and self-resonance frequency. Alternatively, soft ferrites generally have high resistivity ($\rho > 10^{4}\,\Omega \cdot cm$), and they are more suitable to suppress the generation of eddy current and reduce the ohmic loss, hence improving the critical Q factor and self-resonance frequency. The commonly used ferrites include Ni-Zn-Cu spinel, Yttrium Iron Garnet (YIG) and Co_2Z magnetoplumbite, etc [125]. Ni-Zn-Cu (Ni-Zn-Cu-Fe-O) has the feature of high

resistivity, high Curie temperature, and low magnetic loss. YIG is a kind of eminent gyromagnetic material, and is often used in designing tunable microwave components for above-f_{FMR} operation. Co_2Z ($Ba_3Co_2Fe_{24}O_{41}$) series are planar hexagonal ferrites and feature the highest f_{FMR} among existing ferrites, and have been utilized in off-chip inductors working at multi-GHz frequencies. Even though the permeability of ferrites may be lower than ferromagnetic materials, they may enable higher design efficiency. For example, for the tunable solenoid inductor design, the high resistivity of ferrites allows direct utilization as magnetic core, opposite to ferromagnetic (Py) that requires dielectric material (SiO_2) as insulation layer in the dissertation.

6.2.3 Further Developing Tunable Microwave Applications with Dually Tunable Design Methodology

In this dissertation, several tunable microwave applications have been implemented, including slow wave transmission line, inductors, bandpass filter, and phase shifters, and promising performance has been achieved. The dually tunable design methodology can be further developed to achieve wide range of microwave components. A straightforward application is tunable matching network. The matching network can be constructed by either transmission lines or lumped elements such as inductors (L) and capacitors (C). In the dissertation, transmission line with dual tunability is achieved, and inductance density and capacitive density can be tuned either simultaneously or separately. Therefor, when it is used in matching network, impedance can be matched in multiple frequency bands. Likewise, if the tuning network is constructed by tunable lumped elements (L and C), multi-band impedance matching can also be realized. Another tunable implementation is voltage-controlled oscillator (VCO). The conventional design method is using varactors or switched capacitor network to change the resonant frequency of LC tank so that the oscillation frequency can be tuned. If the

ferromagnetic and ferroelectric enabled tunable inductors and capacitors can be used in designing LC tank, the architecture of VCO can be significantly simplified, and the oscillation frequency can be varied in wider range, since both inductor and capacitor can be electrically tuned simultaneously.

Bibliography

[1] T. ETSI. *136 101, TS: Etsi ts 136 101 v12. 5.0 (2014-11)*.

[2] S. Goswami, H. Kim, and J. L. Dawson. "A frequency-agile RF frontend architecture for multi-band TDD applications". In: *IEEE Journal of Solid-State Circuits* 49.10 (2014), pp. 2127–2140.

[3] K Muhammad and B Krenik. "Front-Ends for Commercial Digitally Controlled Radios". In: *IMS2007 Workshop*. 2007.

[4] K. Konanur. "CMOS RF transceiver chip tackles multiband 3.5 G radio system". In: *RF DESIGN* 29.4 (2006), p. 22.

[5] H. Arslan. *Cognitive radio, software defined radio, and adaptive wireless systems*. Vol. 10. Springer, 2007.

[6] T.-Y. Yun and K. Chang. "Piezoelectric-transducer-controlled tunable microwave circuits". In: *IEEE Transactions on Microwave Theory and Techniques* 50.5 (2002), pp. 1303–1310.

[7] F Huang and R. Mansour. "Tunable compact dielectric resonator filters". In: *Microwave Conference, 2009. EuMC 2009. European*. IEEE. 2009, pp. 559–562.

[8] E. J. Naglich, J. Lee, D. Peroulis, and W. J. Chappell. "Extended passband bandstop filter cascade with continuous 0.85–6.6-GHz coverage". In: *IEEE Transactions on Microwave Theory and Techniques* 60.1 (2012), pp. 21–30.

[9] S. H. Barnes and J. E. Mann. *Voltage sensitive semiconductor capacitor*. US Patent 2,989,671. 1961.

[10] X. Luo, S. Sun, and R. B. Staszewski. “Tunable bandpass filter with two adjustable transmission poles and compensable coupling”. In: *IEEE Transactions on Microwave Theory and Techniques* 62.9 (2014), pp. 2003–2013.

[11] L. Kurra, M. P. Abegaonkar, A. Basu, and S. K. Koul. “Switchable and tunable notch in ultra-wideband filter using electromagnetic bandgap structure”. In: *IEEE Microwave and Wireless Components Letters* 24.12 (2014), pp. 839–841.

[12] C.-S. Lin, S.-F. Chang, and W.-C. Hsiao. “A Full-360° Reflection-Type Phase Shifter With Constant Insertion Loss”. In: *IEEE Microwave and Wireless Components Letters* 18.2 (2008), pp. 106–108.

[13] M. A. El-Tanani. “High linearity 1.5-2.5 GHz RF-MEMS and varactor diodes based tunable filters for wireless applications”. PhD thesis. University of California at San Diego, 2009.

[14] M. Rais-Zadeh, P. A. Kohl, and F. Ayazi. “MEMS switched tunable inductors”. In: *Journal of Microelectromechanical Systems* 17.1 (2008), pp. 78–84.

[15] Y. Shim, Z. Wu, and M. Rais-Zadeh. “A multimetal surface micromachining process for tunable RF MEMS passives”. In: *Journal of Microelectromechanical Systems* 21.4 (2012), pp. 867–874.

[16] Y. Shim, Z. Wu, and M. Rais-Zadeh. “A high-performance continuously tunable MEMS bandpass filter at 1 GHz”. In: *IEEE Transactions on Microwave Theory and Techniques* 60.8 (2012), pp. 2439–2447.

[17] K. Y. Yuk, S. Fouladi, R. Ramer, and R. R. Mansour. “RF MEMS switchable interdigital bandpass filter”. In: *IEEE Microwave and Wireless Components Letters* 22.1 (2012), pp. 44–46.

[18] E. Rocas, C. Collado, J. Mateu, N. Orloff, J. M. O'Callaghan, and J. C. Booth. "A large-signal model of ferroelectric thin-film transmission lines". In: *IEEE Transactions on Microwave Theory and Techniques* 59.12 (2011), pp. 3059–3067.

[19] H. Jiang, M. Patterson, D. Brown, C. Zhang, K. Pan, G. Subramanyam, D. Kuhl, K. Leedy, and C. Cerny. "Miniaturized and reconfigurable CPW square-ring slot antenna loaded with ferroelectric BST thin film varactors". In: *IEEE Transactions on antennas and propagation* 60.7 (2012), pp. 3111–3119.

[20] C. Kong, H. Li, X. Chen, S. Jiang, J. Zhou, and C. Chen. "A monolithic AlGaN/GaN HEMT VCO using BST thin-film varactor". In: *IEEE Transactions on Microwave Theory and Techniques* 60.11 (2012), pp. 3413–3419.

[21] C. Lugo, G. Wang, J. Papapolymerou, Z. Zhao, X. Wang, and A. T. Hunt. "Frequency and bandwidth agile millimeter-wave filter using ferroelectric capacitors and MEMS cantilevers". In: *IEEE transactions on Microwave Theory and Techniques* 55.2 (2007), pp. 376–382.

[22] H. Jiang, B. Lacroix, K. Choi, Y. Wang, A. T. Hunt, and J. Papapolymerou. "Ka-and U-band tunable bandpass filters using ferroelectric capacitors". In: *IEEE Transactions on Microwave Theory and Techniques* 59.12 (2011), pp. 3068–3075.

[23] Y. Wang, Y. Liu, H. Du, C. Liu, Q. Xue, X. Gao, S. Li, and Y. Lu. "A Frequency Reconfigurable Microstrip Antenna Based on $(Ba, Sr)TiO_3$ Substrate". In: *IEEE Transactions on Antennas and Propagation* 63.2 (2015), pp. 770–775.

[24] D. Judy, J. Qiu, J. Pulskamp, R. Polcawich, and R Kaul. “Reflection-type continuously-tunable phase shifter using PZT thin-film capacitors”. In: *Electronics letters* 45.3 (2009), pp. 171–173.

[25] B. F. Rahman, R. Divan, L. Stan, D. Rosenmann, L. E. Ocola, and G. Wang. “Tunable transmission line with nanopatterned thin films for smart RF applications”. In: *IEEE Transactions on Magnetics* 50.11 (2014), pp. 1–4.

[26] Y. Sebbag, I. Goykhmann, B. Desiatov, T. Nachmias, O. Yoshaei, M. Kabla, S. E. Meltzer, and U. Levy. “Silicon optical phase shifter based on strain induced by a piezoelectric PZT thin film”. In: *CLEO: Science and Innovations*. Optical Society of America. 2012, CTh1C–3.

[27] U. Shah, J. Liljeholm, T. Ebefors, and J. Oberhammer. “Permeability Enhancement by Multilayer Ferromagnetic Composites for Magnetic-Core On-Chip Inductors”. In: *IEEE Microwave and Wireless Components Letters* 24.10 (2014), pp. 677–679.

[28] H. Wu, S. Zhao, D. S. Gardner, and H. Yu. “Improved high frequency response and quality factor of on-chip ferromagnetic thin film inductors by laminating and patterning Co-Zr-Ta-B films”. In: *IEEE Transactions on Magnetics* 49.7 (2013), pp. 4176–4179.

[29] G.-M. Yang, J. Wu, J. Lou, M. Liu, and N. X. Sun. “Low-loss magnetically tunable bandpass filters with YIG films”. In: *IEEE Transactions on Magnetics* 49.9 (2013), pp. 5063–5068.

[30] G. Qiu, C. S. Tsai, B. S. Wang, and Y. Zhu. “A YIG/GGG/GaAs-based magnetically tunable wideband microwave band-pass filter using cascaded band-stop filters”. In: *IEEE Transactions on Magnetics* 44.11 (2008), pp. 3123–3126.

[31] B. A. Belyaev, K. V. Lemberg, A. M. Serzhantov, A. A. Leksikov, Y. F. Bal'va, and A. A. Leksikov. "Magnetically Tunable Resonant Phase Shifters for UHF Band". In: *IEEE Transactions on Magnetics* 51.6 (2015), pp. 1–5.

[32] L.-P. Carignan, A. Yelon, D. Menard, and C. Caloz. "Ferromagnetic nanowire metamaterials: Theory and applications". In: *IEEE Transactions on microwave theory and techniques* 59.10 (2011), pp. 2568–2586.

[33] X. Yang, J. Wu, Y. Gao, T. Nan, Z. Zhou, S. Beguhn, and N. X. Sun. "Compact and low loss phase shifter with low bias field using partially magnetized ferrite". In: *IEEE Transactions on magnetics* 49.7 (2013), pp. 3882–3885.

[34] M. Vroubel, Y. Zhuang, B. Rejaei, and J. N. Burghartz. "Integrated tunable magnetic RF inductor". In: *IEEE Electron Device Letters* 25.12 (2004), pp. 787–789.

[35] J. Mullenix, A. El-Ghazaly, and S. X. Wang. "Integrated transformers with sputtered laminated magnetic core". In: *IEEE Transactions on Magnetics* 49.7 (2013), pp. 4021–4027.

[36] J.-S. G. Hong and M. J. Lancaster. *Microstrip filters for RF/microwave applications*. Vol. 167. John Wiley & Sons, 2004.

[37] J. Ni. "Development of turnable and miniature microwave filters for modern wireless communication". PhD thesis. Heriot-Watt University, 2014.

[38] H. Zhang, A. Hoffmann, R. Divan, and P. Wang. "Direct current effects on high-frequency properties of patterned permalloy thin films". In: *IEEE Transactions on Magnetics* 45.12 (2009), pp. 5296–5300.

[39] B. D. Cullity and C. D. Graham. *Introduction to magnetic materials*. John Wiley & Sons, 2011.

[40] D. Wu. “First-principles study on hard/soft samarium-cobalt/cobalt-iron nanocomposite magnetic materials”. PhD thesis. The University of Texas at Arlington, 2008.

[41] C.-H. Lambert, S. Mangin, B. C. S. Varaprasad, Y. Takahashi, M. Hehn, M Cinchetti, G. Malinowski, K Hono, Y Fainman, M Aeschlimann, et al. “All-optical control of ferromagnetic thin films and nanostructures”. In: *Science* 345.6202 (2014), pp. 1337–1340.

[42] F. Qin and H.-X. Peng. “Ferromagnetic microwires enabled multifunctional composite materials”. In: *Progress in Materials Science* 58.2 (2013), pp. 183–259.

[43] F. Liu, D. Han, M. Sun, and Y. Guo. *Magnetic recording sensor with sputtered antiferromagnetic coupling trilayer between plated ferromagnetic shields*. US Patent 8,760,819. 2014.

[44] C.-Z. Chang, W. Zhao, D. Y. Kim, H. Zhang, B. A. Assaf, D. Heiman, S.-C. Zhang, C. Liu, M. H. Chan, and J. S. Moodera. “High-precision realization of robust quantum anomalous Hall state in a hard ferromagnetic topological insulator”. In: *Nature materials* 14.5 (2015), pp. 473–477.

[45] J. Coey. *Magnetism and Magnetic Materials*. Cambridge University Press, 2010.

[46] D. JUNJIA. “Novel Magnonic Crystals and Devices: Fabrication, Static and Dynamic Behaviors”. PhD thesis. 2013.

[47] N. A. Spaldin. *Magnetic materials: fundamentals and applications*. Cambridge University Press, 2010.

[48] R. C. O’handley. *Modern magnetic materials: principles and applications*. Wiley, 2000.

[49] J. Griffiths. “Anomalous high-frequency resistance of ferromagnetic metals”. In: *Nature* 158.4019 (1946), p. 670.

[50] C. Kittel. “On the theory of ferromagnetic resonance absorption”. In: *Physical Review* 73.2 (1948), p. 155.

[51] L. Panina, M Ipatov, V Zhukova, A Zhukov, and J Gonzalez. “Magnetic field effects in artificial dielectrics with arrays of magnetic wires at microwaves”. In: *Journal of Applied Physics* 109.5 (2011), p. 053901.

[52] M Ipatov, V Zhukova, A Zhukov, and J Gonzalez. “Magnetoimpedance sensitive to dc bias current in amorphous microwires”. In: *Applied Physics Letters* 97.25 (2010), p. 252507.

[53] S. Adhikari, Y.-J. Ban, and K. Wu. “Magnetically tunable ferrite loaded substrate integrated waveguide cavity resonator”. In: *IEEE Microwave and Wireless Components Letters* 21.3 (2011), pp. 139–141.

[54] D. Jiles. *Introduction to magnetism and magnetic materials*. CRC press, 2015.

[55] M. Donahue. *Don porter. OOMMF User’s Guide, Release 1.2 a*. 2002.

[56] B. F. Rahman, R. Divan, D. Rosenmann, T. Wang, Y. Peng, and G. Wang. “Application of sub-micrometer patterned permalloy thin film in tunable radio frequency inductors”. In: *Journal of Applied Physics* 117.17 (2015), p. 17C121.

[57] B. Farid Rahman, R. Divan, H. Zhang, D. Rosenmann, Y. Peng, X. Wang, and G. Wang. “Direct current tunable noise suppressor using sub-micrometer patterned permalloy films”. In: *Journal of Applied Physics* 115.17 (2014), 17E515.

[58] T. Dastagir, W. Xu, S. Sinha, H. Wu, Y. Cao, and H. Yu. “Tuning the permeability of permalloy films for on-chip inductor applications”. In: *Applied Physics Letters* 97.16 (2010), p. 162506.

[59] T. Wang, W. Jiang, Y. Peng, and G. Wang. “Integration of ferromagnetic and ferroelectric films for fully electrically tunable RF devices”. In: *Radio and Wireless Symposium (RWS), 2017 IEEE*. IEEE. 2017, pp. 5–8.

[60] Y. Peng, T. Wang, W. Jiang, B. F. Rahman, T. Xia, and G. Wang. “Electrically Tunable Bandpass Filter With Patterned Permalloy Thin-Film-Enabled Engineered Substrate”. In: *IEEE Transactions on Magnetics* 51.11 (2015), pp. 1–4.

[61] B. Farid Rahman, R. Divan, H. Zhang, D. Rosenmann, Y. Peng, X. Wang, and G. Wang. “High performance tunable slow wave elements enabled with nano-patterned permalloy thin film for compact radio frequency applications”. In: *Journal of Applied Physics* 115.17 (2014), 17A508.

[62] Y. Peng, B. F. Rahman, T. Wang, C. Nowrin, M. Ali, and G. Wang. “Engineered smart substrate with embedded patterned permalloy thin film for radio frequency applications”. In: *Journal of Applied Physics* 117.17 (2015), 17B709.

[63] T. Wang, B. F. Rahman, Y. Peng, T. Xia, and G. Wang. “Arbitrary frequency tunable radio frequency bandpass filter based on nano-patterned Permalloy coplanar waveguide”. In: *Journal of Applied Physics* 117.17 (2015), p. 172605.

[64] A. Chezan, C. Craus, N. Chechenin, T Vystavel, J. T. M. De Hosson, L Niesen, and D. Boerma. “Controlling the induced anisotropy in soft magnetic films for high-frequency applications”. In: *IEEE transactions on magnetics* 38.5 (2002), pp. 3144–3146.

[65] M Yamaguchi, K Suezawa, M Baba, K. Arai, Y Shimada, S Tanabe, and K Itoh. “Application of bi-directional thin-film micro wire array to RF integrated spiral inductors”. In: *IEEE transactions on magnetics* 36.5 (2000), pp. 3514–3517.

[66] M. Yamaguchi, M. Baba, and K.-I. Arai. “Sandwich-type ferromagnetic RF integrated inductor”. In: *IEEE transactions on microwave theory and techniques* 49.12 (2001), pp. 2331–2335.

[67] W. R. Eisenstadt and Y. Eo. “S-parameter-based IC interconnect transmission line characterization”. In: *IEEE transactions on components, hybrids, and manufacturing technology* 15.4 (1992), pp. 483–490.

[68] O Gérardin, H Le Gall, M. J. Donahue, and N Vukadinovic. “Micromagnetic calculation of the high frequency dynamics of nano-size rectangular ferromagnetic stripes”. In: *Journal of Applied Physics* 89.11 (2001), pp. 7012–7014.

[69] R. Liu, J. Wang, Q. Liu, H. Wang, and C. Jiang. “Micromagnetic simulation of the magnetic spectrum of ferromagnetic nanowire”. In: *Journal of Applied Physics* 103.1 (2008), p. 013910.

[70] T. J. Silva, C. Lee, T. Crawford, and C. Rogers. “Inductive measurement of ultrafast magnetization dynamics in thin-film Permalloy”. In: *Journal of Applied Physics* 85.11 (1999), pp. 7849–7862.

[71] J Feng and D Thompson. “Permeability of narrow permalloy stripes”. In: *IEEE Transactions on Magnetics* 13.5 (1977), pp. 1521–1523.

[72] J.-W. Lin, C. Chen, and Y.-T. Cheng. “A robust high-Q micromachined RF inductor for RFIC applications”. In: *IEEE Transactions on Electron Devices* 52.7 (2005), pp. 1489–1496.

[73] H.-Y. Tsui and J. Lau. “An on-chip vertical solenoid inductor design for multigigahertz CMOS RFIC”. In: *IEEE transactions on microwave theory and techniques* 53.6 (2005), pp. 1883–1890.

[74] P.-C. Huang, K.-Y. Lin, and H. Wang. "A 4–17 GHz Darlington Cascode Broadband Medium Power Amplifier in $0.18-\mu$m CMOS Technology". In: *IEEE Microwave and Wireless Components Letters* 20.1 (2010), pp. 43–45.

[75] M. Demirkan, S. P. Bruss, and R. R. Spencer. "11.8 GHz CMOS VCO with 62% tuning range using switched coupled inductors". In: *Radio Frequency Integrated Circuits (RFIC) Symposium, 2007 IEEE*. IEEE. 2007, pp. 401–404.

[76] D. S. Gardner, G. Schrom, P. Hazucha, F. Paillet, T. Karnik, and S. Borkar. "Integrated on-chip inductors with magnetic films". In: *IEEE transactions on magnetics* 43.6 (2007), pp. 2615–2617.

[77] D. S. Gardner, G. Schrom, F. Paillet, B. Jamieson, T. Karnik, and S. Borkar. "Review of on-chip inductor structures with magnetic films". In: *IEEE Transactions on Magnetics* 45.10 (2009), pp. 4760–4766.

[78] J. Michel, Y Lamy, A. Royet, and B Viala. "New RF magnetic stripe inductors with flanges based on exchange-coupled magnetic films". In: *IEEE transactions on magnetics* 42.10 (2006), pp. 3368–3370.

[79] J. N. Burghartz and B. Rejaei. "On the design of RF spiral inductors on silicon". In: *IEEE transactions on electron devices* 50.3 (2003), pp. 718–729.

[80] K.-C. Lin, H.-K. Chiou, P.-C. Wu, W.-H. Chen, C.-L. Ko, and Y.-Z. Juang. "2.4-GHz complementary metal oxide semiconductor power amplifier using high-quality factor wafer-level bondwire spiral inductor". In: *IEEE Transactions on Components, Packaging and Manufacturing Technology* 3.8 (2013), pp. 1286–1292.

[81] D.-M. Fang, Q. Yuan, X.-H. Li, H.-X. Zhang, Y. Zhou, and X.-L. Zhao. "High performance MEMS spiral inductors". In: *Nano/Micro Engineered and Molecular Systems (NEMS), 2010 5th IEEE International Conference on*. IEEE. 2010, pp. 1033–1035.

[82] X.-N. Wang, X.-L. Zhao, Y. Zhou, X.-H. Dai, and B.-C. Cai. "Fabrication and performance of a novel suspended RF spiral inductor". In: *IEEE Transactions on Electron Devices* 51.5 (2004), pp. 814–816.

[83] J. Salvia, J. A. Bain, and C. P. Yue. "Tunable on-chip inductors up to 5 GHz using patterned permalloy laminations". In: *Electron Devices Meeting, 2005. IEDM Technical Digest. IEEE International*. IEEE. 2005, pp. 943–946.

[84] H. Wang, L. Sun, J. Liu, H. Zou, Z. Yu, and J. Gao. "Transfer function analysis and broadband scalable model for on-chip spiral inductors". In: *IEEE Transactions on Microwave Theory and Techniques* 59.7 (2011), pp. 1696–1708.

[85] B. F. Rahman, Y. Pengpeng, T. Wang, T. Xia, and G. Wang. "On-wafer calibration technique for high frequency measurement with simultaneous voltage and current tuning". In: *Journal of Electronic Testing* 31.1 (2015), pp. 67–73.

[86] J. Russat and F. Durbin. "Computation of intrinsic permeability from measured permeability: soft ferromagnetic thin films". In: *IEEE Transactions on Magnetics* 30.6 (1994), pp. 4833–4835.

[87] N Ning, X. Li, J Fan, W. Ng, Y. Xu, X Qian, and H. Seet. "A tunable magnetic inductor". In: *IEEE transactions on magnetics* 42.5 (2006), pp. 1585–1590.

[88] L. Wang, Y. Wang, H. Zhang, Z. Zhong, L. Wang, D. Peng, and F. Bai. "Integrated On-Chip Solenoid Inductors With Nanogranular Magnetic Cores". In: *IEEE Transactions on Magnetics* 52.7 (2016), pp. 1–4.

[89] R. P. Davies, C. Cheng, N. Sturcken, W. E. Bailey, and K. L. Shepard. "Coupled Inductors With Crossed Anisotropy $CoZrTa/SiO_2$ Multilayer Cores". In: *IEEE Transactions on Magnetics* 49.7 (2013), pp. 4009–4012.

[90] T. Wang, Y. Peng, W. Jiang, Y. M. Huang, B. F. Rahman, R. Divan, D. Rosenmann, and G. Wang. "Integrating Nanopatterned Ferromagnetic and Ferroelectric Thin Films for Electrically Tunable RF Applications". In: *IEEE Transactions on Microwave Theory and Techniques* 65.2 (2017), pp. 504–512.

[91] W Kipferl, M Dumm, P Kotissek, F Steinbauer, and G Bayreuther. "Bloch's law for epitaxial ultrathin dot arrays with uniaxial magnetic anisotropy". In: *Journal of applied physics* 95.11 (2004), pp. 7417–7419.

[92] K. Entesari and G. M. Rebeiz. "A differential 4-bit 6.5-10-GHz RF MEMS tunable filter". In: *IEEE transactions on microwave theory and techniques* 53.3 (2005), pp. 1103–1110.

[93] G. Chaudhary, Y. Jeong, and J. Lim. "Dual-band bandpass filter with independently tunable center frequencies and bandwidths". In: *IEEE Transactions on Microwave Theory and Techniques* 61.1 (2013), pp. 107–116.

[94] B.-W. Kim and S.-W. Yun. "Varactor-tuned combline bandpass filter using step-impedance microstrip lines". In: *IEEE Transactions on Microwave Theory and Techniques* 52.4 (2004), pp. 1279–1283.

[95] J. Nath, D. Ghosh, J.-P. Maria, A. I. Kingon, W. Fathelbab, P. D. Franzon, and M. B. Steer. "An electronically tunable microstrip bandpass filter using thin-film Barium-Strontium-Titanate (BST) varactors". In: *IEEE transactions on microwave theory and techniques* 53.9 (2005), pp. 2707–2712.

[96] B Liu, F Wei, and X Shi. "Reconfigurable bandpass filter based on net-type stepped-impedance resonator". In: *Electronics letters* 46.22 (2010), pp. 1506–1507.

[97] S.-G. Mao and Y.-Z. Chueh. "Coplanar waveguide bandpass filters with compact size and wide spurious-free stopband using electromagnetic bandgap

resonators". In: *IEEE Microwave and Wireless Components Letters* 17.3 (2007), pp. 181–183.

[98] A. Sanada, M. Kimura, T. Yamamoto, and I. Awai. "Fabrication of MOD-derived YBCO films on (001) $LaAlO_3$ and their application to $\lambda/4$ CPW SIR BPFs". In: *IEEE transactions on microwave theory and techniques* 50.12 (2002), pp. 2856–2861.

[99] S.-G. Mao, M.-S. Wu, Y.-Z. Chueh, and C. H. Chen. "Modeling of symmetric composite right/left-handed coplanar waveguides with applications to compact bandpass filters". In: *IEEE Transactions on Microwave Theory and Techniques* 53.11 (2005), pp. 3460–3466.

[100] J. K. Everard and K. K. Cheng. "High performance direct coupled bandpass filters on coplanar waveguide". In: *IEEE Transactions on Microwave Theory and Techniques* 41.9 (1993), pp. 1568–1573.

[101] M. E. Lines and A. M. Glass. *Principles and applications of ferroelectrics and related materials*. Oxford university press, 1977.

[102] A. Tagantsev, V. Sherman, K. Astafiev, J Venkatesh, and N Setter. "Ferroelectric materials for microwave tunable applications". In: *Journal of electroceramics* 11.1-2 (2003), pp. 5–66.

[103] C. Kügeler. *Integration of Ferroelectric Thin Films into Silicon Based Microsystems*. Tech. rep. Fakultät für Elektrotechnik und Informationstechnik, 2006.

[104] Y. Liu. "MEMS and BST technologies for microwave applications". PhD thesis. University of California, Santa Barbara, 2002.

[105] T. Wang, Y. Peng, W. Jiang, R. Divan, D. Rosenmann, T. Xia, and G. Wang. "High-performance electrically tunable RF phase shifter with the

application of PZT and permalloy thin-film patterns". In: *IEEE Transactions on Magnetics* 51.11 (2015), pp. 1–4.

[106] S. S. Bedair, J. S. Pulskamp, C. D. Meyer, M. Mirabelli, R. G. Polcawich, and B. Morgan. "High-performance micromachined inductors tunable by lead zirconate titanate actuators". In: *IEEE Electron Device Letters* 33.10 (2012), pp. 1483–1485.

[107] Y. Yang, Y. Hu, and Y. Lu. "Sensitivity of PZT impedance sensors for damage detection of concrete structures". In: *Sensors* 8.1 (2008), pp. 327–346.

[108] T. Kanda, A. Makino, T. Ono, K. Suzumori, T. Morita, and M. K. Kurosawa. "A micro ultrasonic motor using a micro-machined cylindrical bulk PZT transducer". In: *Sensors and Actuators A: physical* 127.1 (2006), pp. 131–138.

[109] A. Tatarenko, V Gheevarughese, and G Srinivasan. "Magnetoelectric microwave bandpass filter". In: *Electronics Letters* 42.9 (2006), pp. 540–541.

[110] Y. K. Fetisov and G Srinivasan. "Electric field tuning characteristics of a ferrite-piezoelectric microwave resonator". In: *Applied physics letters* 88.14 (2006), p. 143503.

[111] D. M. Pozar. *Microwave engineering*. John Wiley & Sons, 2009.

[112] A. M. Abbosh. "Compact tunable reflection phase shifters using short section of coupled lines". In: *IEEE Transactions on Microwave Theory and Techniques* 60.8 (2012), pp. 2465–2472.

[113] C.-L. Chen, W. E. Courtney, L. J. Mahoney, M. J. Manfra, A. Chu, and H. Atwater. "A low-loss Ku-band monolithic analog phase shifter". In: *IEEE transactions on microwave theory and techniques* 35.3 (1987), pp. 315–320.

[114] F. Ellinger, R. Vogt, and W. Bachtold. "Ultracompact reflective-type phase shifter MMIC at C-band with 360° phase-control range for smart antenna combining". In: *IEEE Journal of Solid-State Circuits* 37.4 (2002), pp. 481–486.

[115] M Nikfalazar, A Mehmood, M Sohrabi, M Mikolajek, A Wiens, H Maune, C Kohler, J. R. Binder, and R Jakoby. "Steerable dielectric resonator phased-array antenna based on inkjet-printed tunable phase shifter with BST metal-insulator-metal varactors". In: *IEEE Antennas and Wireless Propagation Letters* 15 (2016), pp. 877–880.

[116] D. Kim, Y. Choi, M. G. Allen, J. S. Kenney, and D. Kiesling. "A wide-band reflection-type phase shifter at S-band using BST coated substrate". In: *IEEE transactions on microwave theory and techniques* 50.12 (2002), pp. 2903–2909.

[117] O. G. Vendik. "Insertion loss in reflection-type microwave phase shifter based on ferroelectric tunable capacitor". In: *IEEE transactions on microwave theory and techniques* 55.2 (2007), pp. 425–429.

[118] K. Zheng, J. Lu, and J. Chu. "A novel wet etching process of Pb (Zr, Ti) O_3 thin films for applications in microelectromechanical system". In: *Japanese journal of applied physics* 43.6S (2004), p. 3934.

[119] J. Leach, H Liu, V Avrutin, E Rowe, Ü Özgür, H Morkoç, Y.-Y. Song, and M Wu. "Electrically and magnetically tunable phase shifters based on a barium strontium titanate-yttrium iron garnet layered structure". In: *Journal of Applied Physics* 108.6 (2010), p. 064106.

[120] A. Geiler, S. Gillette, Y Chen, J Wang, Z Chen, S. Yoon, P He, J Gao, C Vittoria, and V. Harris. "Multiferroic heterostructure fringe field tuning of meander line microstrip ferrite phase shifter". In: *Applied Physics Letters* 96.5 (2010), p. 053508.

[121] I. Viswanathan, S. Yoon, T Sakai, A. Geiler, J. Wang, C. Chinnasamy, C Vittoria, and V. Harris. "High performance compact microstripline phase shifter at C-band using yttrium iron garnet". In: *IEEE Transactions on Magnetics* 45.10 (2009), pp. 4176–4178.

[122] F. Ellinger, H. Jackel, and W. Bachtold. “Varactor-loaded transmission-line phase shifter at C-band using lumped elements”. In: *IEEE Transactions on Microwave Theory and Techniques* 51.4 (2003), pp. 1135–1140.

[123] S. Kobayashi, K. Amanuma, and H. Hada. “Effect of interconnect layer on Pb (Zr, Ti) O 3 thin film capacitor degradation”. In: *IEEE Electron Device Letters* 19.11 (1998), pp. 417–419.

[124] C. Yang, F. Liu, X. Wang, J. Zhan, A. Wang, T.-L. Ren, L.-T. Liu, H. Long, Z. Wu, and X. Li. “Investigation of on-chip soft-ferrite-integrated inductors for RF ICsâĂŤPart I: Design and simulation”. In: *IEEE Transactions on Electron Devices* 56.12 (2009), pp. 3133–3140.

[125] C. Yang, F. Liu, X. Wang, J. Zhan, A. Wang, T.-L. Ren, L.-T. Liu, H. Long, Z. Wu, and X. Li. “Investigation of on-chip soft-ferrite-integrated inductors for RF ICsâĂŤPart II: Experiments”. In: *IEEE Transactions on Electron Devices* 56.12 (2009), pp. 3141–3148.